

## REPORT DOCUMENTATION PAGE

0365

Public reporting burden for this collection of information is estimated to average 1 hour per response, including the time for reviewing the data needed, and completing and reviewing the collection of information. Send comments regarding this burden estimate or any other aspect of this collection of information, including suggestions for reducing this burden, to Washington Headquarters Services, Directorate for Information Operations and Reports, 1215 Jefferson Davis Highway, Suite 1204, Arlington, VA 22202-4302, and to the Office of Management and Budget, Paperwork Reduction Project (0704-0188), Washington, DC 20503.

1. AGENCY USE ONLY (Leave blank)		2. REPORT DATE 21 April 1998		3. REPORT TYPE AND DATES COVERED Final Technical Report	
4. TITLE AND SUBTITLE Probability of Detection in SQUID Nondestructive Evaluation				5. FUNDING NUMBERS Grant # F49620-94-1-0369  61103D 3484/TS	
6. AUTHORS John P. Wikswa, Principal Investigator, Anthony P. Ewing, Research Associate					
7. PERFORMING ORGANIZATION NAME(S) AND ADDRESS(ES) Dept. of Physics and Astronomy 6301 Stevenson Center Vanderbilt University Nashville, TN 37235				8. PERFORMING ORGANIZATION REPORT NUMBER  EML-1998-1	
9. SPONSORING/MONITORING AGENCY NAME(S) AND ADDRESS(ES) AFOSR/NE 110 Duncan Ave Room B115 Bolling AFB, Washington DC 20332-8050				10. SPONSORING/MONITORING AGENCY REPORT NUMBER	
11. SUPPLEMENTARY NOTES					
12a. DISTRIBUTION/AVAILABILITY STATEMENT No restrictions				12b. DISTRIBUTION CODE	
13. ABSTRACT (Maximum 200 words) Superconducting QUantum Interference Device (SQUID) magnetometers are being used as tools for Nondestructive Evaluation (NDE) to detect and characterize defects in aging aircraft. To evaluate SQUID NDE reliability, a probability of detection (POD) analysis has been done. A boundary element method (BEM) measurement model using a Green's function developed specifically for crack problems has been constructed for use in the POD analysis. The model simulates the 2-D images of the magnetic field obtained by scanning a SQUID magnetometer over a plate containing a crack and carrying an injected dc-current. POD curves were generated through Monte Carlo simulation using distributions derived from sensitivity analyses and experimental noise measurements. For the conditions simulated, crack lengths of 1.4 mm (dc-measurement) and 0.0134 mm (ac-measurement) could be found with 90% probability of detection and 95% confidence. These small crack lengths suggest that additional experimental noise factors will have to be incorporated into the POD analysis before realistic SQUID NDE capability can be accurately quantified.  <div style="text-align: right; font-size: 1.2em;">19980430 069</div>					
14. SUBJECT TERMS Nondestructive evaluation, probability of detection, SQUID magnetometer, boundary element method.				15. NUMBER OF PAGES 17	
				16. PRICE CODE	
17. SECURITY CLASSIFICATION OF REPORT  UNCLASSIFIED	18. SECURITY CLASSIFICATION OF THIS PAGE  UNCLASSIFIED	19. SECURITY CLASSIFICATION OF ABSTRACT  UNCLASSIFIED	20. LIMITATION OF ABSTRACT  UL		

NSN 7540-01-280-5500

Computer Generated

STANDARD FORM 298 (Rev 2-89)  
Prescribed by ANSI Std Z39-18  
298-102

DTIC QUALITY INSPECTED 3

# **Augmentation Awards for Science & Engineering Research Training (AASERT)**

Final Technical Report

Period Covering 6/30/94 to 12/31/97

Grant No. F49620-94-1-0369

John P. Wikswo, Principal Investigator  
Vanderbilt University

## **Final Report**

### **PROJECT PUBLICATIONS:**

#### **Ph.D. Dissertation:**

Anthony Ewing, Ph.D., Mechanical Engineering, 1997 (Major advisors: T.A. Cruse and J.P. Wikswo, Jr.).

See the attached executive summary of the dissertation: "Superconducting Quantum Interference Device Nondestructive Evaluation and Probability of Detection using a Boundary Element Measurement Model".

#### **Manuscripts in Preparation:**

"Green's Function Formulation of Laplace's Equation for Electromagnetic Crack Detection," T.A. Cruse, A.P. Ewing, and J.P. Wikswo, Jr., to be submitted to J. App. Physics.

"Using a SQUID Measurement Model for Sensitivity Analysis to Determine Probability of Detection," A.P. Ewing, T.A. Cruse, and J.P. Wikswo, Jr..

"A Boundary Element Measurement Model for SQUID Nondestructive Evaluation: An Experimental Comparison," A.P. Ewing, T.A. Cruse, and J.P. Wikswo, Jr..

#### **Conference Proceedings:**

"Measurements of Surface-Breaking Flaws in Ferromagnetic Plates by Means of an Imaging SQUID Susceptometer," A.C. Bruno, A.P. Ewing, and J.P. Wikswo, Jr., IEEE Trans. on Applied Superconductivity, 5(2): 2482-2485 (1995).

"Recent Advances in SQUID Magnetometers for Aging Aircraft NDE," W.G. Jenks, B. Ball, J. Cadzow, T. Cruse, A.P. Ewing, G. Hahn, X. Li, Y.P. Ma, and J.P. Wikswo, Jr., 4th Air Force Aging Aircraft Conference, 9-11 July 1996.

"Boundary Integral Equation Measurement Model for the Electric Current Injection Method of Nondestructive Evaluation," A.P. Ewing, C. Hall Barbosa, T.A. Cruse, A.C. Bruno, and J.P. Wikswo, Jr., COMPUMAG - The 11th Conference on the Computation of Electromagnetic Fields, PA4-6: 89-90 (1997).

"Probability of Detection (POD) in SQUID NDE," A.P. Ewing, J.P. Wikswo, Jr., and T.A. Cruse, Proceedings of the 1st Joint DoD/FAA/NASA Aging Aircraft Conference, in press.

"Measurements of Surface-Breaking Flaws in Steel Pipes Using a SQUID Susceptometer in an Unshielded Environment," C. Hall Barbosa, A.C. Bruno, G.S. Kuhner, J.P. Wikswo, Jr., Y.P. Ma, A.P. Ewing, and C.S. Camerini, 24<sup>th</sup> Annual Review of Progress in Quantitative NDE, 1997, in press.

"Boundary Integral Equations for Modeling Arbitrary Flaw Geometries in ECI NDE," A.P. Ewing, C. Hall Barbosa, T.A. Cruse, A.C. Bruno, and J.P. Wikswo, Jr., 24<sup>th</sup> Annual Review of Progress in Quantitative NDE, 1997, in press.

"A SQUID NDE Measurement Model Using BEM," A.P. Ewing, T.A. Cruse, and J.P. Wikswo, Jr., 24<sup>th</sup> Annual Review of Progress in Quantitative NDE, 1997, in press.

#### PERSONNEL SUPPORTED:

##### Graduate students:

7/1/94 - 9/30/97: Anthony Ewing - Probability of detection in non-destructive testing of aging aircraft.

12/1/94 - 1/31/95: Kevin Parker - Magnetic imaging with SQUIDs.

##### Undergraduate students:

Five undergraduate students were supported on a part-time basis for work on SQUID magnetometry, magnetic imaging, and the development of data acquisition electronics.

6/30/95 - 6/30/96: Drew Ammons, Nathan Carter

6/30/96 - 6/30/97: Drew Ammons, Nathan Carter, Eric Chen, and Nick Peters

6/30/97 - 12/31/97: Nick Peters, Trevis Crane

## Executive Summary

### SQUID NDE AND POD USING A BEM MEASUREMENT MODEL

by Anthony P. Ewing

#### Overview

As the commercial and military aircraft fleets age, additional resources are required to ensure their airworthiness. As the aircraft become older, the more likely they are to develop structural damage that may lead to unscheduled repairs or, in the worst case, accidents. Fatigue and corrosion are the two main causes of structural damage in aging aircraft and this research examines the use of a Superconducting QUantum Interference Device (SQUID) magnetometer as a tool for Nondestructive Evaluation (NDE) to detect and characterize these aging aircraft problems. The primary advantage of using SQUIDs in NDE over other techniques is the ability to detect second layer cracks and corrosion commonly found in aircraft structures.

In general, verification of a NDE method means demonstrating, through experiment and/or calculations, the ability to distinguish signal from noise for the flaw types and sizes and instrument/flaw configurations expected in the actual inspection. A common approach to quantify and validate the capabilities of an inspection technique is to conduct a probability of detection (POD) analysis. There are basically two ways to conduct this type of analysis. The first is, experimentally, which requires a large number of samples with ranging flaw characteristics being examined by several inspectors. The second is, analytically, which requires a model simulating the inspection process for a range of samples and testing conditions.

A POD analysis has been done using the analytical approach, combined with experimental information, to evaluate SQUID NDE reliability consistent with damage tolerant design philosophies used in aerospace to make life predictions. A minimum detectable crack length at 90% probability of detection and 95% confidence was used as the reliability criteria.

#### Fatigue Cracks – a Problem Requiring NDE

Fatigue cracking in aircraft is primarily due to cyclic stress loading. For example, internal pressurization during flight creates stresses on the fuselage longitudinal skin splices. The two basic splice designs used are shown in Figure 1.

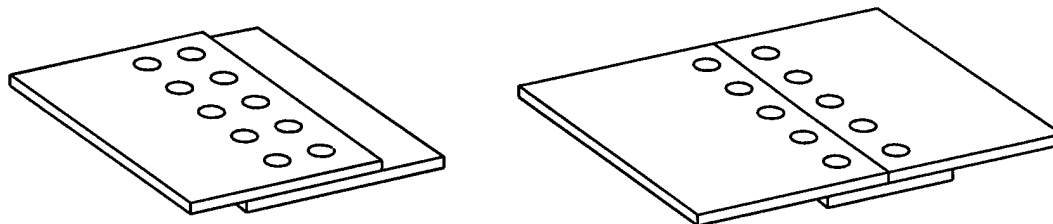


Figure 1 Fuselage skin splices: a) lap splice and b) butt splice

Fatigue cracks are most likely to develop along the direction of the fastener row since the primary stress direction is transverse to the row (see Figure 2). Usually, the cracks start at the fastener hole and propagate radially and, if there is multiple site damage (MSD), the structural strength is greatly reduced even for small crack lengths.

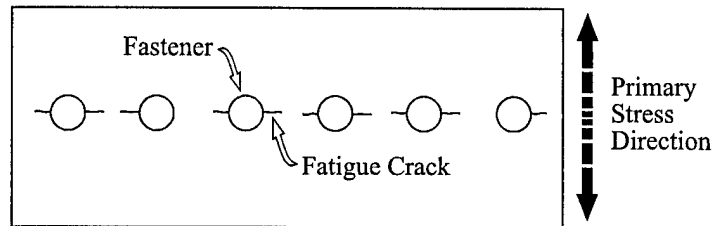


Figure 2 Fatigue crack development along direction of fastener row

Aircraft are designed to meet damage tolerant requirements and nondestructive evaluation/inspection (NDE/I) techniques are needed to efficiently and reliably detect and characterize damage, if it occurs, so that repairs can be made. Damage tolerant design basically involves fatigue crack growth predictions starting from some assumed crack length,  $a_0$ , due to possible manufacturing defects. For aircraft structures, damage tolerance specifications require a 90% detection probability and 95% confidence level for detecting a specified crack length,  $a_{th}$  (threshold crack length), at a particular location.

The dependence of  $a_{th}$  on the inspection process and the uncertainties associated with the detection of a crack lead to the statistical problem that can be addressed by POD analyses. Earlier NDE work established POD as a way in which NDE process performance could be quantified and incorporated into specifications, standards and design documents. By quantifying the procedure to measure the performance capability of a NDE system, objective comparison could be done for different NDE systems and NDE performance requirements could be defined for development of new techniques.

#### Probability of Detection (POD)

Probability of detection can be defined as the probability that a specific crack length can be detected with a particular inspection system under known conditions. POD combines characteristics of the measurement system, including noise, with statistical information pertinent to the cracks being examined. The schematic POD curve in Figure 3 shows the probability of detection as a function of crack length. The probability of detecting a small crack is low whereas, the probability of detecting larger cracks approaches unity.

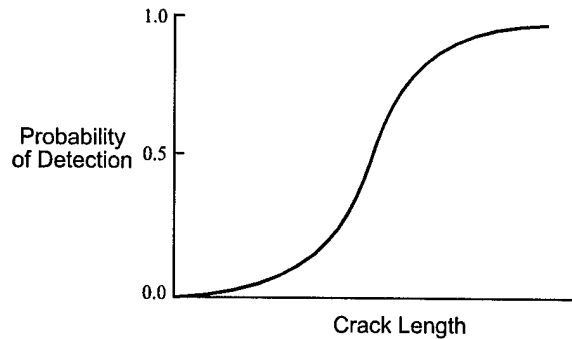


Figure 3 Probability of detection as a function of crack length

The POD function serves as a basis to evaluate the capability of an NDE system. For these analyses, POD is a function of crack length to be consistent with life prediction calculations that are based on crack length. The POD then is a measure of how well cracks of all sizes can be found. This capability cannot be determined exactly but, through the use of confidence bounds that account for the random errors of the NDE process, can be estimated. For example, the Air Force uses a 95% lower confidence bound that provides a risk factor that the true probability of detection is better than this bound 95% of the time.

#### Use of SQUID's in NDE

A superconducting quantum interference device (SQUID) magnetometer is the world's most sensitive detector of magnetic fields. The potential advantage that a SQUID has over other techniques is its ability to detect second layer flaws by using low frequency excitation.

A SQUID NDE technique is not only defined by the SQUID instrument characteristics but also by nature of the current distributions used to probe the flaws. When the current passing through the sample is affected by inhomogeneities, voids, cracks, and edges, the magnetic field is perturbed and can be sensed by the pickup coil of the SQUID. This work focuses on the dc-current injection technique. Injecting or inducing a uniform current distribution in the specimen causes the current to be parallel to the specimen surface under the pickup coil. For example, a large, uniform plate would have a magnetic field from this that encircles the specimen. This magnetic field would primarily be parallel to the specimen surface for scans centrally located and for small liftoff distances. The pickup coils measure only the perpendicular component (or gradient of this) of the magnetic field. A flaw in the specimen will perturb the parallel field and produce a perpendicular component which can then be detected (pickup coils measure only  $B_z$ ). Figure 4 illustrates the SQUID pickup coil being scanned over the sample containing a flaw and the typical magnetic map produced revealing a signature that commonly has a dipolar shape. The trough and ridge at the ends of the map are due to the edge effects of the plate.

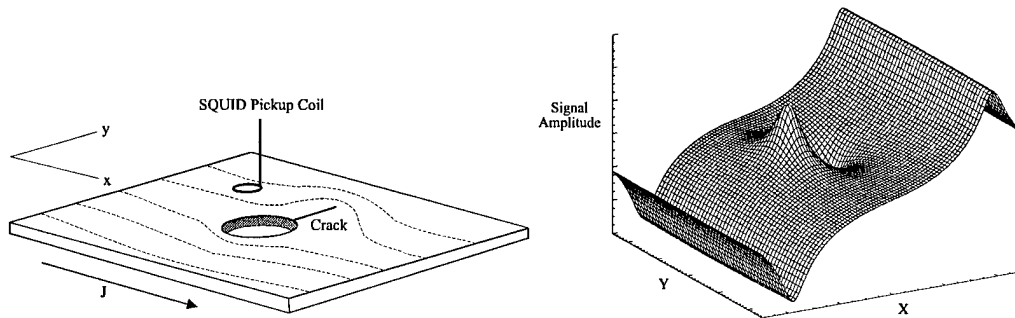


Figure 4 Dc-current injection: (a) scan over sample (b) resulting  $B_z$  magnetic map

Although this technique is not likely to be used in a field instrument, the current distributions produced are similar to the planar ac eddy currents produced by sheet inducers, which *are* proposed for a field instrument. Also, since existing boundary element methods can be used to model dc-current injection, the analytical approach to a POD analysis can be taken.

#### Measurement Model

A measurement model using boundary element methods has been constructed simulating a SQUID magnetometer being scanned over a dc-current injected, finite plate containing an ideal (*i.e.*, straight, infinitely thin, and perfectly insulated) crack. The model was used to examine the effect of system parameter variability on flaw detectability. The results of this sensitivity analysis was then combined with empirical noise distributions to determine probability of detection. A goal in this research was to develop a method where simulation represents the experimental approach, is cheaper and faster, and identifies sources of unreliability in SQUID NDE.

The objective of the SQUID measurement model, which solves the forward problem of calculating the magnetic field from a known current distribution, is to simulate what the instrument may see in a test environment on an unknown sample. A SQUID gradiometer measures the vertical component of magnetic field, which is the result of currents flowing in the sample. A flaw will perturb these currents and, if the perturbation is large enough (*e.g.*, signal/noise > 1), show up as an anomaly in the magnetic field map. The specific aging aircraft problem being addressed is the modeling of a fatigue crack emanating radially from a fastener hole (schematically shown in Fig. 5) as discussed previously regarding fuselage skin splices.

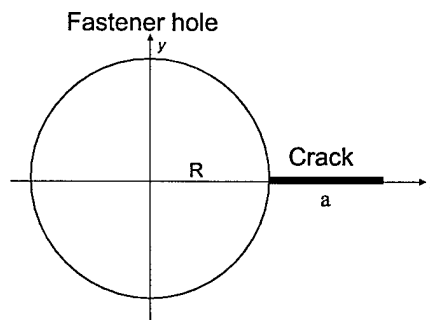


Figure 5 Schematic of a fastener hole with crack



For the interested reader, the details of the mathematical development of this can be found in Chapter II of the associated dissertation from which this summary is written.

#### POD Curves from Simulated Experimental Data

Figure 6 shows the centerline profiles of the magnetic maps resulting from simulated scans over a hole with crack for four different crack lengths while keeping the hole diameter constant. As can be seen, for increasing crack length, the signal

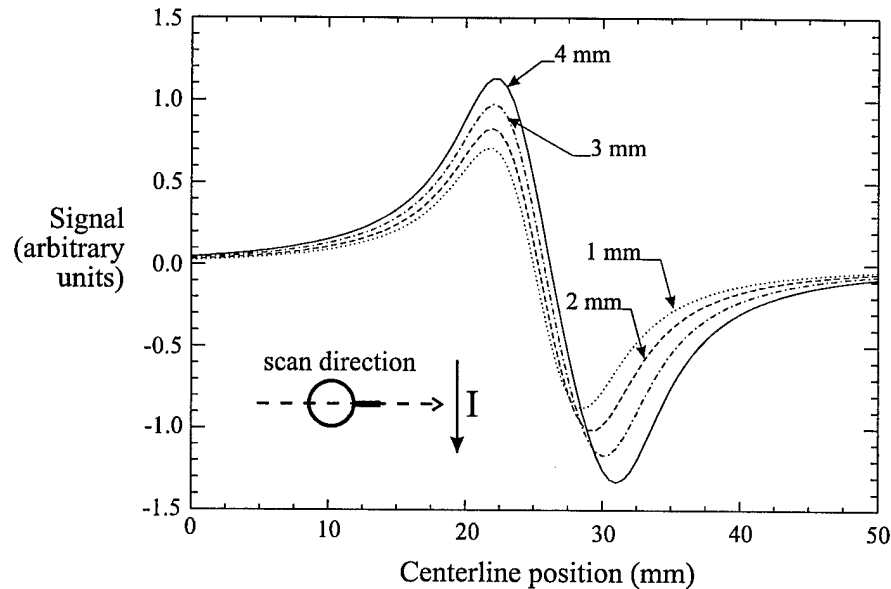


Figure 6 Scan centerline profiles for various crack lengths (with hole)

amplitude increases. Also, the asymmetry increases, pulling the crack side of the dipolar signal to the right while the hole side remains relatively fixed. The important characteristic for POD is the increasing peak-to-peak value as a function of crack length, which is the “signal” used in the POD analysis.

Sensitivity analyses were done on the system parameters of scan resolution, plate thickness, pick-up coil liftoff, and pick-up coil tilt angle to determine how they affect the overall signal distribution. Monte Carlo simulations used this signal distribution along with experimental noise distributions to generate realistic POD curves.

Noise distributions must be characterized in order to determine POD and POFA. Several noise distributions have been extracted from existing experimental data for different SQUID systems and measurement techniques. The measurement model simulates dc-current injection and experiments using direct dc-current injection have large noise distributions since they use the entire bandwidth of the SQUID (dc to ~10kHz) and therefore, include noise over these frequencies as well. Noise conditions associated with other experimental techniques are more representative of what SQUID’s will be operated in. Techniques based upon eddy current inducers use lock-in amplifiers at a particular frequency and greatly reduce the noise. The dc-measurement data shows approximately 400 pT peak-to-peak noise while the lock-in measurement data shows about 2 pT, a noise

reduction factor of 200! POD values determined using noise from lock-in measurements represent present SQUID capability.

Monte Carlo simulation, utilizing the results from the BEM measurement model, was used to sample from the uncertainty distributions of scan resolution, plate thickness, pick-up coil liftoff and pick-up coil tilt angle to generate an overall signal distribution. The resulting signal distribution was then compared with the noise distributions associated with ac and dc measurements to determine POD. A 95% lower confidence bound was then generated by iterative generation of multiple signal distributions at each crack length.

Figure 7 is the dc-measurement POD curve resulting from generating similar distributions at each crack length. The abruptness of the POD curve near the origin is due to a combination of the relative sharpness of the signal distribution with respect to the noise distribution and the one-sidedness of the noise distribution. The 95% lower confidence limit applies more to experimentally based POD curves that are usually generated from a relatively small number of data points. For simulated data, the lower confidence bound can be made to basically lie on the POD curve if enough runs are made and is not as useful as a concept as for the experimentally derived POD curve.

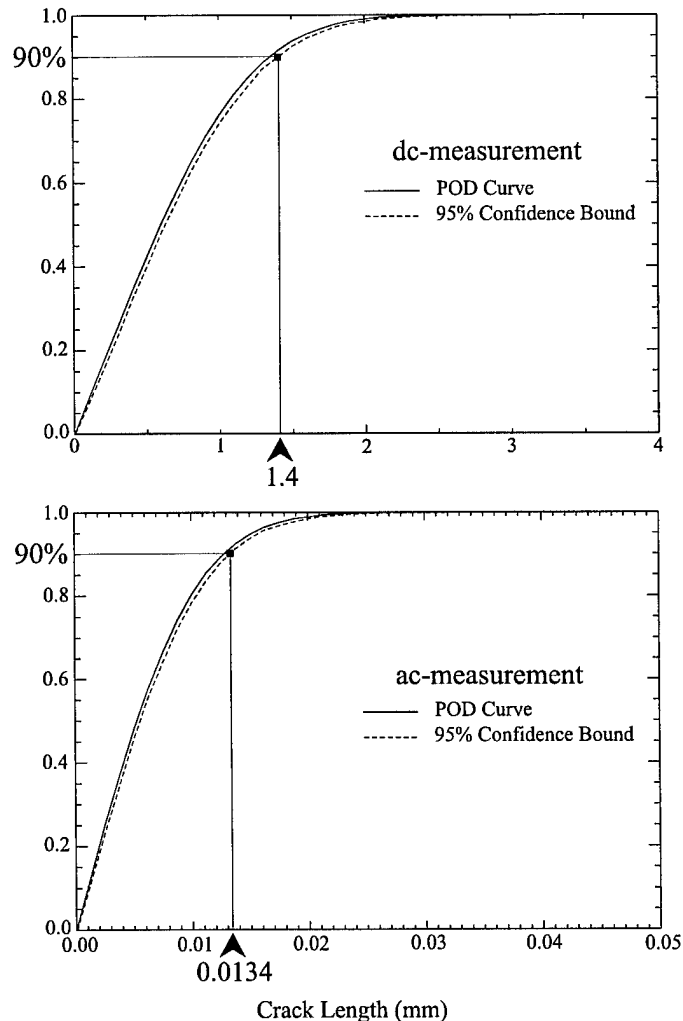


Figure 7 Ac/dc-measurement POD curves showing 90/95 crack lengths

The minimum detectable crack lengths corresponding to 90% probability of detection at 95% confidence are 1.4 mm for the dc-measurement and 0.0134 mm for the ac-measurement. The very small minimum detectable crack length determined for the ac-measurement is due to the large noise reduction through use of the lock-in amplifier in this type of measurement.

In the Monte Carlo simulations, the signal distribution was compared directly with the noise distribution to determine POD. For direct sampling from distributions, the signal-to-noise ratio set the threshold ( $\hat{a}_{th}$ ), which set the detection criteria. To examine the tradeoff between the probability of detection (POD) and the probability of false alarm (POFA) when setting  $\hat{a}_{th}$ , the signal and noise distribution data generated by the Monte Carlo simulations can be presented in a different format. The SNR requirements determine where  $\hat{a}_{th}$  is to be placed, thus affecting POD (larger SNR requirements correspond to larger minimum detectable crack lengths).

Figure 8 displays the dc-measurement POFA and POD curves for three crack lengths, including the minimum detectable crack length, as a function of threshold. By setting a threshold, a value for POFA and POD for all crack lengths is determined. As can be seen, for a crack length of 0.5 mm, the 90% probability of detection point corresponds to a 28% POFA (*i.e.*, there is a 28% chance that noise will be mistaken for a signal). There is only a single POFA curve since probability of false alarm is determined from the noise distribution, which for these simulations is constant. Figure 9 shows the ac-measurement POFA and POD as a function of threshold for the previously determined minimum detectable crack length of 0.0134 mm. In both the dc and ac measurement cases, the POFA corresponding to the minimum detectable crack length is approximately zero.

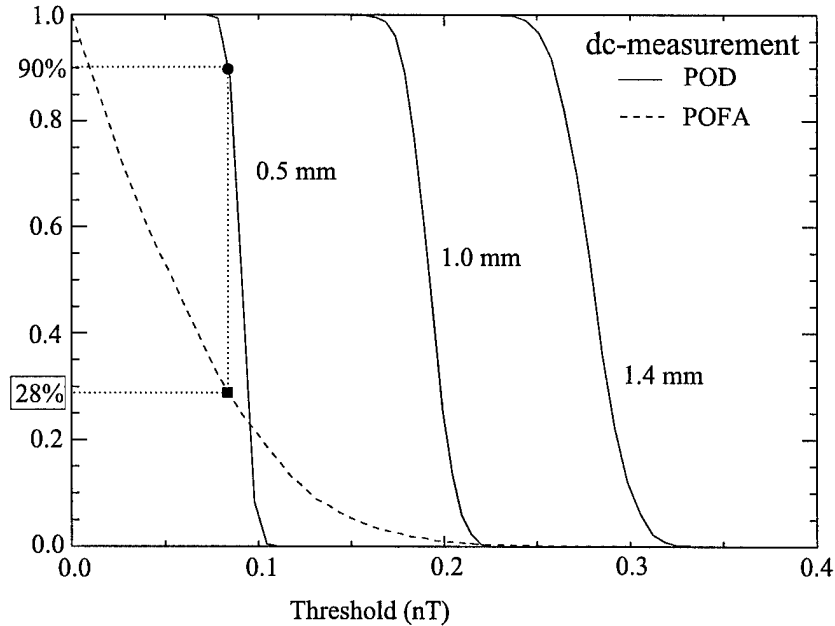


Figure 8 Dc-measurement POFA and POD as a function of threshold for three values of crack length

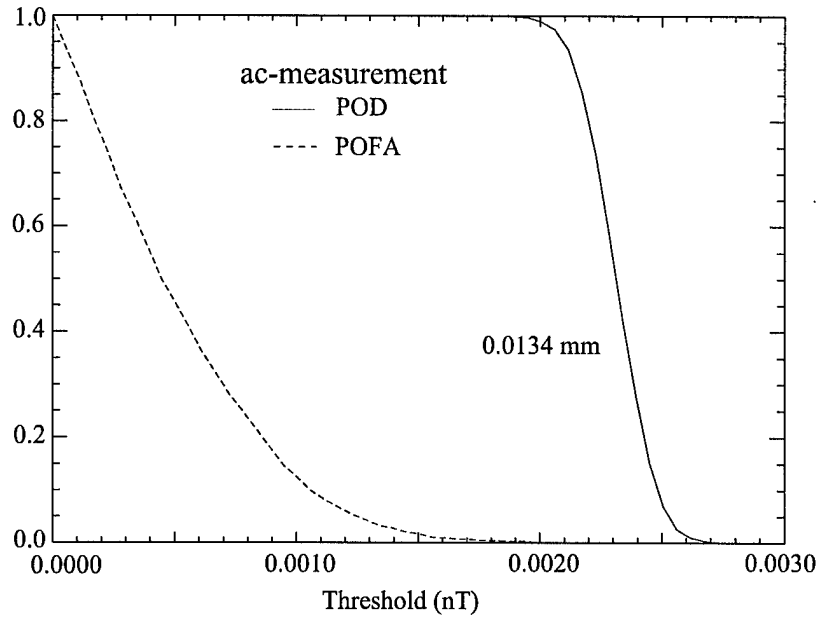


Figure 9 Ac-measurement POFA and POD as a function of threshold for the minimum detectable crack length

#### Factors That May Decrease POD Capability

The relatively small values of minimum detectable crack length determined from this analysis prompts discussion on whether this reflects the true capability of SQUIDs in the detection of real cracks near fasteners in aircraft lap joints. Experimental measurements using SQUIDs on fatigue cracks in lap joints have demonstrated the difficulty in finding cracks, adjacent to fasteners, on the order several millimeters in length. For the POD analysis done here, only four system parameters (scan resolution, plate thickness, pickup coil liftoff and tilt angle) and their associated uncertainties were considered. Since it is these parameter uncertainties that determine the overall signal distribution, and therefore POD, it is apparent that significant parameters have been left out of this analysis. More than likely, these stem from sample-related noise associated with real measurements, which have not been represented in either the measurement model itself or through the parameter uncertainty distributions. Sample-related noise results from the geometry of the sample or, more specifically, how that geometry affects the current flow used to probe the sample. Figure 10 shows how some of these current paths can go under and/or through the crack and the fastener, further complicating the detection and characterization of the crack. Some of these issues are discussed in the following sections.

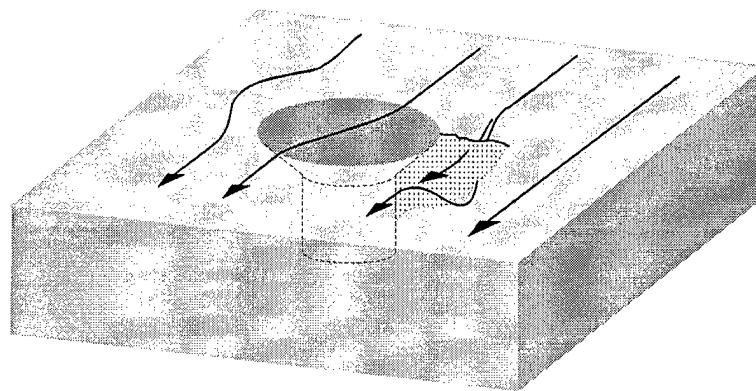


Figure 10 Additional current paths complicating crack detection

*Crack shape* - Probability of detection is traditionally stated as a function of crack length to be consistent with damage tolerant requirements, which are stated in terms of crack length. However, crack shape is an important issue to discuss briefly since cracks of the same “length” but different shape could result in different signals. Currently, the BEM measurement model simulates a straight-through crack (the same length through the entire thickness of the plate) but it is possible to use the model to simulate “3-D” cracks to examine the effect of crack “shape” on magnetic field. By creating slices of varying shapes and depths (see Fig. 11), a pseudo-3D crack can be modeled.

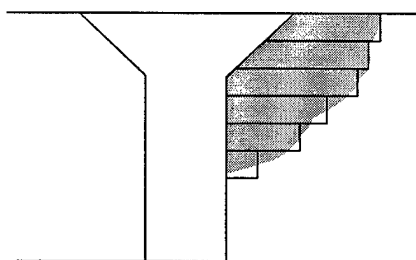


Figure 11 Pseudo 3-D modeling of a crack using slices

Since crack shape affects both the amplitude and the shape of the magnetic field, then this pseudo 3-D approach would be a better approximation to a real crack that has shape that varies with depth.

*Ideal cracks versus real cracks and slots* - The BEM measurement model assumes an ideal, perfectly insulating, and infinitely thin crack. This assumption will lead to differences between the model and measurements made on samples containing either wide cracks (slots) or real fatigue cracks. Most fabricated test samples used in our laboratory use slots, made by a saw or electrodischarge machining (EDM), to simulate cracks. A combination of a drilled hole with an EDM slot is an approximation to a crack emanating from an aircraft fastener hole. This is useful in preliminary analyses, especially for development of NDE techniques. Fabrication of test samples made this way is simple and controllable, making it easy to build a test set representing the range of conditions that are of interest. But, measurements with NDE instruments have shown that the instrument response from a slot is not necessarily the same as that from a fatigue

crack of the same size and geometry. Figure 12 schematically shows some of the possible variations, each possibly resulting in a different instrument response.

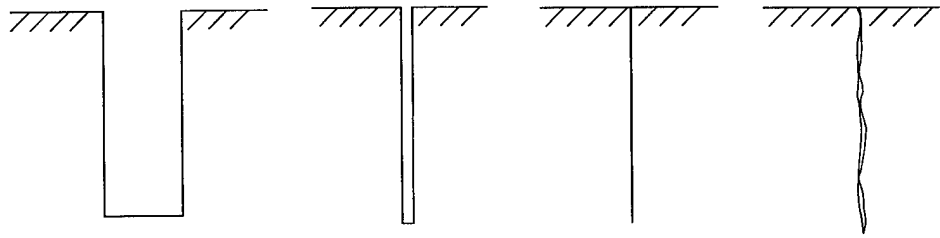


Figure 12 Slot profiles: (a) wide slot (b) narrow slot (c) ideal crack (d) real crack

The BEM measurement model simulates a closed crack that is electrically insulated along the entire length. We have shown that it provides a reasonable approximation to a thin slot for liftoffs appropriate for SQUIDs commonly used in the laboratory ( $> 3$  mm). However, for real fatigue cracks, it is possible that crack closure may cause electrical conductivity across parts of the crack. Probability of detection will be strongly dependent on the effects of crack closure since, if current is flowing through the crack instead of around it, the signal (which is proportional to the perturbation of the current) will be greatly reduced. It is not yet understood how much crack closure effects current flow since it is likely that the oxide layers that form on the crack surfaces will act as an electrical insulator and so, only those contact points where the oxide layer is not present will provide conductive paths.

*Additional current paths* - The POD analysis has been based on simulated measurements of a crack emanating from a fastener *hole* and has completely ignored the effects of the fastener itself. This is most likely one of the larger sources of discrepancy present between the model and real measurement. Since most fatigue cracks start under the fastener head, early detection is difficult and usually the crack has to propagate beyond the fastener head before detection occurs. Another critical issue is that of contact between the fastener and the hole sides, which can create numerous current flow paths across and through the fastener. These currents may be too difficult to model directly and their associated uncertainty might have to be represented through a sample-related noise distribution. This will probably have to be determined experimentally by examining samples with holes alone and with fasteners inserted to quantify the effect on the magnetic signal.

*Geometry factors* - Current can also be greatly affected by the geometry of the surrounding structure, particularly edges such as lap joint seams. Figure 13 shows that edges can produce a large signal amplitude that can make flaw detection difficult, especially if the flaw is located near an edge. Image processing techniques can partially remove the background slope due to these edges but it is still difficult to extract the signal from a flaw that is near an edge. Edges and other geometrical factors (*e.g.*, structural support members) affect the ability of the SQUID to detect a crack and these have not been taken into account in this POD analysis.

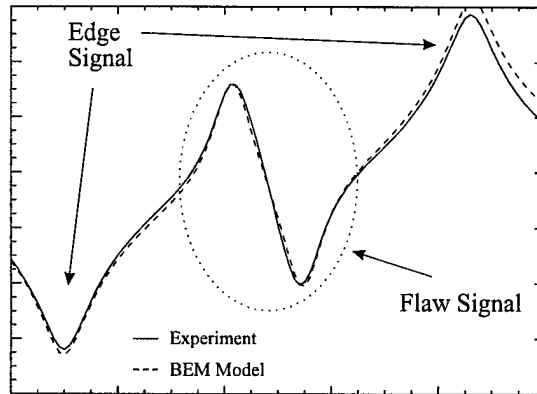


Figure 13 Magnetic map centerline profile pointing out edge and flaw signals

#### Factors That May Increase POD Capability

*Signal definition* - The peak-to-peak value of the magnetic dipolar map is the present definition of “signal” used in these analyses. Peak-to-peak amplitude is a very limited use of the information available in the mapping since it reduces the entire 2-D image to a single value. It is the opinion of the author that image features (*e.g.*, shape and asymmetry) of the 2-D magnetic field map are just as important as the peak-to-peak signal amplitude in the detection and characterization of cracks, especially near fastener holes. For example, if we look at the magnetic map centerline profiles for various ideal geometries that have the same “cross sectional length” perpendicular to the current injection direction, we can see that using only peak-to-peak information for current perpendicular to the crack can lead to detection problems. The left-hand side of Fig. 14 shows the profiles for the current transverse to the crack at three different liftoffs for a 9 mm diameter hole, a 5 mm hole with a 4 mm crack, and a 9 mm crack. The signal values for each of the traces are plotted on the same scale and represent a SQUID system using 3 mm pickup/balance coils with a 3 cm baseline. From this information, all the profiles look the same in that they are dipolar with a mostly symmetrical shape. Based on peak-to-peak amplitude in a single direction, we can not distinguish between a crack alone, hole alone, or a hole-with-crack combination unless a baseline signal amplitude can be established as was done earlier in this POD analysis using the signal associated with a 5 mm hole alone. However, this approach would not work here since the 5 mm hole is not a constant feature in all three geometries.

The rotating current schemes take advantage of the differing two-dimensional structure of these three geometries. By rotating the current direction, the signals associated with a crack will go through a maximum (when the current is perpendicular to the crack) and a minimum (when the current is parallel to the crack). A hole alone will not show this cyclic behavior (unless it is out-of-round). On the right-hand side of Fig. 14 are the corresponding profiles when the current is parallel to the crack showing the 9 mm crack having a flatline (zero signal) and the 5 mm hole with a 4 mm crack having a signal corresponding to a 5 mm hole alone and the 9 mm hole is unchanged. In this way, the three geometries could be distinguished by a measure of their peak-to-peak difference at the two current injection directions, with the crack alone being the largest, the hole-with-crack combination the next largest, and the hole alone having no difference. Real fatigue cracks will have some small signal for current injected parallel to the crack (versus zero signal for

the ideal cracks of Fig. 14) but will still show the same maximum/minimum behavior as a function of current injection direction (the signal difference will just be smaller than the ideal crack case).

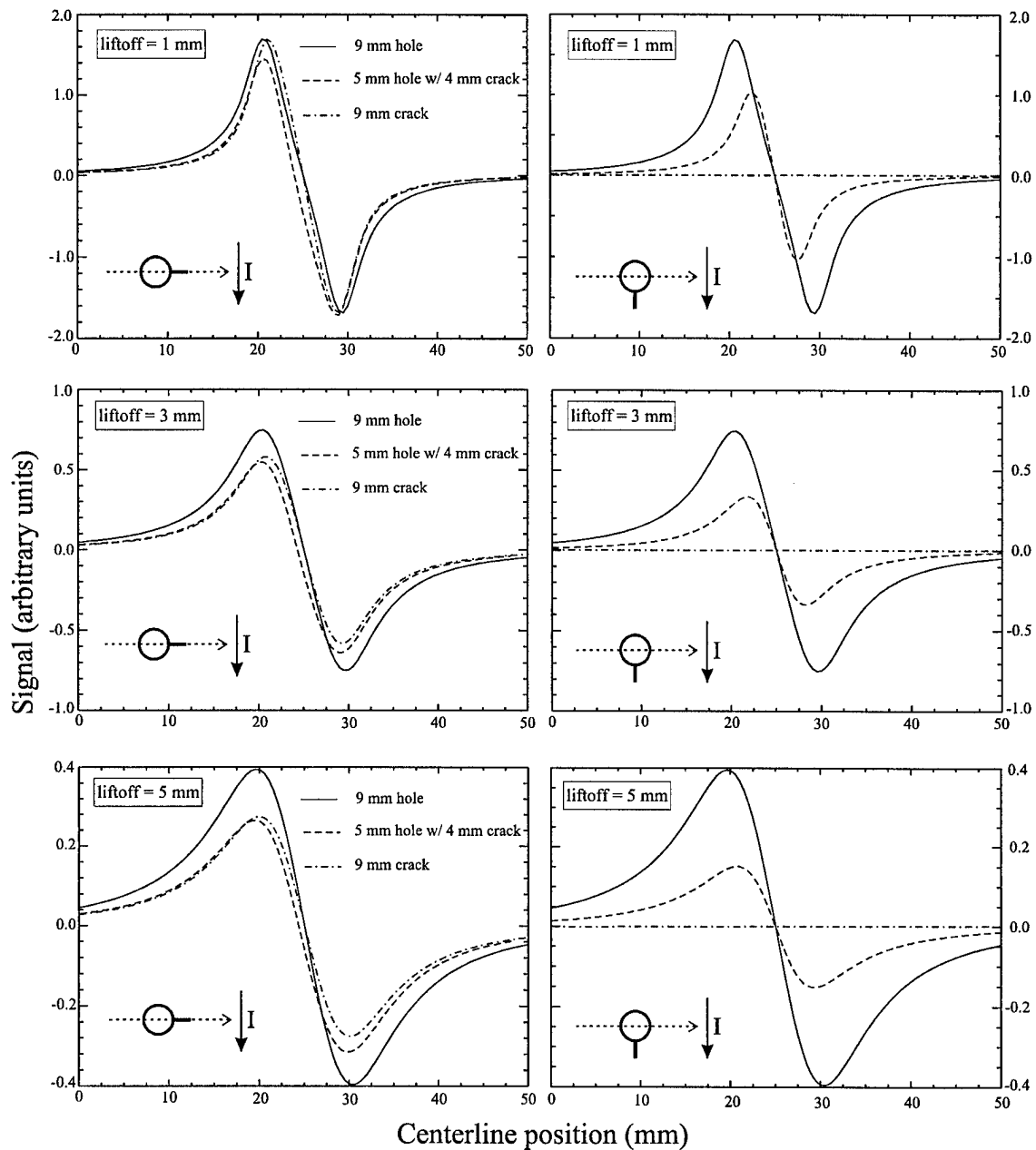


Figure 14 Profiles for three 9-mm "cross section" geometries at varying liftoffs  
(Note: all profile traces are on the same scale)

SQUID NDE systems will have to use asymmetry measures (which includes the rotating current direction technique) for crack detection, especially for cracks originating from fastener holes. If the asymmetry technique is used only to find the maximum and



minimum of the signal, then POD may still be determined primarily from peak-to-peak amplitudes. However, if additional measures of asymmetry (*e.g.*, eccentricity or other shape factors) are to be used, then POD analyses must incorporate these measures into the standard peak-to-peak analysis to reflect the true capability of the system. This is an important topic to be addressed for future development of SQUID POD methodologies.

### Conclusions

A measurement model using boundary element methods has been constructed simulating a SQUID magnetometer being scanned over a dc-current injected, finite plate containing an ideal (*i.e.*, straight, infinitely thin, and perfectly insulated) crack. The model was used to examine the effect of system parameter (scan resolution, plate thickness, pick-up coil liftoff, and pick-up coil tilt angle) variability on flaw detection. The results of this sensitivity analysis were then combined with empirical noise distributions to determine probability of detection. A goal in this research was to develop a method where simulation represents the experimental approach, is cheaper and faster, and identifies sources of unreliability in SQUID NDE.

This POD analysis resulted in minimum detectable crack lengths corresponding to 90% probability of detection at 95% confidence of 1.4 mm for the dc-measurement and 0.0134 mm for the ac-measurement. The very small minimum detectable crack length determined for the ac-measurement is due to the large noise reduction through use of the lock-in amplifier in this type of measurement. . However, there is a large discrepancy between experimental measurements on real fatigue cracks and the results of this analysis. If the model is to be used to calculate realistic probability of detection values for SQUID systems, more work has to be done to quantify additional sources of noise to be incorporated into the analysis. Some of the possible sources of this noise have been discussed but no work has been done as of yet to quantify their effects.

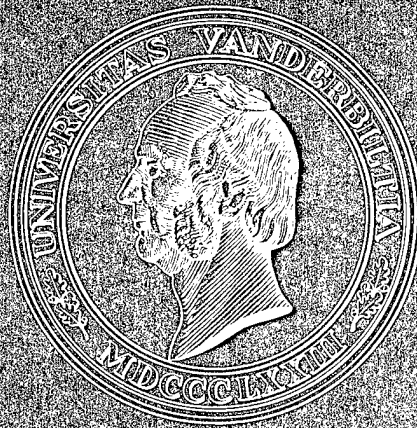
The BEM measurement model has already been used in other experimental work involving validation and calibration techniques. The model is just now beginning to be used for POD work, which was what it was originally designed for, and continued development will improve the model as a tool for SQUID NDE development and capability measurement.

**SQUID NDE AND POD USING A BEM  
MEASUREMENT MODEL**

by

Anthony Phillip Ewing

**Department of Physics and Astronomy**



**VANDERBILT UNIVERSITY  
NASHVILLE, TENNESSEE**

19980430 069

Report LSP-1997-1

Research supported by AFOSR Grant  
F49620-93-0268 and AASERT Grant  
F49620-94-1-0369

**DTIC QUALITY INSPECTED 3**

SQUID NDE AND POD USING  
A BEM MEASUREMENT MODEL

By

Anthony Phillip Ewing

Dissertation

Submitted to the Faculty of the  
Graduate School of Vanderbilt University  
in partial fulfillment of the requirements

for the degree of

DOCTOR OF PHILOSOPHY

in

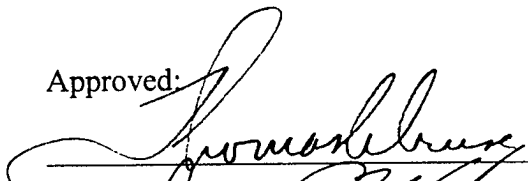
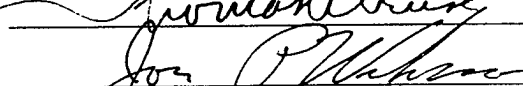
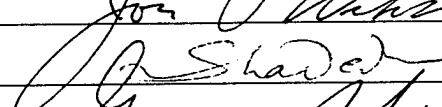
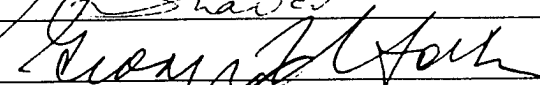
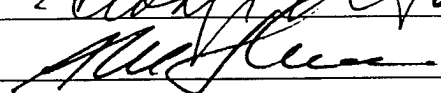
Mechanical Engineering

December, 1997

Nashville, Tennessee

Approved:

Date:

	12/1/97
	1 Dec 97
	12/1/97
	12/2/97
	12/2/97

SQUID NDE AND POD USING  
A BEM MEASUREMENT MODEL

ANTHONY PHILLIP EWING

Dissertation under the direction of Professors T.A. Cruse and J.P. Wikswo, Jr.

Superconducting QUantum Interference Device's (SQUID's) are being used as tools for Nondestructive Evaluation (NDE) to detect and characterize defects in aging aircraft. To evaluate SQUID NDE reliability, a probability of detection (POD) analysis has been done. A boundary element method (BEM) measurement model using a Green's function developed specifically for crack problems has been constructed for use in the POD analysis. The model simulates the 2-D images of the magnetic field obtained by scanning a SQUID magnetometer over a plate containing a crack and carrying an injected dc-current. POD curves were generated through Monte Carlo simulation using distributions derived from sensitivity analyses and experimental noise measurements. For the conditions simulated, crack lengths of 1.4 mm (dc-measurement) and 0.0134 mm (ac-measurement) could be found with 90% probability of detection and 95% confidence. These small crack lengths suggest that additional experimental noise factors will have to be incorporated into the POD analysis before realistic SQUID NDE capability can be accurately quantified.

Approved



Date

1 Dec. 97

Approved



Date

1 Dec 97

## ACKNOWLEDGEMENTS

The author was very grateful for the financial support by AFOSR Grant F49620-93-0268 and AASERT Grant F49620-94-1-0369.

The author thanks the members of the Mechanical Engineering and Physics departments who have assisted in this dissertation, especially my advisors Dr. T.A. Cruse and Dr. J.P. Wikswo, who have hopefully turned me into a decent engineer. Here also, I would like to thank the other members of my Ph.D. committee, Dr. S. Mahadevan, Dr. G. Hahn and Dr. A. Strauss. Additional thanks go to Dr. F. Shahrokhi, my initial thesis advisor at UTSI.

My folks, Margo and Gary, get a very special thank-you for always being there. And of course, friends and other family cannot be left out – thanks for the moral support!

## Table of Contents

	Page
ACKNOWLEDGEMENTS .....	ii
LIST OF FIGURES .....	v
LIST OF VARIABLES .....	viii
 Chapter	
I. INTRODUCTION	
Overview .....	1
Fatigue Cracks – a Problem Requiring NDE .....	2
Probability of Detection (POD) .....	5
Use of SQUID's in NDE .....	6
General Approach .....	8
 II. SQUID NDE MEASUREMENT MODEL	
Modeling the Measurement Process .....	10
Flaw Modeling .....	10
Superposition Measurement Model .....	11
Boundary Element Method Measurement Model .....	12
<i>Non-crack boundaries (<math>s = S</math>)</i> .....	18
<i>Crack boundaries (<math>s = I</math>)</i> .....	20
<i>Numerical integration</i> .....	22
Using the Measurement Model .....	26
 III. COMPARISON OF BEM MEASUREMENT MODEL TO EXPERIMENT	
Comparison Issues .....	28
Experimental Measurements .....	28
Calibrated System: SBIR .....	29
Measurements Using Other Systems .....	31
<i>MicroSQUID</i> .....	32
<i>Mobile HTS-SQUID</i> .....	33
 IV. POD CURVES FROM SIMULATED EXPERIMENTAL DATA	
Probability of Detection .....	35
Introduction .....	35
Determination from Experimental Data .....	36

Confidence Bounds .....	39
Importance of Setting Threshold Value .....	40
Progression of POD Approaches .....	41
Failure of Superposition .....	41
Standard Hole Subtraction Technique .....	43
Present POD Approach .....	47
Determination of POD Curves .....	54
System Parameter Uncertainty .....	55
<i>Scan resolution uncertainty</i> .....	57
<i>Thin plate approximation and plate thickness uncertainty</i> .....	59
<i>Pick-up coil liftoff uncertainty</i> .....	62
<i>Pick-up coil tilt angle uncertainty</i> .....	63
Noise Measurements .....	65
Monte Carlo Simulation .....	67
<i>A realistic test scenario</i> .....	67
<i>Steps of Monte Carlo distribution sampling</i> .....	68
<i>Monte Carlo generated POD curves</i> .....	70
<i>POD and POFA</i> .....	74

## V. SUMMARY AND DISCUSSION

Summary .....	76
Discussion .....	78
Factors That May Decrease POD Capability .....	78
<i>Crack shape</i> .....	79
<i>Ideal cracks versus real cracks and slots</i> .....	80
<i>Additional current paths</i> .....	82
<i>Geometry factors</i> .....	83
Factors That May Increase POD Capability .....	84
Other Comments and Suggestions .....	88

## Appendices

A. GREEN'S FUNCTION FORMULATION OF LAPLACE'S EQUATION FOR ELECTROMAGNETIC CRACK DETECTION .....	91
B. C-PROGRAM .....	115
C. FLUX/VOLTAGE CALIBRATION OF SQUID MAGNETOMETERS .....	125
D. LIST OF PUBLICATIONS/PRESENTATIONS .....	130
REFERENCES .....	132

## LIST OF FIGURES

### Figure

1.1.	Fuselage skin splices: a) lap splice and b) butt splice.....	2
1.2	Fatigue crack development along direction of fastener row.....	3
1.3	Crack growth and inspection .....	4
1.4	Probability of detection as a function of flaw size.....	5
1.5	The $\mu$ -SQUID system .....	6
1.6	Dc-current injection (a) scan over sample (b) resulting $B_z$ magnetic map .....	8
2.1	Schematic of fastener hole with crack .....	11
2.2	Hole/crack superposition model using ellipses.....	12
2.3	Surface integration of slice .....	14
2.4	Relationship between surface and line integration .....	17
2.5	Boundary integration direction .....	18
2.6	Geometrical relationships for integration .....	19
2.7	Distance $\rho$ measured from crack tip .....	22
2.8	Discretization of crack into elements.....	23
2.9	Quadratic interpolation functions (a) regular element (b) crack-tip element .....	23
2.10	Input variables for BEM measurement model.....	26
3.1	SBIR – Experimental setup.....	30
3.2	SBIR – Magnetic field contour map and comparison profile .....	31
3.3	$\mu$ -SQUID – Experimental setup.....	32
3.4	$\mu$ -SQUID - Magnetic field contour map and comparison profile.....	33
3.5	Mobile HTS – Experimental setup .....	34



3.6	Mobile HTS – Magnetic field contour map and comparison profile .....	34
4.1	Cumulative distribution of rejected signals: real versus ideal .....	35
4.2	Integration of signal to determine POD .....	36
4.3	Effect of setting threshold value .....	41
4.4	Comparison of BEM and superposition models .....	42
4.5	Comparison for a 5-mm hole with a 3-mm crack .....	43
4.6	Subtraction of standard hole to extract signal due to crack .....	43
4.7	Crack signal dependence on subtraction hole position .....	44
4.8	Histogram showing distribution of residual crack signals .....	45
4.9	Calculated POD curves for hole subtraction scheme.....	46
4.10	Scan centerline profiles for various crack lengths (with hole) .....	47
4.11	Scan centerline profiles for various crack lengths (no hole).....	48
4.12	Signals as a function of crack length .....	49
4.13	Current flow concentration around fastener hole.....	50
4.14	Current density concentration near fastener hole ( $R = 2.5$ mm) .....	51
4.15	Determining POD from signal curves.....	53
4.16	Resulting POD curves for both cases.....	54
4.17	Dipole extrema scan resolution error .....	57
4.18	Error due to $1 \times 1$ mm scan resolution .....	58
4.19	Integration approximation over plate thickness .....	60
4.20	Sensitivity of $B_{pp}$ to liftoff for various crack lengths .....	63
4.21	Experimental noise time series .....	66
4.22	HTS-SQUID noise for dc (upper) and lock-in (lower) measurements .....	67

4.23	Monte Carlo generated signal and noise distributions for the dc case (1-mm crack length).....	71
4.24	Ac/dc-measurement POD curves showing 90/95 crack lengths .....	72
4.25	Dc-measurement POFA and POD as a function of threshold for three values of crack length.....	75
4.26	Ac-measurement POFA and POD as a function of threshold for the minimum detectable crack length.....	75
5.1	Additional current paths complicating crack detection .....	79
5.2	Pseudo 3-D modeling of a crack using slices .....	80
5.3	Slot profiles (a) wide slot (b) narrow slot (c) ideal crack (d) real crack.....	81
5.4	Detail from Fig. 3.4 pointing out edge and flaw signals.....	83
5.5	Profiles for three 9-mm “cross section” geometries at varying liftoffs .....	86
5.6	Contour plots showing extrema eccentricity.....	87
C.1	Gradiometer with pick-up coil and counter-wound balance coil.....	126
C.2	Calibration using a current carrying wire .....	127
C.3	Dipolar signal showing peak-to-peak separation and amplitude .....	127

## LIST OF VARIABLES

$a$  – actual crack length  
 $a_0$  – assumed initial crack length  
 $a_{th}$  – inspection threshold crack length  
 $t$  – inspection interval  
 $N_p$  – fracture mechanics propagation life  
 $S_f$  – safety factor  
 $a_p$  – permissible crack length  
 $a_f$  – failure crack length  
 $S/N$  – signal-to-noise ratio  
 $R$  – fastener hole radius  
 $\mu_0$  – permeability of free space  
 $\sigma$  – conductivity  
 $V$  – electric scalar potential  
 $r$  – distance between field and source points  
 $q$  – source point  
 $c$  – field point  
 $\vec{B}$  – magnetic field vector  
 $B_z$  – z-component of magnetic field  
 $B_{pp}$  – peak-to-peak value of the z-component of magnetic field  
 $\Omega$  – surface integration variable  
 $\tau$  – volume integration variable  
 $\Re$  – volume integration region  
 $s$  – linear integration variable  
 $h$  – slice or plate thickness  
 $S$  – non-crack boundary  
 $\Gamma$  – crack boundary  
 $V_t$  – tangential derivative of the scalar potential  
 $D$  – perpendicular distance to boundary segment  
 $z$  – lift-off  
 $\theta$  – angle between  $D$  and  $r$   
 $\delta$  – integration geometrical term  
 $b_1$  –  $V_t$  linear equation intercept  
 $b_2$  –  $V_t$  linear equation slope  
 $K^+$  – potential intensity factor (PIF)  
 $\beta$  – angle to crack tip evaluation point  
 $L$  – segment length  
 $\rho$  – distance from crack tip  
 $N(\xi)$  – quadratic interpolation (shape) function  
 $\xi$  – numerical integration variable in mapped space  
 $J$  – Jacobian  
 $\mu$  – distribution mean  
 $\sigma$  – distribution standard deviation  
 $\lambda$  – pick-up coil tilt angle

$\varepsilon$  – inspection system threshold crack length (Weibull distribution)  
 $\eta$  – central tendency of POD function (Weibull distribution)  
 $\hat{\alpha}$  – y-intercept of log-odds linear regression  
 $\hat{\beta}$  – slope of log-odds linear regression  
 $\gamma$  – confidence percentile  
 $F_{\gamma}(f_1, f_2)$  – F-distribution at  $\gamma$ -confidence  
 $f_1$  – degrees of freedom in F-distribution  
 $f_2$  – degrees of freedom in F-distribution  
 $N$  – sample size  
 $\psi$  – current flow potential streamlines  
 $\omega$  – streamline evaluation point angle  
 $e$  – dipole extrema eccentricity  
 $a_e$  – eccentricity major-axis  
 $b_e$  – eccentricity minor-axis  
 $PS_j$  – first order physical sensitivity factor  
 $\Psi$  –  $n$ -dimensional response surface  
 $d$  – pick-up coil to sample liftoff  
 $I$  – current  
 $l$  – wire half-length  
 $\Delta B_{pp}$  – error in  $B_{pp}$  from uncertainty  
 $s_{POD}$  – sample standard deviation of Monte Carlo generated POD values  
 $\bar{x}_{POD}$  – sample mean of Monte Carlo generated POD values

## CHAPTER I

### INTRODUCTION

#### Overview

As the commercial and military aircraft fleets age, additional resources are required to ensure their airworthiness. As the aircraft become older, the more likely they are to develop structural damage that may lead to unscheduled repairs or, in the worst case, accidents. Fatigue and corrosion are the two main causes of structural damage in aging aircraft and this research examines the use of a Superconducting QUantum Interference Device (SQUID) magnetometer as a tool for Nondestructive Evaluation (NDE) to detect and characterize these aging aircraft problems. The primary advantage of using SQUIDS in NDE over other techniques is the ability to detect second layer cracks and corrosion commonly found in aircraft structures.

In general, verification of a NDE method means demonstrating, through experiment and/or calculations, the ability to distinguish signal from noise for the flaw types and sizes and instrument/flaw configurations expected in the actual inspection. A common approach to quantify and validate the capabilities of an inspection technique is to conduct a probability of detection (POD) analysis. There are basically two ways to conduct this type of analysis. The first is, experimentally, which requires a large number of samples with ranging flaw characteristics being examined by several inspectors. The second is, analytically, which requires a model simulating the inspection process for a range of samples and testing conditions.

A POD analysis is being done using the analytical approach, combined with experimental information, to evaluate SQUID NDE reliability consistent with damage tolerant design philosophies used in aerospace to make life predictions. A minimum detectable crack length at 90% probability of detection and 95% confidence is being used as the reliability criteria.

### Fatigue Cracks – a Problem Requiring NDE

Fatigue cracking in aircraft is primarily due to cyclic stress loading. For example, internal pressurization during flight creates stresses on the fuselage longitudinal skin splices. The two basic splice designs used [1] are shown in Figure 1.1.

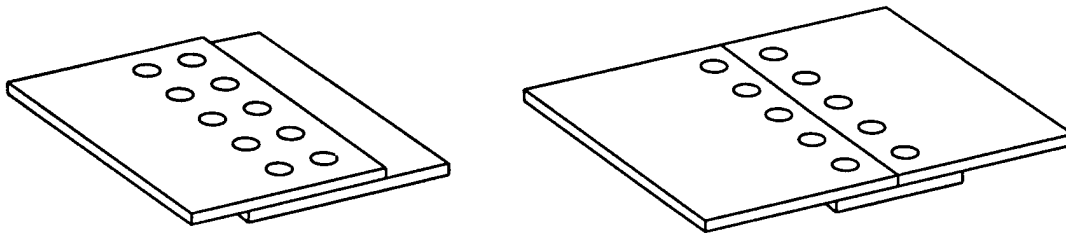


Figure 1.1 Fuselage skin splices: a) lap splice and b) butt splice

Fatigue cracks are most likely to develop along the direction of the fastener row since the primary stress direction is transverse to the row (see Figure 1.2). Usually, the cracks start at the fastener hole and propagate radially and, if there is multiple site damage (MSD), the structural strength is greatly reduced even for small crack lengths.

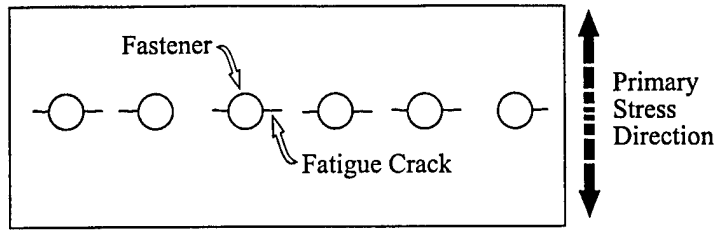


Figure 1.2 Fatigue crack development along direction of fastener row

Aircraft are designed to meet damage tolerant requirements [2-5] and nondestructive evaluation/inspection (NDE/I) techniques are needed to efficiently and reliably detect and characterize damage, if it occurs, so that repairs can be made. Damage tolerant design basically involves fatigue crack growth predictions starting from some assumed crack length,  $a_0$ , due to possible manufacturing defects. For aircraft structures, damage tolerance specifications require a 90% detection probability and 95% confidence level for detecting a specified crack length,  $a_{th}$ , at a particular location. The inspection interval,  $t$ , is determined by

$$t = \frac{N_p}{S_f}, \quad (1.1)$$

where  $N_p$  is the fracture mechanics propagation life or the life for a crack length  $a$  to propagate to the permissible crack length,  $a_p$ , under expected usage environments and  $S_f$  is the safety factor. The permissible crack length  $a_f$ , which is smaller than the failure crack length, is associated with minimum residual strength under the presence of cracks, defined by Federal Aviation Regulations Airworthiness Requirements (FAR-25)[6]. Commonly, a safety factor of two is used and so inspections are then required at half the

predicted time for the crack to reach the permissible crack length. After the first inspection, the crack length is reset to the largest crack length that can be missed by the inspection process being used,  $a_{th}$  (see Figure 1.3).

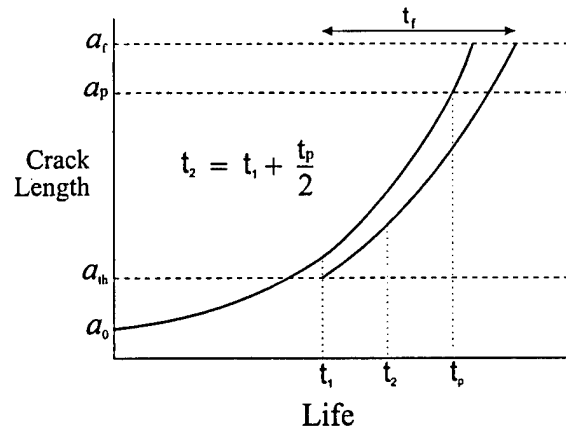


Figure 1.3 Crack growth and inspection

This process is repeated throughout the aircraft's life with detected cracks being repaired. The dependence of  $a_{th}$  on the inspection process and the uncertainties associated with the detection of a crack lead to the statistical problem that can be addressed by POD analyses. Earlier NDE work [7,8] established POD as a way in which NDE process performance could be quantified and incorporated into specifications, standards and design documents [3-5]. By quantifying the procedure to measure the performance capability of a NDE system, objective comparison could be done for different NDE systems and NDE performance requirements could be defined for development of new techniques.



### Probability of Detection (POD)

Probability of detection can be defined as the probability that a specific crack length can be detected with a particular inspection system under known conditions. POD combines characteristics of the measurement system, including noise, with statistical information pertinent to the cracks being examined. The schematic POD curve in Figure 1.4 shows the probability of detection as a function of crack length. The probability of detecting a small crack is low whereas, the probability of detecting larger cracks approaches unity.

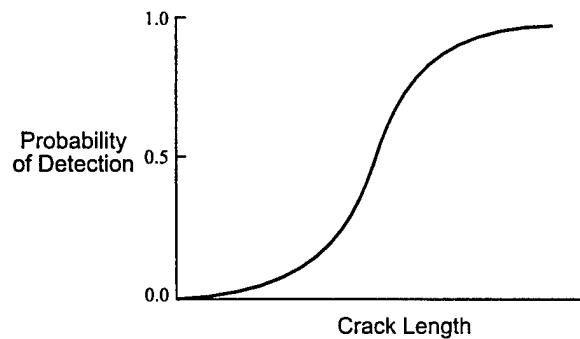


Figure 1.4 Probability of detection as a function of crack length

The POD function serves as a basis to evaluate the capability of an NDE system. For these analyses, POD is a function of crack length to be consistent with life prediction calculations that are based on crack length. The POD then is a measure of how well cracks of all sizes can be found. This capability cannot be determined exactly but, through the use of confidence bounds that account for the random errors of the NDE process, can be estimated. For example, the Air Force uses a 95% lower confidence bound that provides a risk factor that the true probability of detection is better than this bound 95% of the time.

## Use of SQUID's in NDE

A superconducting quantum interference device (SQUID) magnetometer is the world's most sensitive detector of magnetic fields. The potential advantage that a SQUID has over other techniques is its ability to detect second layer flaws by using low frequency excitation. Figure 1.5 shows one of the imaging SQUID gradiometer systems at Vanderbilt University (termed  $\mu$ -SQUID [9]) which contains four 3-mm diameter, 16 turn, closely-spaced pick-up coils for high resolution measurements. Minimum liftoff (pick-up coil to sample) distance is 2-3 mm. To reject noise, all pick-up coils are axial gradiometers, each having a counter-wound 12-mm, 1 turn, balance coil with a baseline of 3 cm. Two separate scanning stages are currently being used to move samples beneath SQUID instruments to produce the 2-D magnetic field maps. One, a non-magnetic high-speed (up to 10 cm/s) belt driven stage, is used inside the magnetic shield. The other, an open frame screw-drive stage, cannot be used inside the shield and must use a diving board assembly to hold the sample under the SQUID for scanning.

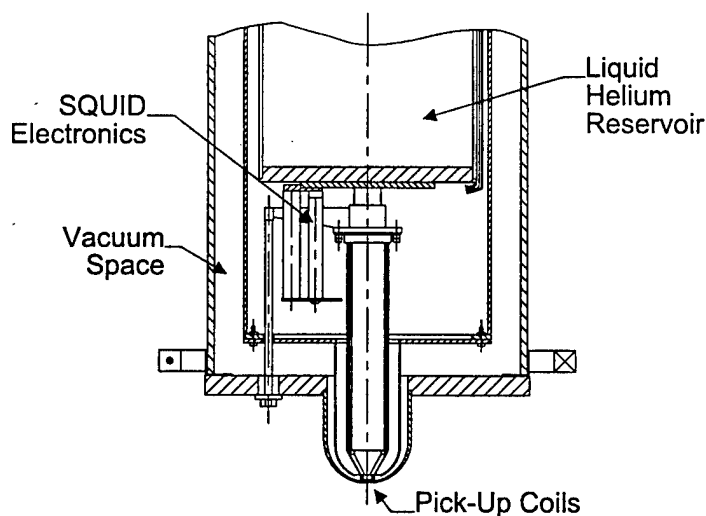


Figure 1.5 The  $\mu$ -SQUID system

A SQUID NDE technique is not only defined by the SQUID instrument characteristics but also by nature of the current distributions used to probe the flaws. When the current passing through the sample is affected by inhomogenities, voids, cracks, and edges, the magnetic field is perturbed and can be sensed by the pickup coil of the SQUID. Some of the commonly used techniques in SQUID NDE include the following:

- a) Ac/dc Current Injection: Injecting or inducing a uniform current distribution in the specimen causes the current to be parallel to the specimen surface under the pickup coil. For example, a large, uniform plate would have a magnetic field from this that encircles the specimen. This magnetic field would primarily be parallel to the specimen surface for scans centrally located and for small liftoff distances. The pickup coils measure only the perpendicular component (or gradient of this) of the magnetic field. A flaw in the specimen will perturb the parallel field and produce a perpendicular component which can then be detected (pickup coils measure only  $B_z$ ). Figure 1.6 illustrates the SQUID pickup coil being scanned over the sample containing a flaw and the typical magnetic map produced revealing a signature that commonly has a dipolar shape. The trough and ridge at the ends of the map are due to the edge effects of the plate.
- b) Inducing Plate: An eddy-current technique using a striped inducer sheet constructed from a 300  $\mu\text{m}$  copper sheet carrying a low frequency ac-current

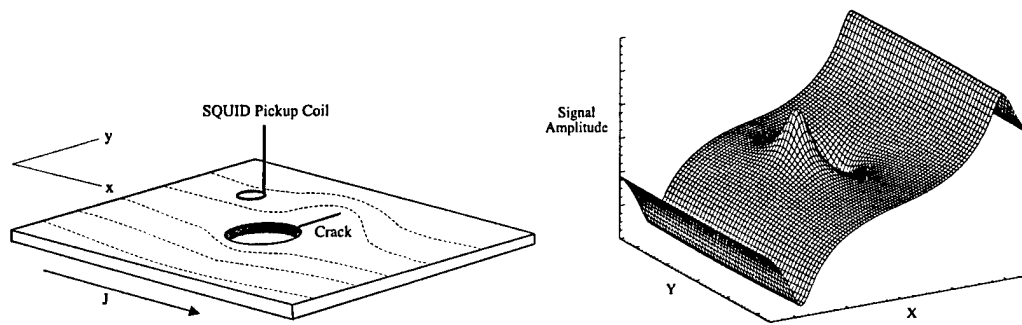


Figure 1.6 Dc-current injection: (a) scan over sample (b) resulting  $B_z$  magnetic map

has been used to image flaws in test specimens. This also leads into the present work related to the use of phase information of the eddy current image to determine depth of the flaw [10].

c) Ac Nulling: This is basically a modified eddy-current technique. An ac magnet located in the tail of the instrument is capable of producing a low-frequency ac-signal (200 Hz max). Optimizing software controls feedback circuitry to cancel the ac-signal that is directly coupled to the SQUID as different specimens are examined. This feedback allows a “zeroing” out of the signal before a scan and enables the instrument to be set on a higher sensitivity.

### General Approach

This work focuses on the dc-current injection technique. Although this technique is not likely to be used in a field instrument, the current distributions produced are similar to the planar ac eddy currents produced by sheet inducers, which *are* proposed for a field instrument. Also, since existing boundary element methods can be used to model dc-current injection, the analytical approach to a POD analysis can be taken.

A measurement model using boundary element methods will be constructed simulating a SQUID magnetometer being scanned over a dc-current injected, finite plate containing an ideal (*i.e.*, straight, infinitely thin, and perfectly insulated) crack. The model will be used to examine the effect of system parameter variability on flaw detectability. The results of this sensitivity analysis will then be combined with empirical noise distributions to determine probability of detection. A goal in this research is to develop a method where simulation represents the experimental approach, is cheaper and faster, and identifies sources of unreliability in SQUID NDE.

## CHAPTER II

### SQUID NDE MEASUREMENT MODEL

#### Modeling the Measurement Process

Due to the large number of parameters defining a method, experimental results alone are usually inadequate for examining the effect of parameter variation on POD. Therefore, predictive measurement models are needed in reliability analysis to extend the database required for a POD analysis. Using mathematical modeling, the response of the measurement system to the anomalies of interest (*e.g.*, cracks, corrosion, and voids) can be simulated if enough is known about the field-flaw interaction that generates the response function. Due to the complexity of the mathematics of these interactions, idealized models are normally used but these still provide sensitivity analysis information useful in constructing POD models.

The goal of a measurement model would be to predict, through repeated simulations with random perturbations in the system parameters that have known distributions, a distribution of flaw signals about some mean value. This distribution determines the POD performance for the particular system/technique being verified.

#### Flaw Modeling

The objective of the SQUID measurement model, which solves the forward problem of calculating the magnetic field from a known current distribution, is to simulate what the instrument may see in a test environment on an unknown sample. A

SQUID gradiometer measures the vertical component of magnetic field, which is the result of currents flowing in the sample. A flaw will perturb these currents and, if the perturbation is large enough (*e.g.*,  $\text{signal/noise} > 1$ ), show up as an anomaly in the magnetic field map. Ideally, “inverting” this magnetic field to give the underlying current map which generated the field would give much detail about the flaw producing the anomaly but, unfortunately, inverse solutions are non-unique (in 3-D) and even obtaining approximate reconstructions can be a very difficult job. The specific aging aircraft problem being addressed is the modeling of a fatigue crack emanating radially from a fastener hole (schematically shown in Fig. 2.1) as discussed in the previous chapter regarding fuselage skin splices. The measurement model involves only the forward problem and requires that the flaw geometry be known beforehand.

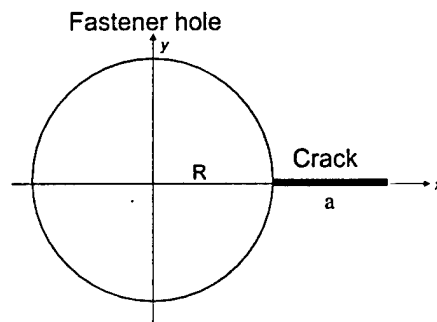


Figure 2.1 Schematic of a fastener hole with crack

### Superposition Measurement Model

To model a hole with a crack, an earlier measurement model was constructed using existing analytical solutions. Several analytical solutions for very simple geometries have been derived to represent the magnetic field produced by a flaw in a conductor. In the case of direct current injection, these include a spherical flaw in a

conducting half space, a flat-bottomed cylindrical flaw in a half space, and an elliptical flaw in a conducting plate (2-D). Scans of standard flaw specimens have experimentally validated these models [11,12].

The earlier measurement model constructed used the solution of the perturbed magnetic field due to an elliptical flaw in a conducting sheet containing injected current. In the elliptical model, the major/minor axes can be varied and also allows the limiting case of when the minor axis goes to zero (approximating a crack). By using superposition (Born approximation), one ellipse can act as the fastener hole and another ellipse, translated to one side, can act as a crack emanating from that hole as shown in Figure 2.2.

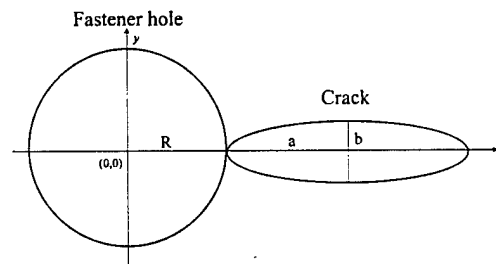


Figure 2.2 Hole/crack superposition model using ellipses

The superposition is only an approximation since it assumes non-interaction between the hole and the crack but provides a view of the critical issues confronting crack detection.

#### Boundary Element Method Measurement Model

The Boundary Element Method (BEM) provides the basis for the updated measurement model of a hole with a crack and is more accurate than the superposition model used for preliminary analysis. The superposition model was not accurate for the



geometry used since the hole and the crack interact when they are in close proximity. The BEM formulation solves for the potential problem of the hole and the crack together and thus, accounts for their interaction. The BEM model has replaced the superposition measurement model for use in generating signals used in the POD analysis.

By applying the law of Biot and Savart to the modeling of dc-current injection, an integral for the magnetic field results in a form that can be solved using BEM techniques. The law of Biot-Savart states that the magnetic field at a field point  $c$  can be determined from the volume integral over the region  $\mathfrak{R}$  of the curl (with respect to the point  $c$ ) of the gradient of the scalar potential  $V$ , at the source point  $q$ , divided by the distance  $r$  between the source and field points

$$\bar{B}(c) = -\frac{\mu_0 \sigma}{4\pi} \int_{\mathfrak{R}} \bar{\nabla}_c \times \left( \frac{\bar{\nabla}_q V(q)}{r(c, q)} \right) d\tau(q). \quad (2.1)$$

But

$$\bar{\nabla}_c \times \left( \frac{\bar{\nabla}_q V(q)}{r(c, q)} \right) = -\bar{\nabla}_q \times \left( \frac{\bar{\nabla}_q V(q)}{r(c, q)} \right) + \frac{\bar{\nabla}_q \times \bar{\nabla}_q V(q)}{r(c, q)} \quad (2.2)$$

and, for the case of a homogeneous, isotropic medium,  $V$  satisfies Laplace's equation (*i.e.*,  $V$  is a scalar potential field and  $\bar{\nabla} \times [\nabla(\text{scalar})] = 0$ ) and the second term on the right hand side of the above equation equals zero. Therefore,

$$\bar{\nabla}_c \times \left( \frac{\bar{\nabla}_q V(q)}{r(c, q)} \right) = -\bar{\nabla}_q \times \left( \frac{\bar{\nabla}_q V(q)}{r(c, q)} \right) \quad (2.3)$$

and now the integral is a function of  $q$  only (so we can hereafter drop the  $q$  notation),

$$\bar{B}(c) = \frac{\mu_0 \sigma}{4\pi} \int_{\mathfrak{R}} \bar{\nabla} \times \left( \frac{\bar{\nabla} V}{r} \right) d\tau. \quad (2.4)$$

One of the vector integral theorems [13] states that for a general vector  $F$ ,

$$\int_{\mathcal{R}} \bar{\nabla} \times \bar{F} d\tau = \oint_{\Omega} \hat{n} \times \bar{F} d\Omega, \quad (2.5)$$

where  $\Omega$  represents a 2-D surface. This is derived from the divergence theorem

$$\int_{\mathcal{R}} \nabla \cdot \bar{A} d\tau = \oint_{\Omega} \bar{A} \cdot \hat{n} d\Omega \quad (2.6)$$

by a substitution of  $\bar{A} = \bar{F} \times \bar{c}$  where  $\bar{c}$  is some arbitrary constant vector [14].

By applying this vector integral theorem to Eq. (2.4) and expanding out the cross product term, the integrand term can now be represented as

$$\hat{n} \times \frac{\bar{\nabla} V}{r} = \frac{1}{r} \left[ \left( n_y \frac{\partial V}{\partial z} - n_z \frac{\partial V}{\partial y} \right) \hat{i} - \left( n_x \frac{\partial V}{\partial z} - n_z \frac{\partial V}{\partial x} \right) \hat{j} + \left( n_x \frac{\partial V}{\partial y} - n_y \frac{\partial V}{\partial x} \right) \hat{k} \right]. \quad (2.7)$$

Now, assuming that the integration over the volume can be accomplished by taking thin slices perpendicular to the z-axis, then the resulting surface integral of this slice is over a top and bottom surface and a bounding side surface (see Fig. 2.3).

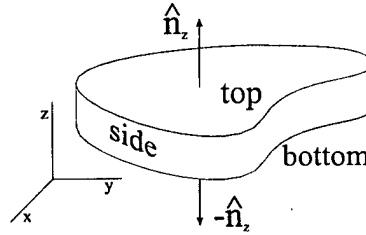


Figure 2.3 Surface integration of slice

Looking at each one of these surfaces separately:

- 1) Top surface: normal is in positive z-direction only,

$$\left( \hat{n} \times \frac{\bar{\nabla} V}{r} \right)_{top} = \frac{1}{r_t} \left( -n_z \frac{\partial V}{\partial y} \right) \hat{i} + \frac{1}{r_t} \left( n_z \frac{\partial V}{\partial x} \right) \hat{j}, \quad (2.8)$$

where  $\partial V / \partial y, \partial V / \partial x$  are evaluated at the top surface.

2) Bottom surface: normal is in negative z-direction only,

$$\left( \hat{n} \times \frac{\bar{\nabla} V}{r} \right)_{\text{bottom}} = \frac{1}{r_b} \left( n_z \frac{\partial V}{\partial y} \right) \hat{i} + \frac{1}{r_b} \left( -n_z \frac{\partial V}{\partial x} \right) \hat{j}, \quad (2.9)$$

where  $\partial V / \partial y, \partial V / \partial x$  are evaluated at the bottom surface. Note here that  $r_t$  and  $r_b$

differ by the slice thickness  $h$  in their z-component, i.e. if  $r_t$  is represented by

$$r_t = \sqrt{(x_c - x)^2 + (y_c - y)^2 + (z_c - z)^2}, \quad (2.10)$$

where the subscript  $c$  denotes the coordinates of the pickup coil, then  $r_b$  is

represented by

$$r_b = \sqrt{(x_c - x)^2 + (y_c - y)^2 + (z_c - [z - h])^2}. \quad (2.11)$$

3) Bounding side surface - normal is in x-y plane only,

$$\left( \hat{n} \times \frac{\bar{\nabla} V}{r} \right)_{\text{side}} = \frac{1}{r} \left( n_y \frac{\partial V}{\partial z} \right) \hat{i} - \frac{1}{r} \left( n_x \frac{\partial V}{\partial z} \right) \hat{j} + \frac{1}{r} \left( n_x \frac{\partial V}{\partial y} - n_y \frac{\partial V}{\partial x} \right) \hat{k}, \quad (2.12)$$

where all derivatives are evaluated at the bounding side surface.

The total surface integral is then the sum of these three cases. If it is further assumed that only 2-D current flow exists within this slice, then there will be no variation of the potential in the z-direction and the resulting derivatives of the potential at the top and bottom surfaces will be equal

$$\begin{aligned} \frac{\partial V}{\partial z} &= 0 \\ \frac{\partial V}{\partial x} \Big|_{\text{top}} &= \frac{\partial V}{\partial x} \Big|_{\text{bottom}} = \frac{\partial V}{\partial x} \\ \frac{\partial V}{\partial y} \Big|_{\text{top}} &= \frac{\partial V}{\partial y} \Big|_{\text{bottom}} = \frac{\partial V}{\partial y}. \end{aligned} \quad (2.13)$$

The cross product term is now

$$\left( \hat{n} \times \frac{\bar{\nabla} V}{r} \right)_{2D} = -\left( \frac{1}{r_t} - \frac{1}{r_b} \right) \left( n_z \frac{\partial V}{\partial y} \right) \hat{i} + \left( \frac{1}{r_t} - \frac{1}{r_b} \right) \left( n_z \frac{\partial V}{\partial x} \right) \hat{j} + \frac{1}{r_s} \left( n_x \frac{\partial V}{\partial y} - n_y \frac{\partial V}{\partial x} \right) \hat{k}. \quad (2.14)$$

This relationship shows that the magnetic field, for the assumption of 2-D current flow, has components in all three directions. For the conventional SQUID magnetometer system, the pickup coil is oriented in the x-y plane and thus measures only the z-component of magnetic field. Therefore, the only component of interest here is

$$\left( \hat{n} \times \frac{\bar{\nabla} V}{r} \right)_{2D} \Big|_{z\text{-direction}} = \frac{1}{r} \left( n_x \frac{\partial V}{\partial y} - n_y \frac{\partial V}{\partial x} \right) \hat{k}. \quad (2.15)$$

This result can be rewritten as  $\bar{\nabla} V/r$  dotted into the tangent vector:

$$\begin{aligned} \vec{t} &= \left( \frac{dx}{ds}, \frac{dy}{ds} \right) \\ \hat{n} &= \left( \frac{dy}{ds}, -\frac{dx}{ds} \right), \quad \vec{t} \cdot \hat{n} = 0 \\ \vec{t} &= (-n_y, n_x) \end{aligned} \quad \begin{array}{c} \text{dy} \uparrow \\ \text{ds} \nearrow \\ \text{dx} \leftarrow \end{array} \quad (2.16)$$

$$\hat{n} \times \frac{\bar{\nabla} V}{r} = \frac{1}{r} \left( n_x \frac{\partial V}{\partial y} - n_y \frac{\partial V}{\partial x} \right) = \frac{(\bar{\nabla} V \cdot \vec{t})}{r}.$$

So, with this substitution and letting  $q \rightarrow Q$  on the boundary, the final result for the magnetic field (in the z-direction) at the field point  $c$  as a function of the tangential derivatives of the scalar potential is

$$[\bar{B}_z(c)] = \left[ \frac{\mu_0 \sigma}{4\pi} \int_{\Omega} \frac{\bar{\nabla} V(Q) \cdot \vec{t}}{r(c, Q)} d\Omega \right] \hat{k}. \quad (2.17)$$

For the assumption of 2-D current flow within the thin slice (thickness  $h$ ), the integrand of Eq. (2.17) is approximately constant in the z-direction and the surface integral can be

represented as a line integration multiplied by the thickness  $h$ . In this way, a pseudo surface integration can be done over the surface  $\Omega$  where  $d\Omega = hds$  (see Figure 2.4). The final form of the boundary integral to be solved can now be represented as

$$B_z(c) = \frac{\mu_0 \sigma h}{4\pi} \int_s \frac{\vec{\nabla} V(Q) \cdot \hat{i}}{r(c, Q)} ds(Q). \quad (2.18)$$

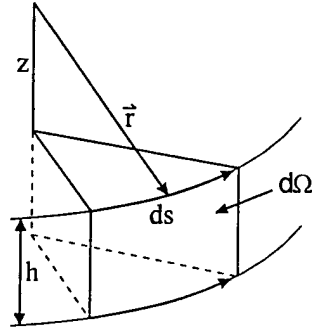


Figure 2.4 Relationship between surface and line integration

Some care must be exercised here to keep track of the sign as you move around the boundary during the integration of Eq. (2.18). Convention is to define the positive direction along  $s$  as to keep the material on your left as you move along the boundary. Integration direction around the boundary of the fastener hole with a crack is shown in Fig. 2.5. For the upper surface of the crack, the integration direction is in the positive  $x$  direction ( $ds = dx$ ) but, for the lower surface of the crack, the integration direction in the *negative*  $x$  direction ( $ds = -dx$ ).

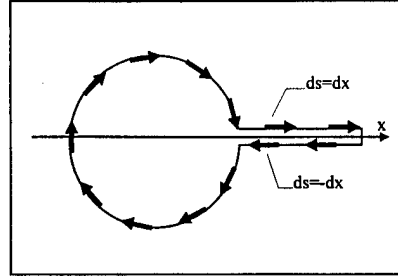


Figure 2.5 Boundary integration direction

Appendix A details the mathematical formulation [15] that will be applied to solving these boundary integral equations. In this formulation, the crack is modeled through the Green's function and not through the boundary of the crack eliminating the difficulties and inaccuracies associated with mesh construction around the crack tip region. The boundaries of interest here have been separated into those associated with the crack ( $s = \Gamma$ ) and non-crack ( $s = S$ ) boundaries since different techniques will be required to carry out the integration for each.

#### *Non-crack boundaries ( $s = S$ )*

The BEM program calculates  $dV/dt$  as a piecewise linear result since  $V(Q)$  is piecewise quadratic. Letting  $V_t = \bar{\nabla} V \cdot \hat{t}$  be the tangential component of the gradient of the scalar potential, we have for the line segment along  $s$

$$V_t(Q) = b_1 + b_2 s, \quad (2.19)$$

where  $b_1$  and  $b_2$  are different for each line segment. This is done for all boundary surfaces except for the crack surface ( $\Gamma$ ) (e.g., fastener hole, plate edges, etc.). Substituting this  $V_t$

into the integral for  $B_z(c)$ , Eq. (2.18), gives the contribution to the magnetic field at point  $c$  due to all non-crack boundaries

$$B_z(c)|_s = \frac{\mu_0 \sigma h}{4\pi} \int_s \frac{b_1 + b_2 s}{r(c, Q)} ds(Q). \quad (2.20)$$

To carry out the integration, the geometrical relations for  $r$  and  $s$  must be determined.

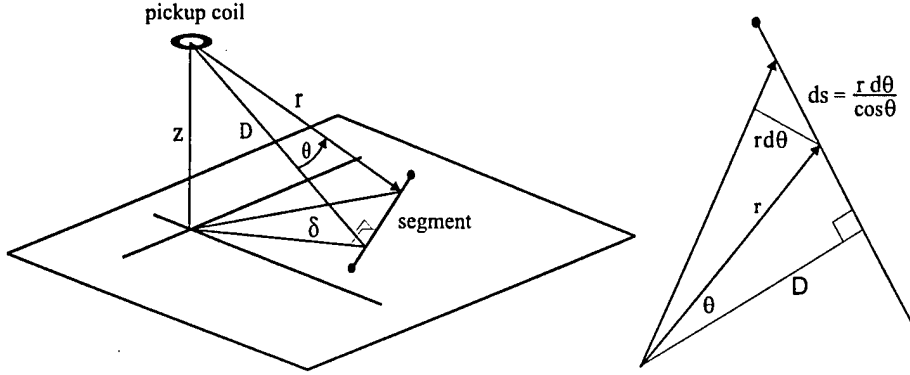


Figure 2.6 Geometrical relationships for integration

From the Fig. 2.6 we can see that

$$\begin{aligned} r &= \frac{D}{\cos \theta} \\ D &= \sqrt{z^2 + \delta^2} \\ ds &= \frac{r d\theta}{\cos \theta} = \frac{D d\theta}{\cos^2 \theta} \\ s &= D \tan \theta \Big|_{\theta_1}^{\theta_2} \Rightarrow D(\tan \theta - \tan \theta_1). \end{aligned} \quad (2.21)$$

Therefore, for non-crack boundaries, the integral is now

$$\begin{aligned}
B_z(c)|_s &= \frac{\mu_0 \sigma h}{4\pi} \int_s \frac{b_1 + b_2 D(\tan \theta - \tan \theta_1)}{\frac{D}{\cos \theta}} \frac{D d\theta}{\cos^2 \theta} \\
&= \frac{\mu_0 \sigma h}{4\pi} \left[ B_1 \int_s \frac{1}{\cos \theta} d\theta + b_2 D \int_s \frac{\sin \theta}{\cos^2 \theta} d\theta \right] \\
&= \frac{\mu_0 \sigma h}{4\pi} \left[ B_1 \ln \left\{ \tan \left( \frac{\pi}{4} + \frac{\theta}{2} \right) \right\} + \frac{b_2 D}{\cos \theta} \right]_s,
\end{aligned} \tag{2.22}$$

where  $B_1 = b_1 - b_2 D \tan \theta_1$  (constant term). Since the surface  $S$  is divided into  $n$  segments, the summation of this equation evaluated over each segment for which  $V_i$  is defined by a single linear equation (each with a different  $b_1$  and  $b_2$ ) will determine  $B_z$  at the pickup coil:

$$B_z(c) = \sum_n \frac{\mu_0 \sigma h}{4\pi} \left[ B_1 \ln \left\{ \tan \left( \frac{\pi}{4} + \frac{\theta}{2} \right) \right\} + \frac{b_2 D}{\cos \theta} \right]_{\theta_1}^{\theta_2}, \tag{2.23}$$

where  $\theta_1$  and  $\theta_2$  correspond to the angles between the perpendicular  $D$  and each endpoint of the segment as the summation moves in a positive sense around the boundary (material on left).

#### *Crack boundaries ( $s = \Gamma$ )*

For the crack (length  $a$ ), the singular behavior of  $V_i$  at the crack tip requires numerical integration to evaluate the magnetic field contribution of the crack. Values of  $V_i$  will be evaluated near the upper and lower crack surfaces using the BEM program and then the magnetic field will be calculated through a numerical integration of the previously stated Biot-Savart relation (Eq. 2.1). The series expansion of  $V_i$  is given by [16]



$$V_i = \frac{f_1(x)}{\sqrt{x^2 - a^2}} + f_2(x), \quad (2.24)$$

where  $f_1(x)$  and  $f_2(x)$  are analytic functions. The first term contains the discontinuity at the crack tip while the second term is needed to match far field boundary conditions. On the crack surface ( $\Gamma$ ) this can be rewritten as

$$\begin{aligned} V_i|_{\Gamma} &= \frac{if_1(x)}{\sqrt{a-x}\sqrt{a+x}} + f_2(x) \\ &= \frac{1}{\sqrt{\rho}} \frac{if_1(x)}{\sqrt{a+x}} + f_2(x) \\ &= \frac{1}{\sqrt{\rho}} iF_1(x) + f_2(x), \end{aligned} \quad (2.25)$$

where  $\rho$  is the distance measured from the crack tip (see Fig. 2.7). Equation (2.25) is well behaved except at the crack tip. On the crack boundary near the crack tip, the behavior of  $V_i$  can be represented in terms of the potential intensity factor (PIF),

$$K^+ \equiv \lim_{\rho \rightarrow 0} \sqrt{2\pi\rho} (V_i),$$

$$V_i|_{\text{crack tip region}} = \pm \frac{K^+}{\sqrt{2\pi\rho}} + \dots, \quad (2.26)$$

where the plus/minus sign is associated with the upper and lower crack surfaces respectively. Note that at  $\rho = 0$  (crack tip),  $V_i = \infty$ . The  $K^+$  factor is proportional to crack length (square root) and also to current and can be thought of as representing how much current is being diverted around the tip of the crack; the longer the crack length, the more current that is diverted. By combining Eqs. (2.25) and (2.26), we can express  $F_1$  at the crack tip in terms of the PIF

$$F_1(a) = \mp \frac{K^+}{\sqrt{2\pi}} - f_2(a). \quad (2.27)$$

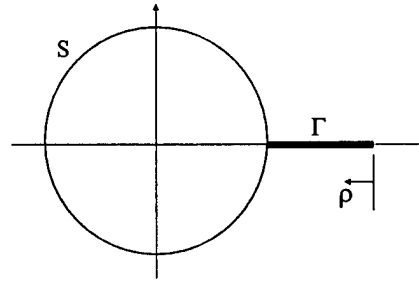


Figure 2.7 Distance  $\rho$  measured from crack tip

It will be assumed that  $f_2(a)$ , the far field boundary term, is small relative to the crack tip term and can be neglected. With the function value at the crack tip now defined, we can continue with the numerical integration development.

#### *Numerical integration*

Numerical integration over the crack is accomplished through discretization of the crack boundary into elements. By utilizing a coordinate transformation,  $V_i$  can be expressed in terms of nodal values and interpolation functions (shape functions) of an intrinsic coordinate  $\xi$ . Once mapped into  $\xi$ -space, Gaussian quadrature numerical integration can be used to evaluate the integral. This formulation uses quadratic interpolation functions  $N_m(\xi)$  which requires three nodes per boundary element. The crack is modeled with one crack-tip element containing the crack-tip node and one regular element (Fig. 2.8).

The regular element is a straightforward application of the interpolation functions but the crack-tip element will use a quarter-point formulation [17] to map the singular behavior at the crack tip. The general forms of the quadratic interpolation functions used to map the function to be integrated into the  $\xi$ -space are

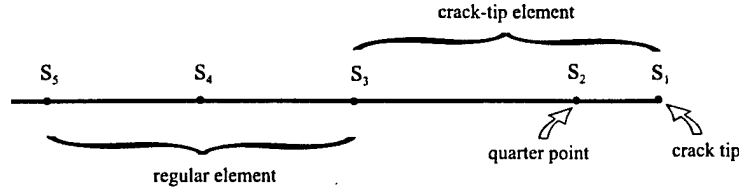


Figure 2.8 Discretization of crack into elements

$$\begin{aligned}
 N_1(\xi) &= \frac{1}{2}\xi(\xi-1) \\
 N_2(\xi) &= 1-\xi^2 \\
 N_3(\xi) &= \frac{1}{2}\xi(\xi+1),
 \end{aligned} \tag{2.28}$$

which are shown in Fig. 2.9. The coordinate transformation into  $\xi$ -space of the integral results in the following sum

$$\int_{\Gamma} F(s) ds \rightarrow \sum_{k=1}^3 \int_{-1}^{+1} N_k(\xi) F_k J(s, \xi) d\xi, \tag{2.29}$$

where  $F_k$  is the value of the function at the  $k^{th}$  node and  $J$  is the Jacobian of the mapping that accounts for the spatial scaling associated with the mapping

$$J(s, \xi) = \frac{ds}{d\xi} = \sum_{k=1}^3 \frac{dN_k}{d\xi} s_k. \tag{2.30}$$

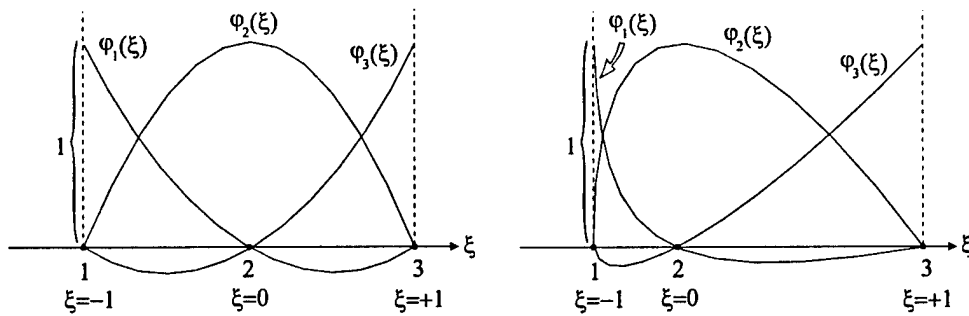


Figure 2.9 Quadratic interpolation functions (a) regular element (b) crack-tip element

For those boundary elements (length  $L$ ) that do not contain the crack tip, the resulting integral for  $B_z$  becomes

$$\begin{aligned}
B_z|_{\Gamma} &= -\frac{\mu_0 \sigma h}{4\pi} \int_0^L \left( \frac{V_t(s)}{r(s)} \right) ds \\
&= -\frac{\mu_0 \sigma h}{4\pi} \int_{-1}^{+1} \left[ N_1(\xi) \left( \frac{V_t(s)}{r(s)} \right)_{s_1} + N_2(\xi) \left( \frac{V_t(s)}{r(s)} \right)_{s_2} + N_3(\xi) \left( \frac{V_t(s)}{r(s)} \right)_{s_3} \right] J(s, \xi) d\xi \quad (2.31) \\
&= -\frac{\mu_0 \sigma h}{4\pi} \frac{L}{2} \int_{-1}^{+1} \left[ N_1(\xi) \left( \frac{V_t(0)}{r(0)} \right) + N_2(\xi) \left( \frac{V_t(L/2)}{r(L/2)} \right) + N_3(\xi) \left( \frac{V_t(L)}{r(L)} \right) \right] d\xi,
\end{aligned}$$

which can now be numerically integrated using Gaussian quadrature techniques.

For the crack-tip element on the upper crack surface, the standard mapping to  $\xi$ -space needs to be modified to accommodate the  $1/\sqrt{s}$  behavior of  $V_t(s)$  at the crack tip (see Fig. 2.9 (b)). The general approach is to split the  $V_t(s)$  term into a singular term multiplied by a non-singular coefficient. The form of  $V_t(s)$  follows from Eq. (2.25)

$$V_t(s)|_{\Gamma} = \frac{if(s)}{\sqrt{s}\sqrt{2L-s}} = \frac{1}{\sqrt{s}} F_1(s). \quad (2.32)$$

To map  $V_t(s)$  into  $\xi$ -space, the singular term uses an inverse mapping relationship and the non-singular term uses the quadratic shape functions. For the inverse mapping, the  $1/\sqrt{s}$  behavior is represented by placing the midnode of the quadratic element at the quarter point location

$$\xi = -1 + 2\sqrt{\frac{s}{L}} \rightarrow \frac{1}{\sqrt{s}} = \frac{2}{\sqrt{L}} \frac{1}{(\xi+1)}. \quad (2.33)$$

The Jacobian is given by

$$J = \frac{ds}{d\xi} = \frac{L}{2}(1+\xi). \quad (2.34)$$

Note that at the point where  $s = 0$  ( $\xi = -1$ ), the Jacobian also equals zero. This characteristic is important when evaluating the integral of the mapped function.

Therefore, the  $B_z$  contribution due to the crack-tip element on the upper crack surface is

$$\begin{aligned} B_z|_{\Gamma} &= -\frac{\mu_0 \sigma h}{4\pi} \int \frac{V_i(s)}{r(s)} ds = -\frac{\mu_0 \sigma h}{4\pi} \int_0^L \frac{1}{\sqrt{s}} \left( \frac{F(s)}{r(s)} \right) ds \\ &= -\frac{\mu_0 \sigma h}{4\pi} \int_{-1}^{+1} \frac{2}{\sqrt{L}} \frac{1}{(\xi+1)} \left[ N_1(\xi) \left( \frac{F(s)}{r(s)} \right)_{s_1} + N_2(\xi) \left( \frac{F(s)}{r(s)} \right)_{s_2} + N_3(\xi) \left( \frac{F(s)}{r(s)} \right)_{s_3} \right] \frac{L}{2} (\xi+1) d\xi \\ &= -\frac{\mu_0 \sigma h}{4\pi} \sqrt{L} \int_{-1}^{+1} \left[ N_1(\xi) \left( \frac{F(s_1)}{r(s_1)} \right) + N_2(\xi) \left( \frac{F(s_2)}{r(s_2)} \right) + N_3(\xi) \left( \frac{F(s_3)}{r(s_3)} \right) \right] d\xi. \end{aligned} \quad (2.35)$$

Also note that as  $\xi \rightarrow -1$ , the singularity term ( $\xi+1$  in denominator) goes to infinity but is canceled by the Jacobian term ( $\xi+1$  in numerator) going to zero, thereby making the overall function finite in the mapped space. All values of  $F$ ,  $r$ , and  $s$  are known, including  $F(s_1) = K^+/\sqrt{2\pi}$  (from Eq. 2.27) at the crack tip node that has the singularity. The crack-tip numerical integration using the quadratic interpolation functions and the quarter-point formulation used in the model was verified against an integrable test case having the same singular behavior as Eq. (2.24)

$$\int_0^a \frac{1}{\sqrt{a^2 - x^2}} = \sin^{-1} \frac{x}{|a|} \Big|_0^a = \frac{\pi}{2}. \quad (2.36)$$

### Using the Measurement Model

A computer program (Appendix B) has incorporated this BEM development into a simulated scan of a SQUID over a dc-current injected plate containing a crack. The program can accommodate various sample geometries and can include an interior boundary (*e.g.*, a fastener hole) if desired. Figure 2.10 shows the basic input variables.

Calculation of the magnetic field is a two step process. First the BEM subprogram must be run to solve for the potentials needed for the integrals involved in the magnetic field calculation. This step requires that a boundary mesh be generated reflecting the geometry of the sample. The crack is handled through the Green's function formulation and does not need to be modeled in this mesh.

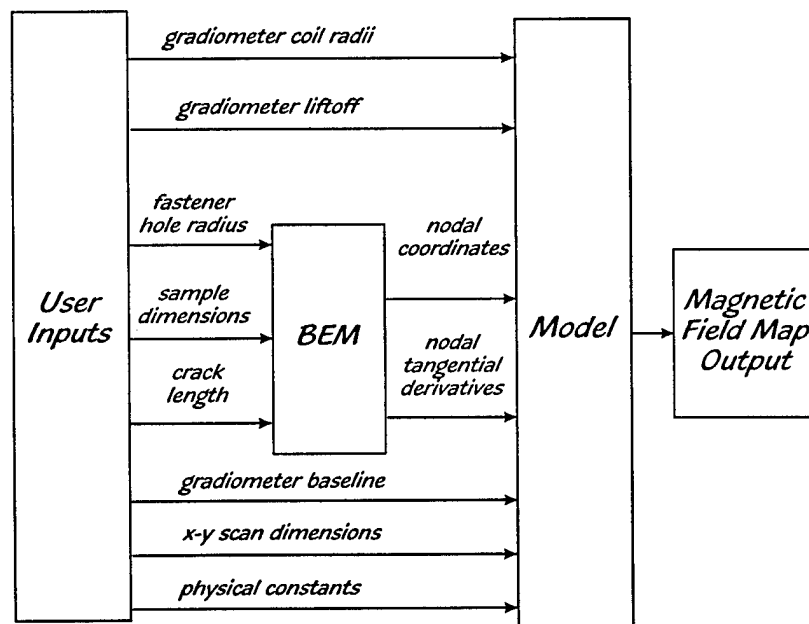


Figure 2.10 Input variables for BEM measurement model

Once the BEM subprogram has calculated the required nodal tangential derivatives, the measurement model then steps through each x-y scan coordinate and calculates the magnetic field contributions from the tangential derivatives at all the boundary nodes (crack and non-crack). The magnetic field is integrated over the areas of the gradiometer coils to determine net flux. This output is then plotted in the form of a 2-D magnetic field map.

If the measurement model is to be used to generate POD analysis data, the program is set up to loop, using the same BEM input file, while sampling from a noise (or system parameter) distribution in Monte Carlo fashion. The peak-to-peak value of the magnetic field is extracted from each 2-D scan (one Monte Carlo loop) and represents the signal used in the determination of POD. In this way, a distribution of signals can be generated for a single crack length. For each crack length, the BEM subprogram is run only once, then the signal distribution for that crack generated from the measurement model Monte Carlo loops. Calculation of the POD from this data is discussed in Chapter IV.

## CHAPTER III

### COMPARISON OF BEM MEASUREMENT MODEL TO EXPERIMENT

#### Comparison Issues

Several experimental measurements were compared to the BEM measurement model. There are some important issues affecting how closely the measurement model can represent the experimental measurement. Fabrication of test samples to be used specifically for comparison to models is usually a compromise between representing the ideal geometries used in the calculations and what is found in an actual aircraft structure. In addition, the uncertainties associated with taking experimental measurements make comparison as much a qualitative analysis as it is a quantitative one. These issues, and others, will be discussed in more detail in Chapter V.

Also, direct amplitude comparison requires accurate SQUID calibration factors. A description of a calibration procedure used in this laboratory is given in Appendix C. Only one of the following experimental comparisons utilized this factor.

#### Experimental Measurements

Experimental measurements were made using three different SQUID systems for comparison to the BEM measurement model. These experimental measurements do not necessarily validate the BEM measurement model but show that the model does do well in determining the magnetic fields associated with common test conditions found in the laboratory.



## Calibrated System: SBIR

A new optimization procedure was conducted for one channel of a 5-channel low- $T_c$  SQUID gradiometer system (termed SBIR SQUID) to determine an accurate value of the voltage-to-magnetic-field factor required to convert the output voltage of the SQUID to units of tesla, which is consistent with the measurement model. This was done so that at least one comparison based on accurate experimental signal amplitudes could be done. The other SQUIDs used in these measurements do not have optimized calibration factors at this time.

SBIR SQUID is documented as having an axial gradiometer with 5-mm diameter pickup and balance coils with a baseline of 20 mm. The calibration factor that was determined for channel 1 of SBIR SQUID is assumed to be independent of magnetic field source making it applicable to scanning samples with different associated magnetic fields. A measurement was made using a 100 mA dc current injected into a 100 mm  $\times$  150 mm  $\times$  0.03 mm copper clad circuit board containing a 9 mm diameter hole with a 9 mm  $\times$  0.03 mm slot on one side of the hole (see Figure 3.1). Although this setup does not provide completely uniform current injection across the sample (transverse to the slot) due to the point source electrodes, the region around the central region should be relatively uniform.

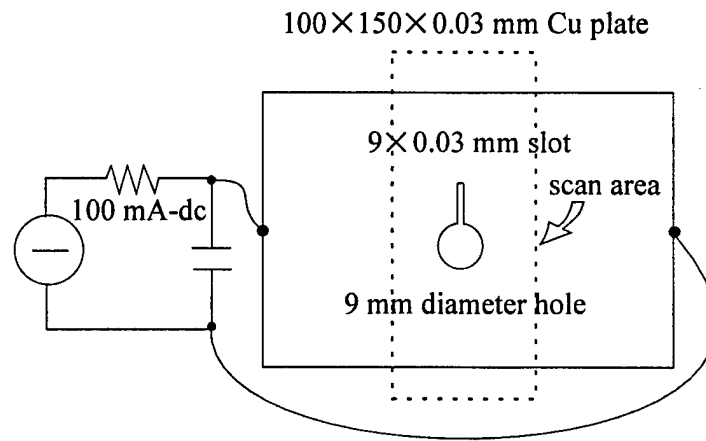


Figure 3.1 SBIR Experimental setup

Figure 3.2 shows the contour map resulting from a 2-D scan (unshielded environment) over the sample. The optimized parameters (pick-up coil radius = 2.8 mm, baseline = 2.06 cm, and liftoff = 14 mm) were used in the BEM measurement model and both magnetic maps compared. Figure 3.2 also shows the profile comparison, after scaling the experimental result with the optimized calibration factor ( $6.16 \times 10^{-8}$  T/V), corresponding to the line AA' on the contour map. At this large of a liftoff, the dipole signal does not reveal much about the hole/slot geometry but the interest here was to ensure that the measurement model was calculating field amplitudes correctly. Using the optimized parameters, the measurement model is within 2% of experiment (measuring  $B_{pp}$  of the dipole associated with the hole and slot). Some difference can be attributed to the assumption of uniform current density across the plate, which can have a large effect, and is most likely causing the amplitude error seen at both ends of the scan profile. The current density non-uniformity can also be seen on the experimental contour map as asymmetries in the contour lines. Errors in the optimized parameters or calibration

number would show up as a mismatch of the profiles in shape and amplitude beyond that attributable to experimental error.

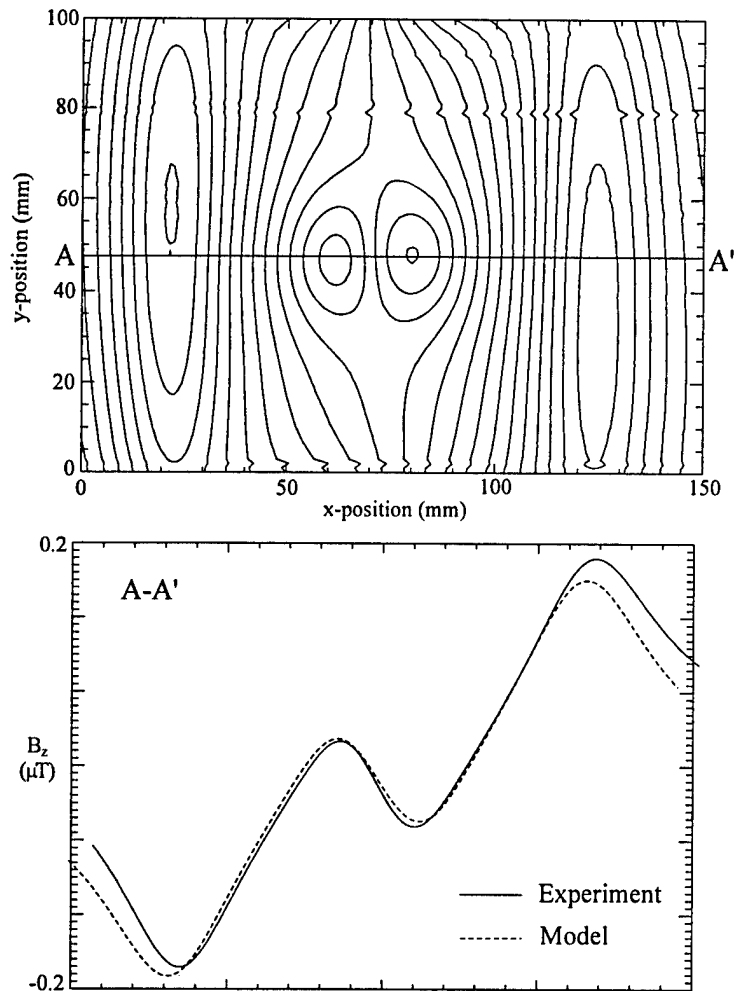


Figure 3.2 SBIR magnetic field contour map and comparison profile

### Measurements Using Other Systems

Other comparisons were made using SQUID systems that did not have optimized calibration factors. By scaling the amplitudes of the measurement model map to the experimental map, the use of the calibration factor was bypassed and then only shape comparisons were made.

### *MicroSQUID*

Using MicroSQUID, a comparison experiment used a 5 mA dc current injected into a  $75\text{ mm} \times 150\text{ mm} \times 0.03\text{ mm}$  copper clad circuit board containing a  $15\text{ mm} \times 0.03\text{ mm}$  slot cut with a scalpel (see Figure 3.3). Figure 3.4 shows the contour map resulting

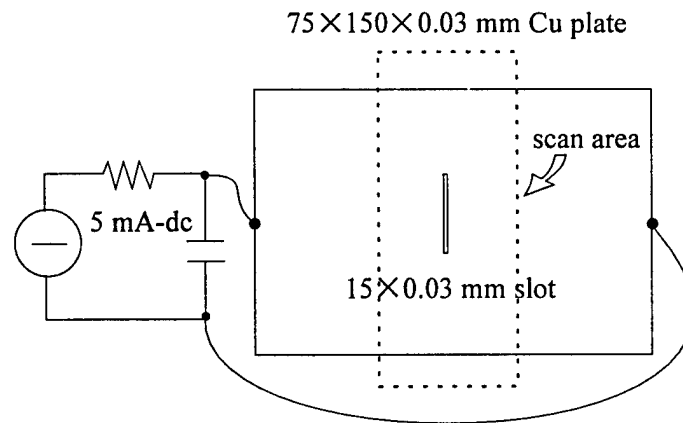


Figure 3.3 MicroSQUID: Experimental setup

from a 2-D scan (shielded environment) over the sample with the lines AA', BB', and CC'. Profiles along these lines on this map are compared to those calculated by the measurement model. Magnetic field shape characteristics (matching of peaks and valleys) reflect the accuracy of the measurement model since a difference between the model and experiment would show up as a mismatch of the profiles at either the edge or the crack locations. The measurement model is in very good agreement (only shape characteristics compared) with experiment for all profiles. A slight mismatch at the right side of AA' can be seen and is most likely due to a small variation in liftoff during a scan (i.e. sample not level).

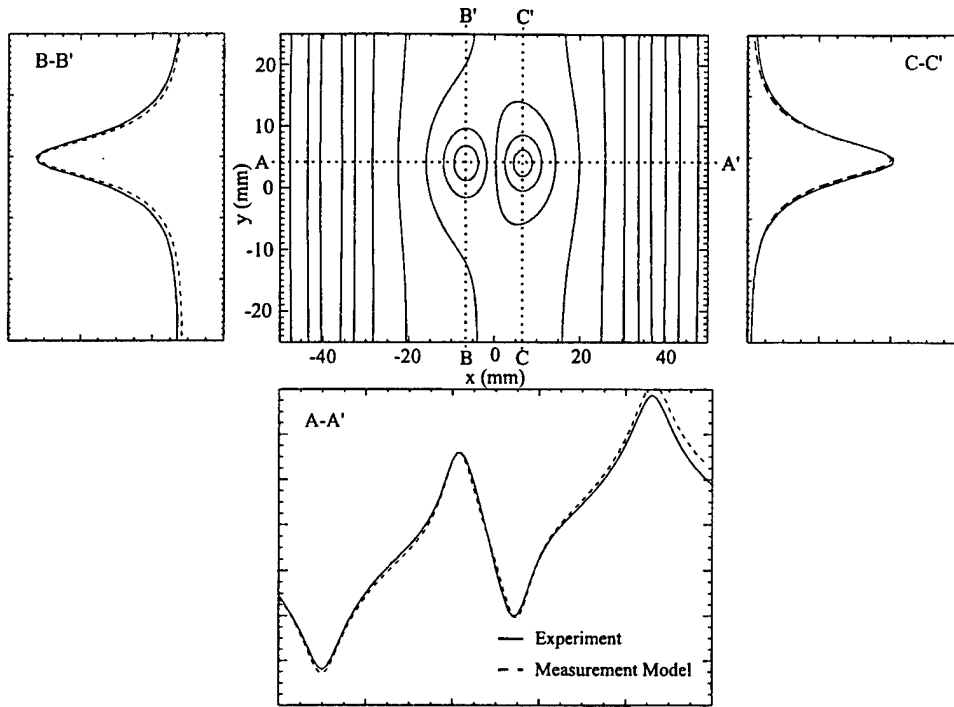


Figure 3.4 MicroSQUID magnetic field contour map and comparison profiles

### *Mobile HTS SQUID*

Another measurement used a 50 mA dc-current injected into a 100 mm  $\times$  150 mm  $\times$  0.03 mm copper clad circuit board containing a 9 mm diameter hole with a 9 mm  $\times$  0.03 mm slot on one side of the hole (see Figure 3.5). However, the SQUID used for this measurement was a high- $T_c$  system [24] which used a planar gradiometer (the pickup and balance coils are in a plane parallel to the sample surface) instead of an axial one. Figure 3.6 shows the contour map resulting from a 2-D scan (unshielded environment) over the sample. The quadrupolar shape results from the planar gradiometer acting as a spatial differentiator and, by taking the derivative of the dipole-shaped magnetic signal, results in a quadrupole shape. Since the planar gradiometer was oriented parallel to the plate edges, the edge signal is approximately zero and therefore, only that part of the scan

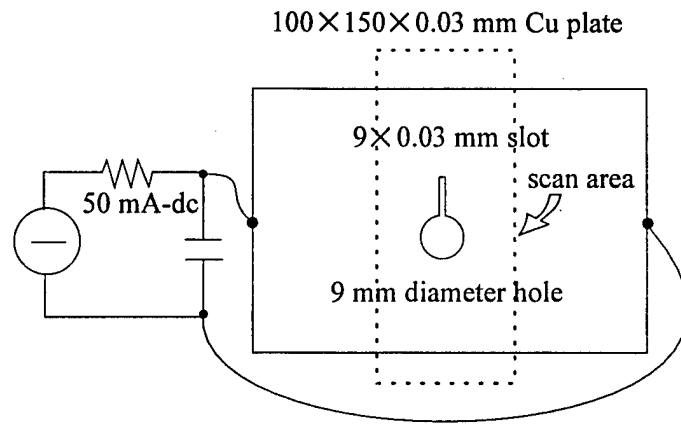


Figure 3.5 Mobile HTS: Experimental setup

above the hole/slot was used in these comparisons. Figure 3.6 also shows the profile comparisons, after scaling, corresponding to the lines AA', BB', and CC' on the contour map. The measurement model is in very good agreement (only shape characteristics compared) with experiment for all profiles. Again, a difference between the model and experiment would show up as a mismatch of the profiles at the location of the hole/crack.

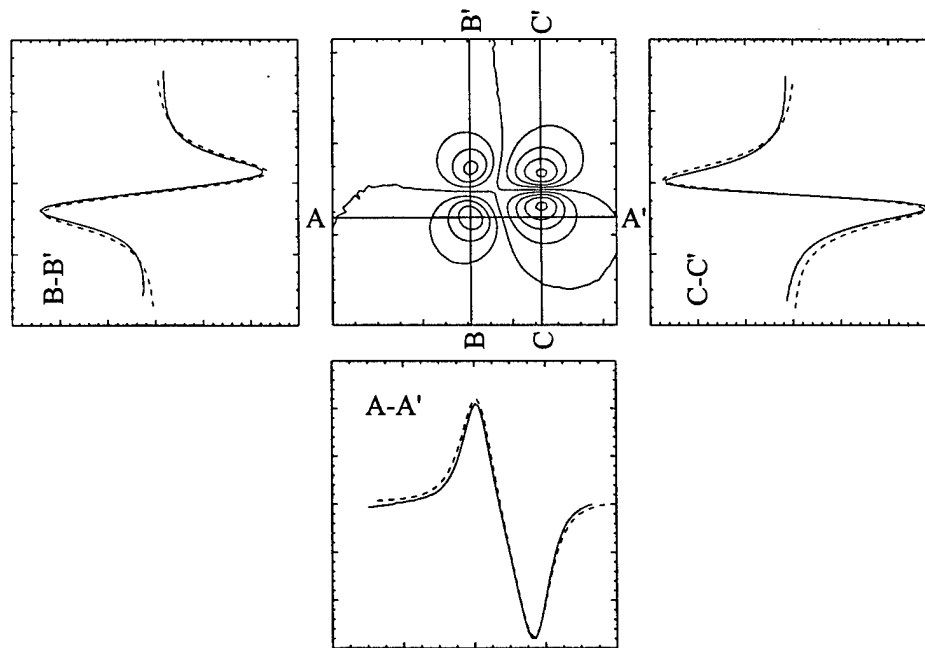


Figure 3.6 Mobile HTS magnetic field contour map and comparison profiles

## CHAPTER IV

### POD CURVES FROM SIMULATED EXPERIMENTAL DATA

#### Probability of Detection

##### Introduction

In general, inspection systems must use some criterion to “accept or reject” the part being tested. A threshold (associated with a minimum crack size) can be set so that the signals above the threshold are rejected and those below accepted. Figure 4.1 shows the cumulative distribution of rejected signals for a range of signals around the threshold. For an ideal inspection system, no signals below the threshold would be rejected and 100% of those above the threshold would be rejected. But, for real systems, uncertainties in the measurement process cause the curve to be rounded, creating two regions of error. False accepts (type I error) are signals above the threshold that are missed leading to issues of safety. False rejects (type II error) are signals below the threshold that are being unnecessarily rejected leading to issues of cost of repair or replacement.

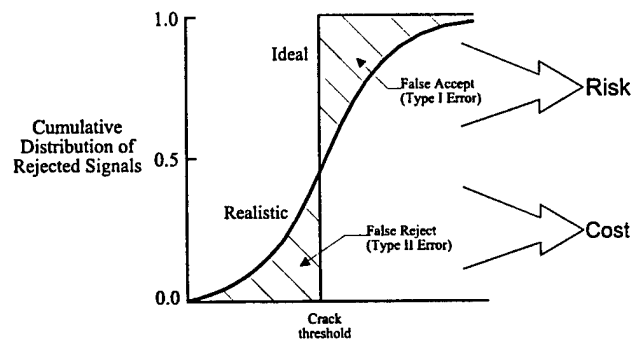


Figure 4.1 Cumulative distribution of rejected signals: real versus ideal

## Determination from Experimental Data

Determination of POD requires that the underlying signal distribution of the data be known (or assumed). The distribution of signals results from such things as sample related variability (*e.g.*, material properties, crack geometry and orientation) and measurement system variability (*e.g.*, sensor characteristics, liftoff, scanning, calibration, and different users). The  $POD(a)$  is determined by integrating this signal distribution,  $f_a(\hat{a})$ , above some specified signal threshold  $\hat{a}_{th}$ ,

$$POD(a) = \int_{\hat{a}_{th}}^{\infty} f_a(\hat{a}) d\hat{a} \quad (4.1)$$

as represented by the shaded areas in the upper part of Fig. 4.2. This integration is done at each crack length resulting in the POD curve shown in the lower part of Fig. 4.2.

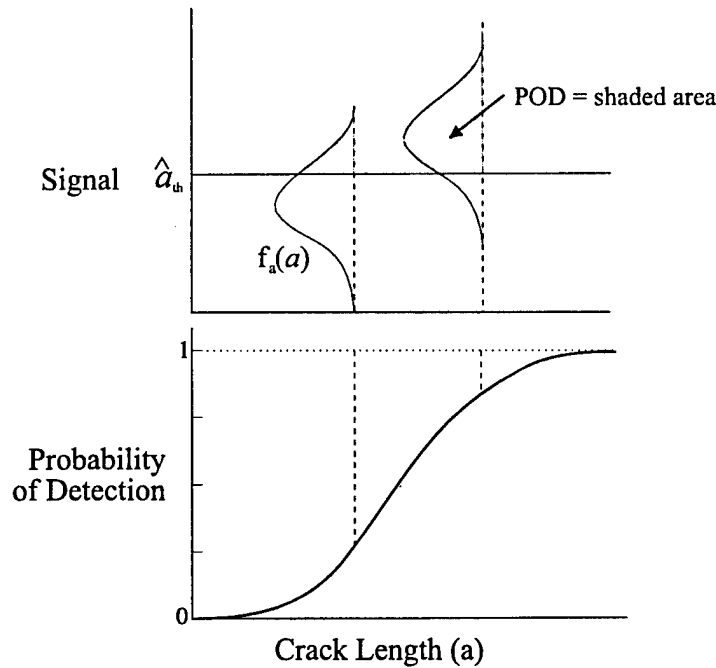


Figure 4.2 Integration of signal to determine POD



If the analysis is using simulated experimental data through use of the BEM measurement model and Monte Carlo methods, then the POD at a given crack length is determined through direct numerical summation of those signals above the threshold

$$POD(a) \propto \sum_N (\text{response signals} > \hat{a}_{th}). \quad (4.2)$$

This approach does not require that the distribution of the signals be known.

For real experimental data, it is commonly assumed that the distribution of signals at a fixed crack length,  $f_a(\hat{a})$ , is normally distributed. Then a functional form is used to determine POD. Previous studies [25] have shown that NDI experimental data commonly have a POD functional form that follows the log-odds or log logistic model

$$POD(a) = \left\{ 1 + \exp \left[ -\frac{\pi}{3} \left( \frac{\ln a - \mu}{\sigma} \right) \right] \right\}^{-1}, \quad (4.3)$$

where  $\mu$  represents the central location of the POD curve and  $\sigma$  is a measure of the flatness of the POD curve (larger  $\sigma$ , flatter POD curve). Another POD function that has been used [26] is the Weibull function

$$\begin{aligned} POD(a) &= 0 & a < \hat{a}_{th} \\ &= 1 - \exp \left[ -\left( \frac{a - \hat{a}_{th}}{\eta} \right)^\alpha \right] & a \geq \hat{a}_{th}, \end{aligned} \quad (4.4)$$

where  $\alpha$  is the bandwidth, and  $\eta$  is the central tendency of the POD function.

NDE reliability data normally falls into two types, either data in which the inspection result was recorded as pass or fail, meaning that a flaw was either found or not found, or data in which the measuring instrument signal  $\hat{a}$ , in response to an actual crack of

size  $a$ , was recorded. For pass/fail data, the distributional parameters (*e.g.*,  $\mu$  and  $\sigma$ ) for the POD function can be determined using maximum likelihood methods. Details describing these methods can be found in [25, 27]. For signal data, regression analysis can be used to estimate the distributional parameters. In this case, the log-odds model is reparameterized to

$$\ln \left[ \frac{POD(a)}{1 - POD(a)} \right] = \hat{\alpha} + \hat{\beta} \ln a$$

rewritten as

(4.5)

$$Y = \hat{\beta}X + \hat{\alpha} \quad \text{where} \quad Y = \ln \left( \frac{POD(a)}{1 - POD(a)} \right), \quad X = \ln a,$$

which shows that the data plots linearly in log-space and  $\hat{\alpha}$  and  $\hat{\beta}$  can be determined from linear regression.

SQUID systems measure signal type data as an output voltage proportional to the magnetic field being measured. Signal data has the advantage over pass/fail data since it contains more information and, as a result, requires a smaller minimum number of samples to conduct an analysis. For example, it is recommended [25] that at least 60 flaw samples be used for a pass/fail analysis versus 30 for an  $\hat{a}$  analysis. Other advantages of signal data include:

- The underlying assumptions of the POD model are easily tested with statistical tools.

Since the POD model is derived from the correlation of the  $\hat{a}$  versus  $a$  data, the assumptions concerning the  $POD(a)$  model can be tested using the signal data. Also, the pattern of  $\hat{a}$  shows the acceptable range of extrapolation.

- The decision threshold is set after the signals are recorded allowing examination of the effect of different settings on POD without rerunning the experiment.
- The POD model is valid over large flaw size range and it is not critical to obtain a larger sampling of flaws around the area of steep slope on the POD curve.

### Confidence Bounds

Aircraft requirements specify that a 95% confidence bound region be determined for these curves. For experimental data using the log-odds model, a method from [29] can be adopted to calculate the lower confidence bound. The  $\gamma$ -percent lower confidence bound is given by

$$POD(a) = \Phi(z_L), \quad (4.7)$$

where

$$z_L = \hat{z} - \sqrt{\frac{\lambda}{N} \left( \frac{\hat{z}^2}{2} + \frac{(X - \bar{X})^2}{SSX} + 1 \right)}$$

and

$$X = \ln a$$

$$\bar{X} = \frac{1}{N} \sum_{i=1}^N \ln a_i$$

$$N = \text{sample size}$$

$$\lambda = \gamma^{\text{th}} \text{ percentile of a } \chi^2 \text{ - distribution (2 dof)}$$

$$SSX = \sum_{i=1}^N X_i^2 - \frac{1}{N} \left( \sum_{i=1}^N X_i \right)^2$$

$$\hat{z} = \frac{X - \bar{\mu}}{\bar{\sigma}}.$$

For simulated data using the BEM measurement model, Monte Carlo simulations will be used to determine the 95% lower confidence bound and only require that the signal and noise distributions be known. This will be discussed further when these values are calculated in a later section.

#### Importance of Setting Threshold Value

It is important to note the dependence of POD on threshold value. The threshold value is primarily a function of background noise and the choice of the minimum signal-to-noise ratio for which a crack can still be seen. This is very dependent on the instrument, technique, and user of an NDE inspection system. The tradeoff with setting the threshold lower to increase POD for a particular crack length is the simultaneous increase of the probability of false alarms (POFA) arising from the background signal being mistaken for a crack signal. The POFA is calculated in the same manner as POD with the noise distribution being integrated above the threshold value.

$$POFA = \int_{\hat{a}_{th}}^{\infty} \text{Noise}(\hat{a}) d\hat{a} \quad (4.8)$$

Figure 4.3 shows schematically the normalized distributions of the background noise and the crack signal pointing out the regions of concern and shows the tradeoff between POD and POFA when decreasing the threshold.

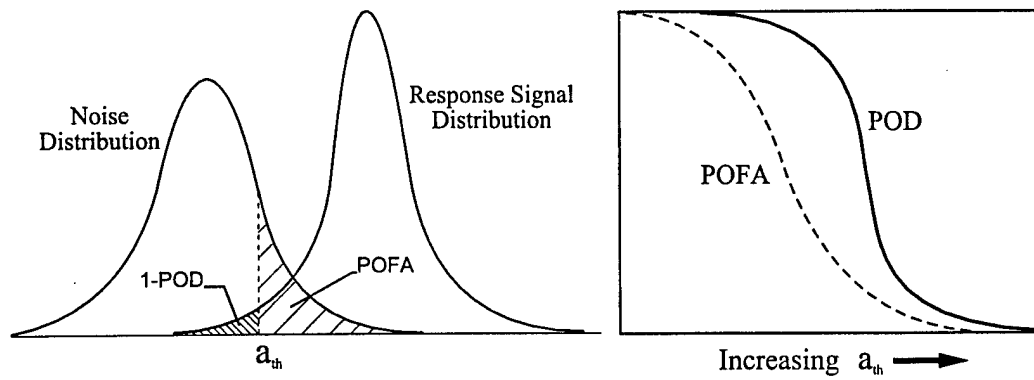


Figure 4.3 Effect of setting threshold value

### Progression of POD Approaches

The following discussion of some of the earlier POD approaches leads up to the present approach and points out some of the critical items that were important in deciding how best to determine POD for SQUID systems.

### Failure of Superposition

Initial POD work utilized a superposition model consisting of an elliptical crack superimposed on a hole in an infinite plate (refer back to Fig. 2.2). Superposition implies that the hole and the crack are behaving independently and do not influence each other when in close proximity. The errors associated with superposition approximations can be illustrated by direct comparison to the BEM model. Figure 4.4 displays centerline profiles for a 5 mm hole with a 5 mm crack at liftoffs of 3 mm and 1 mm revealing how the superposition approximation breaks down as liftoff distance is reduced.

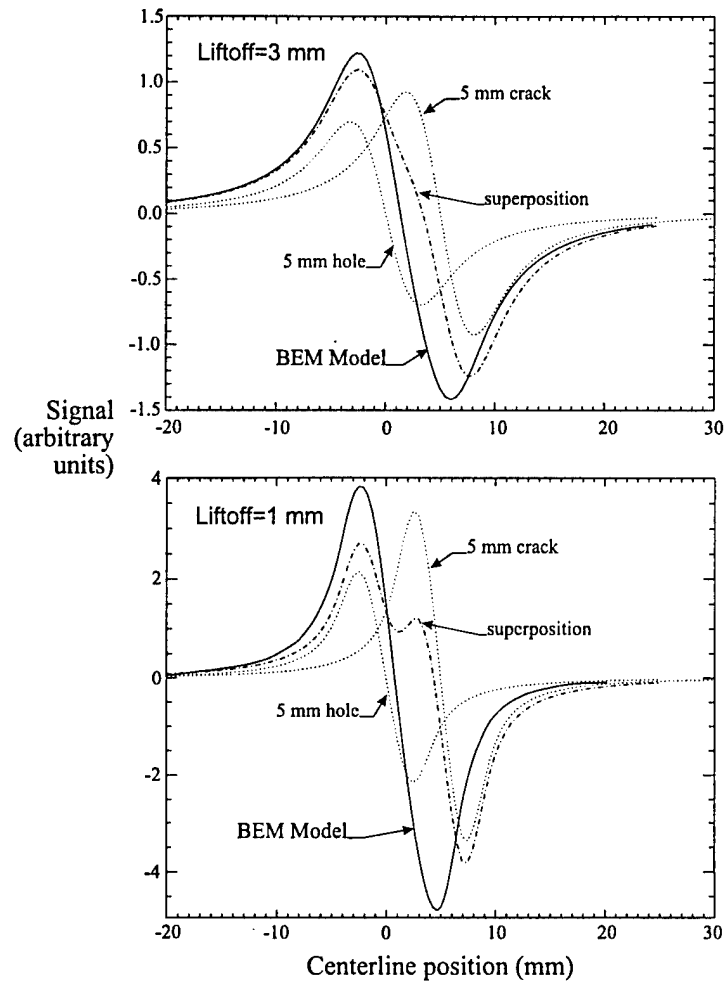


Figure 4.4 Comparison of BEM and superposition models

It is apparent that in these cases the hole-crack interaction cannot be neglected. However, for greater liftoffs and/or smaller crack lengths, the superposition model error is not as significant and may be used in calculating approximate fields. Figure 4.5 shows that for a smaller crack size of 3 mm, the superposition profile is not as distorted as compared to the 5-mm crack length case in the upper part of Fig. 4.4.

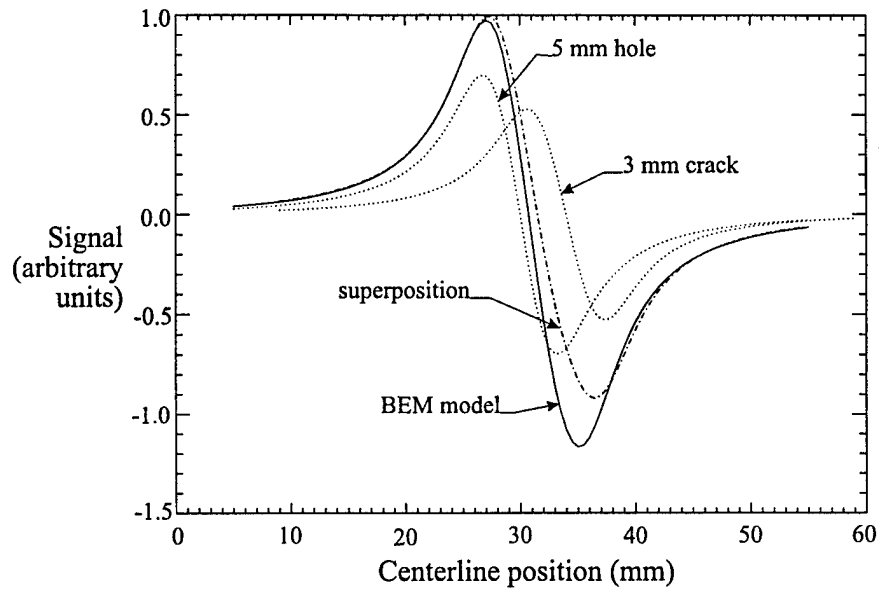


Figure 4.5 Comparison for a 5-mm hole with a 3-mm crack

#### Standard Hole Subtraction Technique

One analysis technique that was examined was that of subtracting a standardized hole from the hole-with-crack signal to extract that part of the signal due to the crack (see Figure 4.6). This was done by subtracting the 2-D magnetic map associated with a scan over a standard fastener hole from the 2-D map of the hole with crack. The resulting “residual” 2-D map could then be thought of as the magnetic field due to the crack alone. The peak-to-peak value of this residual map was defined as the crack signal.

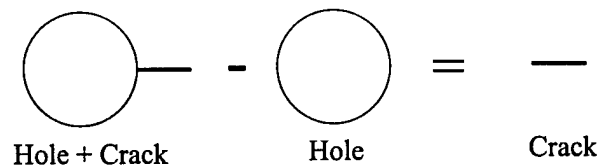


Figure 4.6 Subtraction of standard hole to extract signal due to crack

Unfortunately, in real experimental data, it is difficult to determine exactly where in the resulting magnetic map the hole is located so that there will be an uncertainty associated with this subtraction process. Figure 4.7 shows the sensitivity of the crack signal to the variation of the position of the subtraction hole. The left graph represents the crack signal (the “residual” signal) as the subtracted hole position was varied in a direction transverse to the crack. The right graph is determined the same way with the subtraction hole position varying this time parallel to the crack. The relative magnitudes of the crack signals for the two graphs show that the response surface was more sensitive to variation in the subtraction hole position in the direction parallel to the crack.

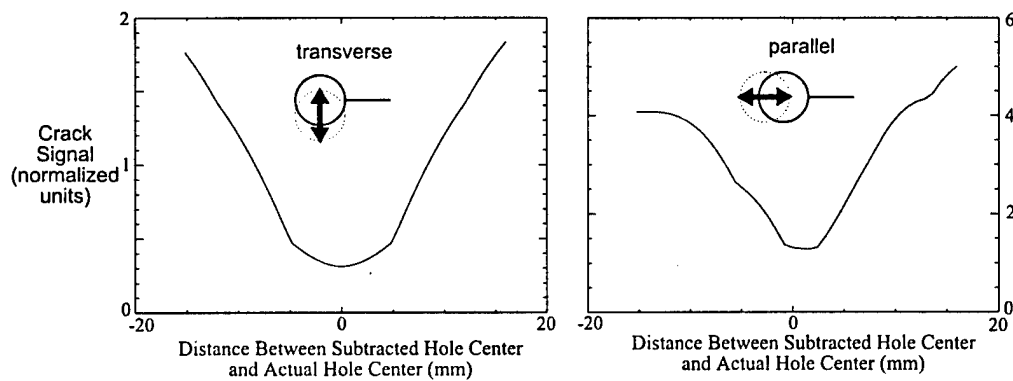


Figure 4.7 Crack signal dependence on subtraction hole position (Note the differing vertical scales)

Since the residual crack signal was dependent on the position of the subtraction hole, the POD was dependent upon the uncertainty associated with this subtraction process. For illustrative purposes, a distribution was placed on the subtraction hole position to simulate the experimental situation. An independent bivariate normal distribution,



$N(0, 1 \text{ mm})$ , was assumed for the subtraction hole position, then a sampling of 1000 random positions results in a distribution of residual crack signals shown histogram format in Figure 4.8.

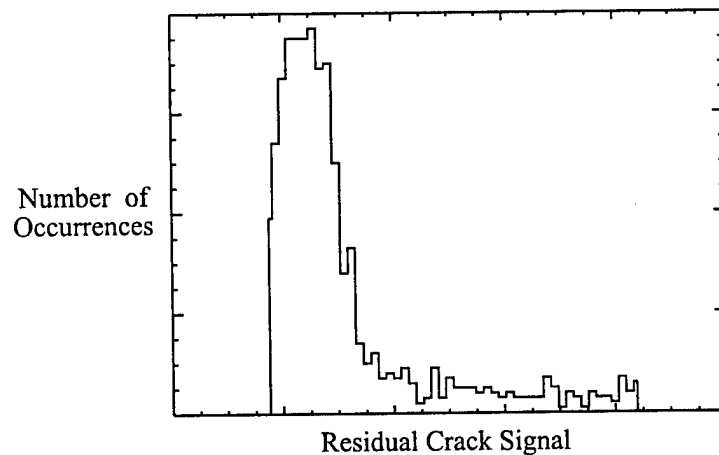


Figure 4.8 Histogram showing distribution of residual crack signals

The characteristics of this distribution arose from the behavior of the residual crack signal (variation shown in Figure 4.7) and the assumed distribution of the subtracted hole position. The sharp truncation on the left side of the distribution was a result of the residual crack signal having a local minimum around the actual hole center; any movement away from this center resulted in an increase in the residual crack signal. The peak/tail characteristic can be attributed to the assumed normal distribution of the subtraction hole position. If the assumed distribution had a larger than 1 mm standard deviation, the residual crack signal distribution would spread out more to the right but the truncation would remain fixed.

The POD at each crack length was determined by integration of the residual crack distribution, determined for each crack length, above a threshold as previously stated in Eq. (4.1). The threshold was set to satisfy  $SNR > 2$ .

The POD curve, a result of direct numerical summation of the Monte Carlo values, is shown in Fig. 4.9. It is common to assume that the crack signal distribution is Gaussian (normal). As a comparison, the distributions (like the one shown in Fig. 4.8) were fit with Gaussian distributions and a second POD curve determined. (also shown in Fig. 4.9). The correct POD curve (shown darker on the graph) has a sharp, asymmetrical shape. The sharp transition to a  $POD=1$  comes from the narrowness of the crack signal distribution and the asymmetry comes from the long narrow tail of this distribution. As can be seen, the normal distributions commonly assumed for these calculations might lead to significant error when calculating POD. The crack length values are retained for scale in this comparison and should not be used to infer SQUID performance.

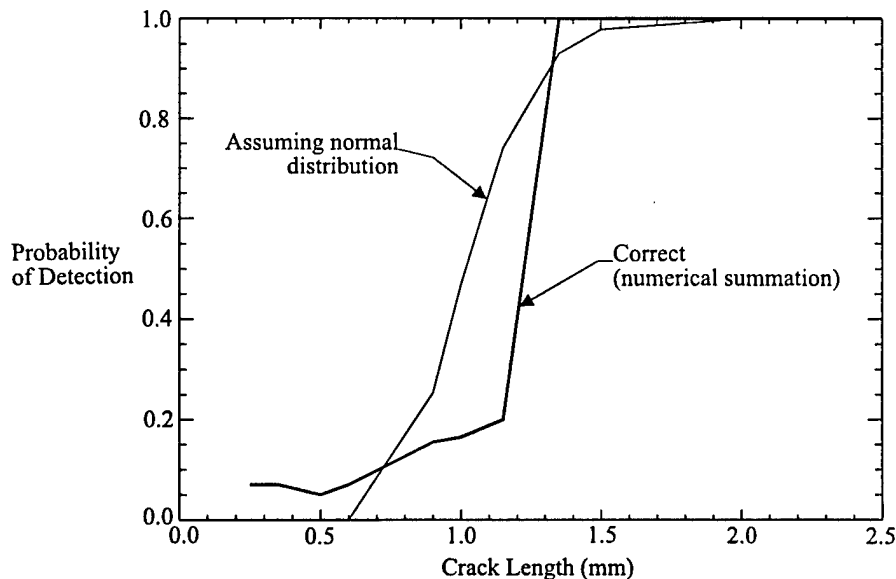


Figure 4.9 Calculated POD curves for hole subtraction scheme

### Present POD Approach

Since the hole subtraction process added additional uncertainty that negatively affected POD, it was desirable to be able to determine POD without this subtraction. It has been determined that POD can be calculated from the hole-with-crack signal directly. For this approach, the “signal” is no longer the peak-to-peak residual signal after subtraction, but the overall hole with crack peak-to-peak signal. Figure 4.10 shows the centerline profiles of the magnetic maps resulting from simulated scans over a hole with crack for four different crack lengths while keeping the hole diameter constant.

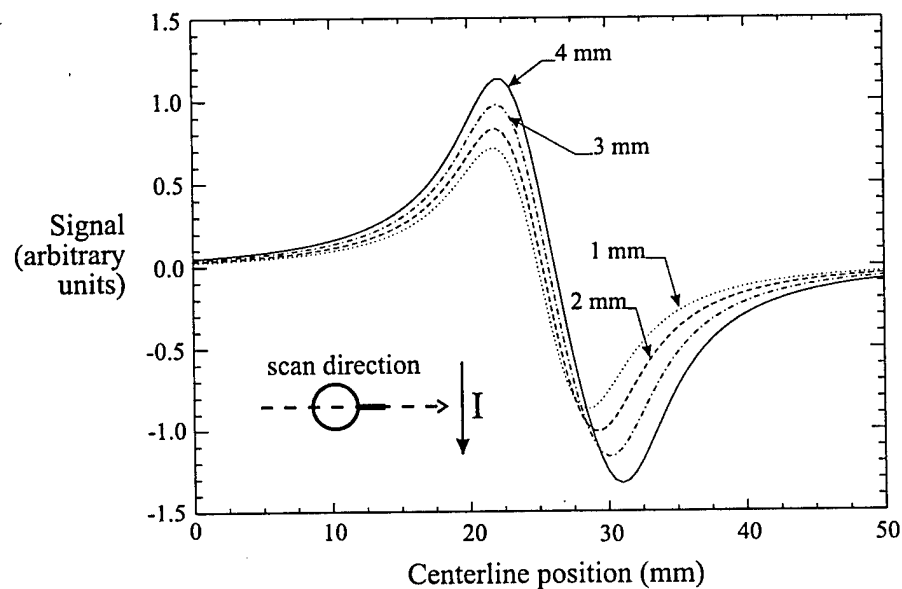


Figure 4.10 Scan centerline profiles for various crack lengths (with hole)

As can be seen, for increasing crack length, the signal amplitude increases. Also, the asymmetry increases, pulling the crack side of the dipolar signal to the right while the hole side remains relatively fixed. The important characteristic for POD is the increasing

peak-to-peak value as a function of crack length, which is the “signal” used in the POD analysis. The effect of increasing crack length on signal is apparent without subtracting a standard hole. For comparison, Fig. 4.11 shows the corresponding scan profiles for cracks alone with no fastener hole (normalized units of signal are on the same scale). Here, the profiles are symmetrical but still show the important characteristic of increasing amplitude for increasing crack length. Either type of data (Fig. 4.10 or 4.11) can be used to calculate POD.

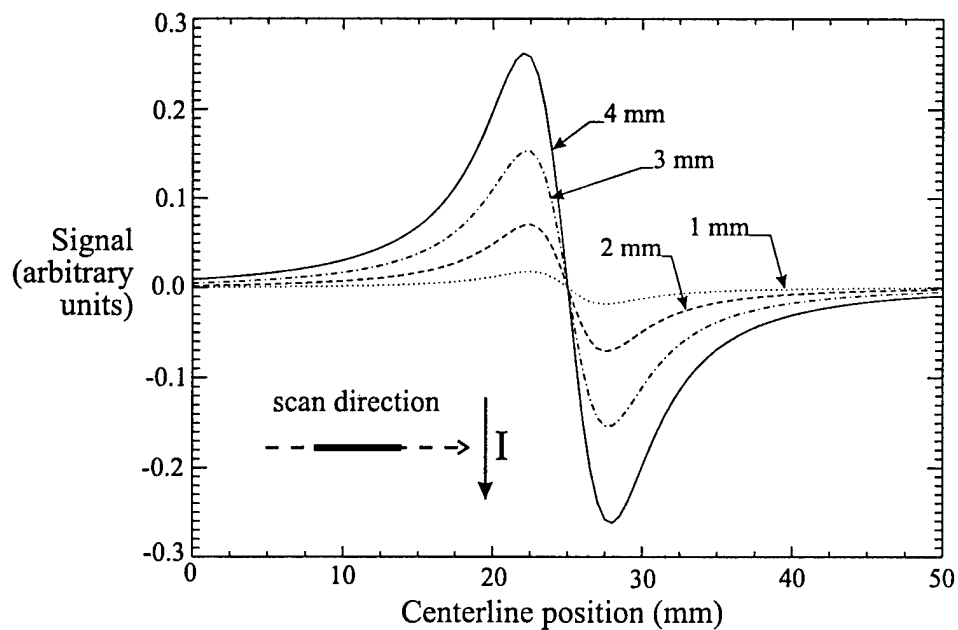


Figure 4.11 Scan centerline profiles for various crack lengths (no hole)

When the peak-to-peak signals from Figs. 4.10 and 4.11 are plotted as a function of crack length, comparisons can be made between the two (see Fig. 4.12) at a given liftoff (each liftoff distance would have a corresponding curve). The crack-only case can be shifted by adding the signal from a hole with no crack (corresponding to the hole-with-crack case at crack length = 0; in this case, a signal value  $\approx 1.5$ ).

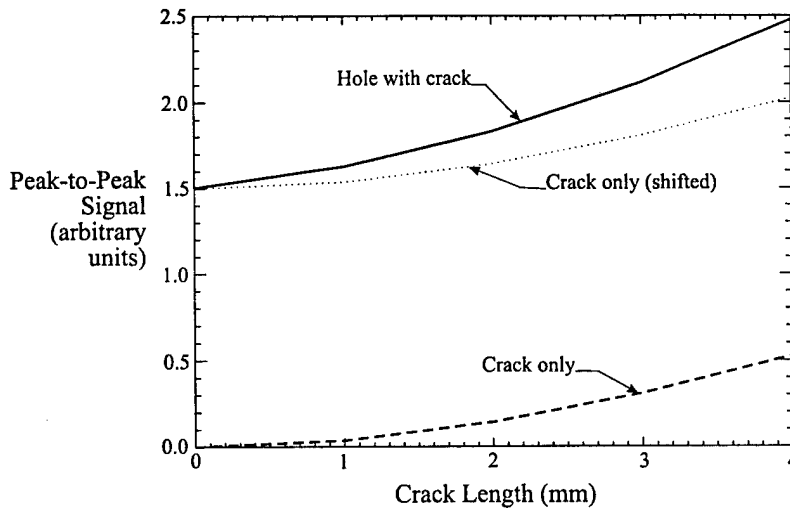


Figure 4.12 Signals as a function of crack length

Looking at this shifted curve, it is important to notice that the addition of a “standard” hole to the crack signal is not equivalent to the corresponding hole with crack. The unusual characteristic of Fig. 4.12 is that the BEM model results in signals that increase more quickly as a function of crack length than with the cracks alone. This is saying that it is easier to see a 3 mm crack on a fastener hole than it is to see a 3 mm crack by itself. This also points out that the hole subtraction scheme discussed earlier will not result in signals representative of cracks alone and would only work if the principle of superposition applied where the hole and the crack behave independently. Instead, the hole and the crack are not independent, in fact, the existence of the hole seems to enhance the detection of the crack. It has been suggested that the hole may be a “crack amplifier” due to the hole’s influence on the current density in the region near the crack causing the larger signal as compared to the signal from a crack alone of the same

size. This can be illustrated by looking at the current flow (potential streamlines) using the relation (normalized to the free stream current density)

$$\psi(r) = r \left( 1 - \frac{R^2}{r^2} \right) \sin \omega . \quad (4.9)$$

These were plotted (constant values of  $\psi$ ) for a region around the fastener hole in Fig. 4.13 and shows the current density concentration. For current injection transverse to the crack, the crack is located directly in the region of high current density possibly causing the greater signal

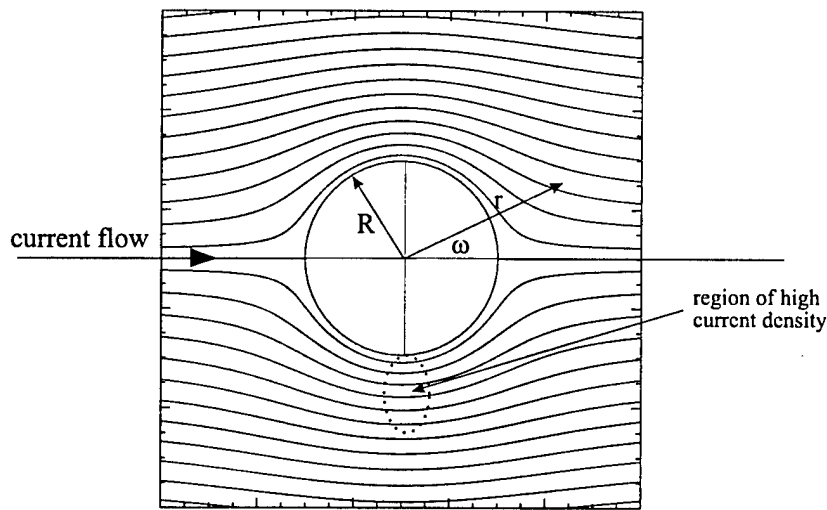


Figure 4.13 Current flow concentration around fastener hole

contribution observed in the hole-with-crack case. The variation in current density can be determined by differentiating Eq. (4.9) in this region ( $x = 0$ ) with respect to the radial direction transverse to the current flow.

$$\psi(r) = r \left( 1 - \frac{R^2}{r^2} \right) \sin \omega$$

at  $\omega = 90^\circ$ ,  $\sin \omega = 1$ ,  $r \rightarrow y$

$$\frac{d\psi(y)}{dy} = \frac{d}{dy} \left[ y \left( 1 - \frac{R^2}{y^2} \right) \right] = 1 + \frac{R^2}{y^2}$$
(4.10)

For  $y \geq R$ , Fig. 4.14 shows that the current density doubles at the surface of the hole and approaches one away from the hole.

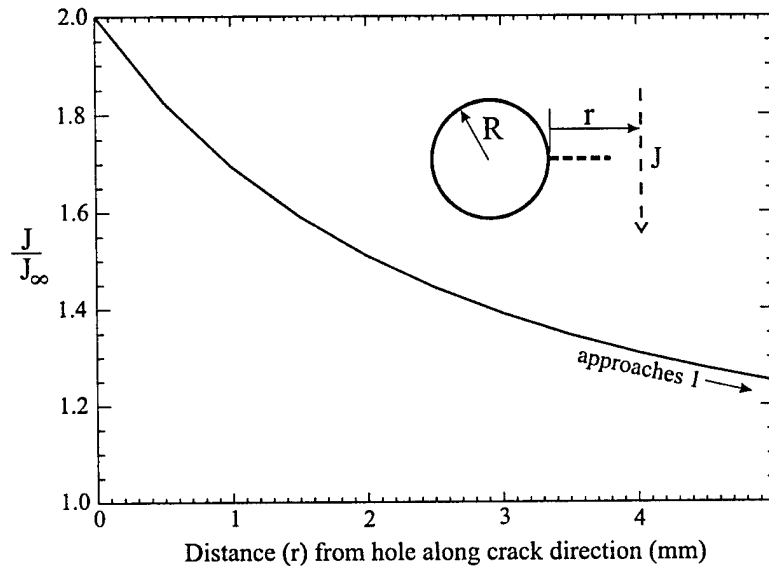


Figure 4.14 Current density concentration near fastener hole ( $R = 2.5$  mm)

One item to mention here is how this may affect the superposition model used previously. Since the current density concentration was not taken into account in that model, the contribution of the crack (thin ellipse) may have been underestimated. If we refer back to Fig. 4.5, we can see that the right side of the superposition curve undershoots the BEM result. By considering the current density concentration, this error may be less. But, it is not simply a multiplicative factor associated with Fig. 4.14 (*e.g.*, a factor of two near the fastener hole) since this would scale the entire dipole signal

associated with the crack and the superposition would then *overshoot* the BEM result on the left side of the profile curve. It might be possible to determine some kind of weighting function along the length of the superposition crack (heavier at the end farthest from hole down to a value of 1 at the end closest) but, this is simulating something more like a “crack-tip current concentration factor” and this is already handled with the BEM formulation. However, approximations could be made for a limited range of uses if so desired.

For illustrative purposes, a representative signal distribution and noise threshold were selected and applied to both the hole-with-crack and crack-alone cases. Figure 4.15 shows Fig. 4.12 with the appropriate thresholds and signal distributions sketched in. In this way the effect of the current density concentration on POD can be examined since it is assumed that both cases have the same signal and noise distributions. It can be seen that the standard hole signal level defines the new baseline for the hole-with-crack case. Experimental techniques exist [30] which can measure both the maximum signal from the hole with crack and the baseline signal simultaneously. However, in the case of a real crack, current injected parallel to the crack will still result in a signal contribution from the crack (versus zero contribution in the BEM measurement model) so, the baseline signal from a hole alone will have an associated uncertainty affecting probability of detection. The SNR threshold is the same for both of the cases since the SNR is a function of the measurement instrument, not the sample. Also, the signal distribution at a fixed crack length would be the same for both cases unless the distribution was dependent on the fastener hole (*e.g.*, uncertainty in size or roundness). Usually, this signal distribution is dependent on uncertainties in parameters common to both samples



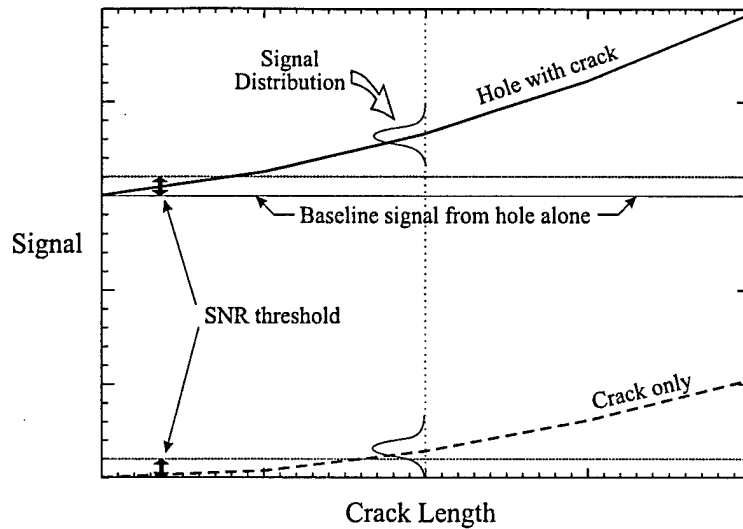


Figure 4.15 Determining POD from signal curves

(e.g., uncertainties associated with the scanning process or the instrument). POD determination is the same for both curves; the integration of the signal distribution above the SNR threshold (see Eq. 4.1 and Fig. 4.2). Due to the interaction of the crack and the hole, the POD values will not be equal (notice the difference in the amount of the distribution above the threshold for each case in Fig. 4.15) but, they *both* are valid measures of POD as a function of crack length. The calculated POD curves from these two cases are shown in Fig. 4.16. The difference in the curves results from the hole/crack interaction, not a difference in how the “signal” was defined, and shows that the hole enhances the probability of detection. Again, the crack length values are somewhat arbitrary, since the distribution was chosen for illustrative purposes only but they offer a sense of scale to the comparison.

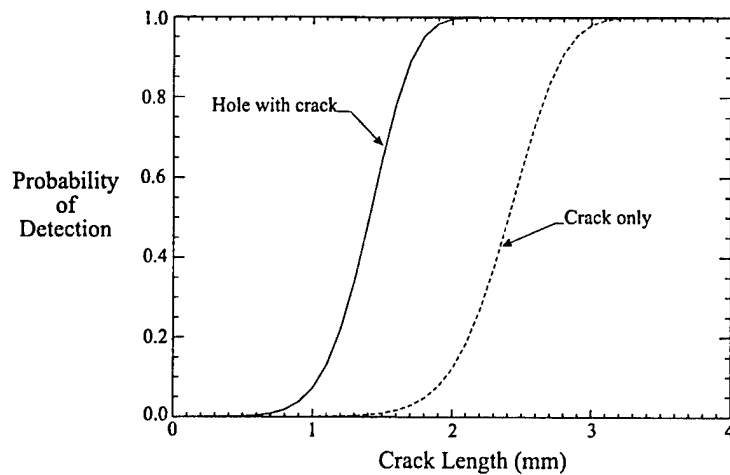


Figure 4.16 Resulting POD curves for both cases

The hole-with-crack POD curve shows that a hole with a crack has a smaller minimum detectable flaw size than the crack only for a given probability of detection. This is directly due to the hole/crack interaction. The effect of the hole increasing the current density concentration has a significant effect on the POD. Even though the POD curves resulting from these cases can be compared in terms of detectability, the hole/crack interaction does not allow direct comparison by use of a baseline hole signal to shift one curve (unless you completely understand this interaction). SQUID performance will have to be determined separately for each kind of crack type (with hole or without hole).

#### Determination of POD Curves

Now that the “signal” has been defined to be that coming from the hole with crack, POD can be determined from the hole-with-crack signal distribution (resulting from the uncertainties in the system parameters). Sensitivity analyses will be done on

selected system parameters to determine how they affect the overall signal distribution. Monte Carlo simulations using this signal distribution and experimental noise distributions will generate realistic POD curves.

### System Parameter Uncertainty

System parameter uncertainty can lead to intrinsic noise associated with the measurement process. The uncertainty in a parameter manifests itself in the signal distribution. To determine POD, the effect of the uncertainty in each system parameter must be examined to determine the overall signal distribution. The BEM measurement model can be used as a sensitivity analysis tool to look at how the magnetic field varies when a system parameter is perturbed within a range associated with the parameter's uncertainty. The measurement model can be thought of as representing an  $n$ -dimensional response surface  $\Psi$  where  $n$  represents the total number of independent parameters used in the model (*e.g.*, liftoff, crack length, and pick-up coil diameter). For a response surface comprised of  $n$  variables,  $x_j$ , such that

$$\Psi = \sum_{j=1}^n c_j x_j, \quad (4.12)$$

the first order physical sensitivity factor,  $PS_j$ , is defined as

$$PS_j = \frac{\partial \Psi}{\partial x_j} \approx \frac{\Delta \Psi}{\Delta x_j} \text{ for } j = 1, \dots, n, \quad (4.13)$$

and the mean,  $\mu_\Psi$ , and variance,  $\sigma_\Psi^2$ , of  $\Psi$  are related to the mean,  $\mu_j$ , and variance,  $\sigma_j^2$ , of each of the variables through the relations

$$\begin{aligned}\mu_{\Psi} &= \sum_{j=1}^n c_j \mu_j \\ \sigma_{\Psi}^2 &= \sum_{j=1}^n (PS_j)^2 \sigma_j^2.\end{aligned}\tag{4.14}$$

By looking at the combined effect of the physical sensitivities (the  $PS_j$ 's) and the distributional characteristics (the  $\sigma_j$ 's) of the system variables, along with some insight obtained by understanding the underlying physical principles, we can identify factors which influence the POD distribution most. Those system parameters that have a relatively large  $PS_j$  (sensitivity analysis will show a steep slope on the response surface) or  $\sigma_j$  (system parameter distribution will be spread out) will be most important in the determination of POD distributions and need to be identified either through analytical or experimental means. It may be necessary to treat certain aspects of the inspection process as "black boxes" (*e.g.*, data acquisition hardware) and examine outputs as a function of inputs without mathematically modeling them. Equation (4.14) requires that the distribution characteristics of each parameter be determined or estimated in order to define the overall signal distribution used in calculating POD. The following sections will examine the parameters of scan resolution, plate thickness, pick-up coil liftoff and pick-up coil tilt angle. The uncertainties associated with these parameters will be stated in terms of the error (denoted  $\Delta B_{pp}$ ) in the total peak-to-peak value of the magnetic field  $B_{pp}$ . These distributions are all determined for a liftoff at or near 3 mm (minimum distance for our SQUID systems) to represent the maximum capability. For other liftoffs, the sensitivity analysis would have to be done again to generate a new set of error distributions.

### *Scan resolution uncertainty*

When a sample is scanned under the SQUID, the user-defined x-y grid of the scan determines at which locations data will be acquired. The spatial resolution of the image is very dependent on the fineness of the grid. It is common practice at Vanderbilt to use a 1-mm square pixel for scanning. Usually, to reduce the effects of noise, multiple data points are taken within the 1-mm pixel (in the scan direction only) and averaged to one value for that pixel. This digitization of the magnetic map can lead to errors in determining the signal since the actual dipole extrema are not likely to fall exactly on a grid point (see Fig. 4.17). The error is the greatest when the peak is in the middle of a pixel; half way between two of the scan lines in both of the  $x$  and  $y$  directions. If we look at the variation of the extrema values within a pixel region, the sensitivity of the signal,  $B_{pp}$ , to scan resolution can be estimated.

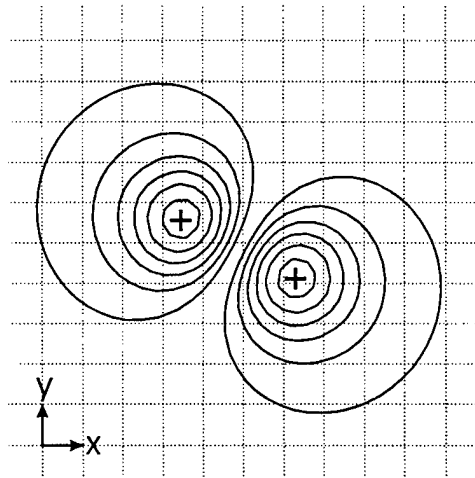


Figure 4.17 Dipole extrema scan resolution error

Figure 4.18 shows the maximum error, stated as a percentage of the total peak-to-peak value, for the dipole extrema associated with a 5-mm fastener hole with a 4-mm

crack at a liftoff of 3 mm. This error will have a strong dependence on varying liftoff since the shape of the dipolar peaks will change. The error will also be dependent on increasing crack length but to a lesser extent (see shape of peaks in Fig. 4.10). The dependence of scan resolution error on crack length is a subject of future work. The error in the peak-to-peak signal  $\Delta B_{pp}$  is shown for a 1 mm (scan pixel size) variation in the  $x$  and  $y$  directions (conducted independently) for both extrema. The maximum error for the peak-to-peak signal is the sum of the maximum errors for each extrema, for this case,  $\Delta B_{pp} \cong 1.6\%$ . For further liftoff distances, the peaks become less sharp which would reduce this error but the peak-to-peak amplitude decreases with a greater effect, causing the error to increase. For this same case, but with the liftoff increased to 6 mm,  $\Delta B_{pp} \cong 6\%$ .

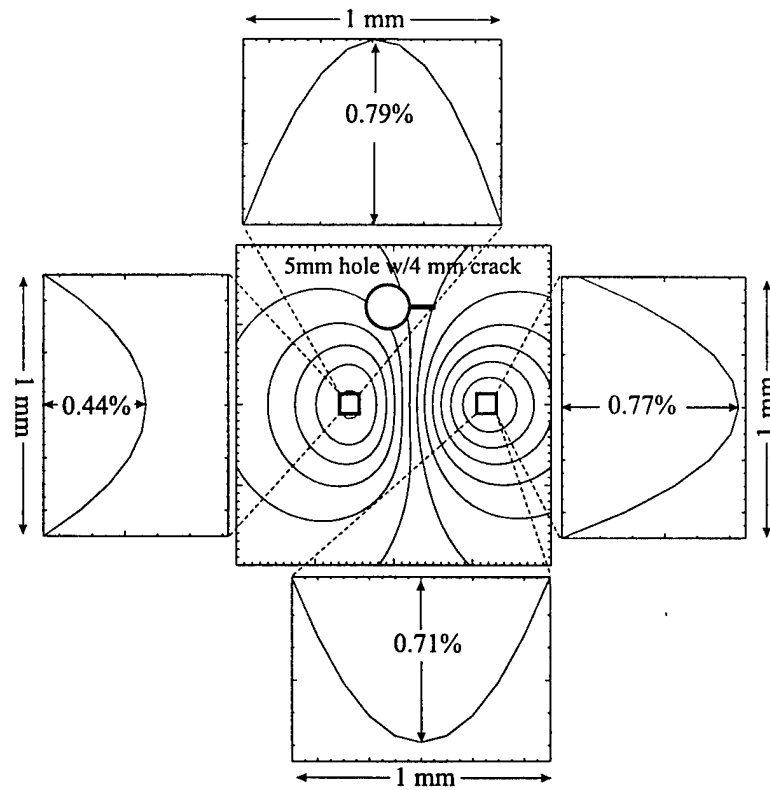


Figure 4.18 Error due to 1 × 1 mm scan resolution

Since it is equally likely that the dipole extrema will fall anywhere within the scan pixel, the distribution of  $\Delta B_{pp}$  associated with the scan resolution uncertainty can be approximated with a uniform distribution (in terms of  $B_{pp}$ ),  $\Delta B_{pp} = U(-0.016 B_{pp}, 0)$  for the 3-mm liftoff case. Scan resolution uncertainty always reduces  $B_{pp}$ , which explains the minus sign in the distribution.

One comment to make here is that spatial resolution is also a function of pickup coil diameter since the magnetic field is being integrated over the face of the pick-up coil. In other words, the magnetic *flux* is measured and represents an “averaged” magnetic field at that measurement point. A rule of thumb is to keep the scan pixel size smaller than the pick-up coil diameter. Pick-up coil flux integration was done for all calculations.

#### *Thin plate approximation and plate thickness uncertainty*

The approximations made in the measurement model formulation can lead to additional uncertainties in the calculated magnetic field. One approximation was made in the integration through the thickness of the plate (see Eq. 2.17,18). It was assumed that for a thin plate, the  $1/r$  term was approximately constant over the thickness (no  $z$ -dependence) and therefore  $d\Omega \rightarrow hds$  with the thickness  $h$  assumed constant. This reduced the surface integral (Eq. 2.17) to a contour integral (Eq. 2.18)

$$[\vec{B}_z(c)] = \frac{\mu_0 \sigma}{4\pi} \int_{\Omega} \frac{\vec{\nabla} V(Q) \cdot \vec{t}}{r(c, Q)} d\Omega \Rightarrow B_z(c) = \frac{\mu_0 \sigma h}{4\pi} \int_s \frac{\vec{\nabla} V(Q) \cdot \hat{t}}{r(c, Q)} ds(Q) \quad (4.15)$$

If we examine the effects of this assumption more closely, the limits of the thin plate approximation can be shown. The error arises from the dependence on  $r$ , which varies

over the thickness  $h$ , as shown with  $r_{upper}$  and  $r_{lower}$  in Fig. 4.19. Only  $r_{upper}$  was considered in calculating  $B_z$  from the contour integral, which was then multiplied by  $h$  to represent the “2-D” surface integration.

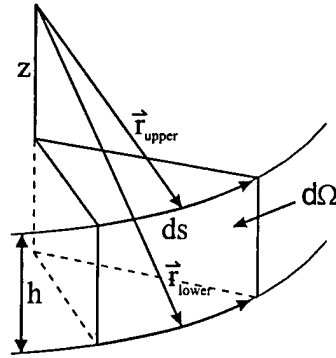


Figure 4.20 Integration approximation over plate thickness

By comparing  $1/r$  at the upper and lower contours, we can determine the magnitude of the error associated with this approximation

$$\begin{aligned}
 r_{upper} &= \left( (x_c - x)^2 + (y_c - y)^2 + (z_c - z)^2 \right)^{1/2} \\
 r_{lower} &= \left( (x_c - x)^2 + (y_c - y)^2 + (z_c - (z - h))^2 \right)^{1/2} \\
 &\quad \text{rewrite in terms of liftoff, } d = z_c - z \\
 &= \left( (x_c - x)^2 + (y_c - y)^2 + (d + h)^2 \right)^{1/2} \\
 &= \left( r_{upper}^2 + (2dh + h^2) \right)^{1/2} \\
 \therefore \frac{1/r_{upper}}{1/r_{lower}} &= \frac{r_{lower}}{r_{upper}} = \left( 1 + \frac{(2dh + h^2)}{r_{upper}^2} \right)^{1/2} = \left( 1 + \frac{2d}{r_{upper}} \left( \frac{h}{r_{upper}} \right) + \left( \frac{h}{r_{upper}} \right)^2 \right)^{1/2}.
 \end{aligned} \tag{4.16}$$

The maximum error is when  $r_{upper}$  is at a minimum,  $r_{upper} = d$

$$\left[ \frac{1/r_{upper}}{1/r_{lower}} \right]_{\max} = \left( 1 + 2 \left( \frac{h}{d} \right) + \left( \frac{h}{d} \right)^2 \right)^{1/2} = 1 + \frac{h}{d}. \tag{4.17}$$



If the liftoff is much greater than the plate thickness ( $d \gg h$ ), the ratio is approximately equal to one and the error would be small; this is the thin plate approximation. However, for increasing plate thickness for a given liftoff, the error increases (e.g., doubled at  $h = d$ ) and can no longer be considered negligible. At this point, the plate thickness should be subdivided into multiple layers (see previous Fig. 3.2) and the integration done separately at each successive layer, then added together (superimposed) to determine the total magnetic field.

The plate thickness approximation can lead to error in the calculated magnetic field but this can be treated more like a systematic error which does not vary if the scan geometry (e.g., liftoff) remains the same. From the standpoint of scan-to-scan uncertainty, it is the variation of or uncertainty in the plate thickness  $h$  which is of interest. For a constant value of injected current (measured in amps), a variation in  $h$  will cause the injected current density (measured in amps/m<sup>2</sup>) to change and thus affect the magnetic field amplitude. The magnetic field is directly proportional to the injected current density which is proportional to the plate thickness for a constant injected current and plate width

$$\frac{B_{pp}|_h}{B_{pp}|_{h+\Delta h}} \propto \frac{J_h}{J_{h+\Delta h}} = \frac{h + \Delta h}{h} = 1 + \Delta h/h. \quad (4.18)$$

A 1% variation in plate thickness will cause a 1% variation in  $B_{pp}$ . The variation could be a result of material processing, sample fabrication, or error when measuring the thickness of the plate. Estimating the uncertainty associated with a 1-mm plate to be  $\pm 0.05$  mm (10% variation),  $\Delta B_{pp}$  associated with plate thickness uncertainty can be approximated

with a normal distribution of  $N(0, 0.025 B_{pp})$ . The standard deviation of this distribution was determined by assuming that the maximum error (5%) is associated with the 2-sigma point (approximately 95%) of the  $\Delta B_{pp}$  distribution.

#### *Pick-up coil liftoff uncertainty*

The magnetic field is strongly dependent on the pick-up coil to sample distance (liftoff). The normalized peak-to-peak values as a function of increasing liftoff distance for a 3 mm diameter pick-up coil scanning over a 5 mm hole with three different crack lengths (2 mm, 3 mm, and 4 mm) are shown in Fig. 4.20. The inset graph shows a detail of the curves for the liftoff range of 3 to 4 mm. Within the range of 1 mm, the curves for the three crack lengths are approximately linear with a slope of 30%/mm. Normally, the liftoff distance can be determined within  $\pm 0.5$  mm and therefore, the greatest error due to uncertainty in liftoff would be  $\pm 15\%$ . By assuming that  $\Delta B_{pp}$  due to liftoff uncertainty is normally distributed, the approximate distribution for  $\Delta B_{pp}$  is  $N(0, 0.075 B_{pp})$ . Again, the maximum error (15%) is used as the 2-sigma point.

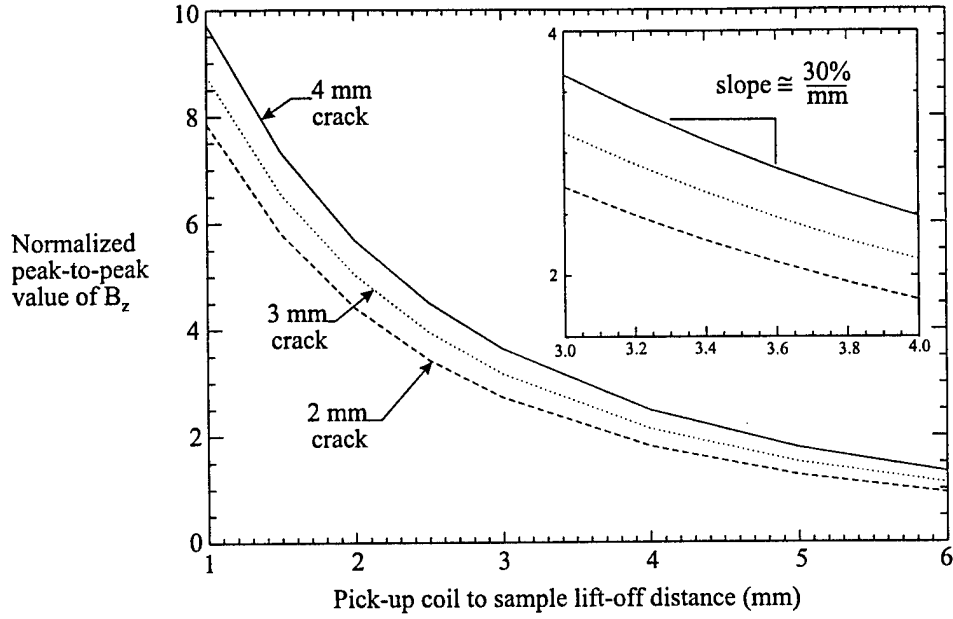


Figure 4.20 Sensitivity of  $B_{pp}$  to liftoff for various crack lengths

#### *Pick-up coil tilt angle uncertainty*

The BEM measurement model has assumed that only the  $z$ -component of magnetic field ( $B_z$ ) is being measured by the pick-up coil. If the pick-up coil is not parallel to the surface of the plate,  $B_z$  will be reduced and the other components of the magnetic field,  $B_x$  and  $B_y$ , will contribute to the signal. These components are associated with the  $\hat{i}$  and  $\hat{j}$  terms of Eq. (2.14)

$$\left( \hat{n} \times \frac{\nabla V}{r} \right)_{2D} = - \left( \frac{1}{r_t} - \frac{1}{r_b} \right) \left( n_z \frac{\partial V}{\partial y} \right) \hat{i} + \left( \frac{1}{r_t} - \frac{1}{r_b} \right) \left( n_z \frac{\partial V}{\partial x} \right) \hat{j} + \frac{1}{r_s} \left( n_x \frac{\partial V}{\partial y} - n_y \frac{\partial V}{\partial x} \right) \hat{k}. \quad (2.14)$$

Both terms have a common multiplier dependent on the pick-up coil distance to the top and bottom plate surfaces being integrated over. The effect of the multiplier on each of these components is similar to the previous discussion on the plate thickness approximation where the  $1/r$  values differed at the upper and lower contours at the edge

of the plate. Therefore, by similar derivation, the magnitude of the multiplier term is found to be dependent on the liftoff to plate thickness ratio.

$$\frac{1}{r_i} - \frac{1}{r_b} = \frac{1}{r_i} - \frac{1}{[r_i^2 + (2dh + h^2)]^{1/2}}$$

*greatest difference at  $r_i = d$*

(4.19)

$$\frac{1}{r_i} - \frac{1}{r_b} = \frac{1}{d} - \frac{1}{[d^2 + (2dh + h^2)]^{1/2}} = \frac{1}{d} \left( 1 - \frac{1}{1 + h/d} \right)$$

This multiplier is reduced even further when considering the geometric term associated with the coil tilt angle components in the x and y directions,  $\lambda_x$  and  $\lambda_y$ , shown here for the x-direction.

$$\left. \frac{1}{r_i} - \frac{1}{r_b} \right|_{\text{coil tilt}} = \frac{1}{d} \left( 1 - \frac{1}{1 + h/d} \right) \sin \lambda_x$$
(4.20)

It can be seen that for the thin plate approximation ( $h/d \ll 1$ ), this multiplier term is approximately equal to zero and there is basically no magnetic field contributions due to  $B_x$  and  $B_y$ . For plates where the thin plate approximation is not valid, the geometrical term associated with the coil tilt is the dominant reduction term. For example, a 2 mm thick plate at a liftoff of 3 mm yields  $0.13 \sin \lambda_x$ . For small tilt angles ( $< 5^\circ$ ), the  $B_x$  component would then be reduced by almost two orders of magnitude.

These two components appear to be negligible and therefore only the effect of pick-up coil tilt on  $B_z$  will be considered. The peak-to-peak value of  $B_z$  is reduced by a geometrical term associated with the tilt angle.

$$B_{pp} \Big|_{\text{tilt}=\lambda} = B_{pp} \cos \lambda$$
(4.21)

Tilt angle variability is small in the laboratory environment since the SQUID is stationary and samples are carefully leveled but, in the field this variability may be much larger.

For now, we will look at tilt angles  $< 5^\circ$ , which result in errors less than 0.5%. Since the tilt angle will always result in a reduction of  $B_{pp}$ , the distribution for  $\Delta B_{pp}$  is a truncated distribution (only negative values used) and is dealt with mathematically by taking negative values from  $N(0, 0.0025 B_{pp})$ .

### Noise Measurements

Noise distributions must be characterized in order to determine POD and POFA. Several noise distributions have been extracted from existing experimental data for different SQUID systems and measurement techniques. The measurement model simulates dc-current injection and experiments using direct dc-current injection have large noise distributions since they use the entire bandwidth of the SQUID (dc to  $\sim 10\text{kHz}$ ) and therefore, include noise over these frequencies as well. Noise conditions associated with other experimental techniques are more representative of what SQUID's will be operated in. Techniques based upon eddy current inducers [29, 24] use lock-in amplifiers at a particular frequency and greatly reduce the noise. Figure 4.21 shows a noise time series extracted from experimental data (dc-current injection in a shielded environment) by taking a single scan line away from any known flaw in the specimen being examined.

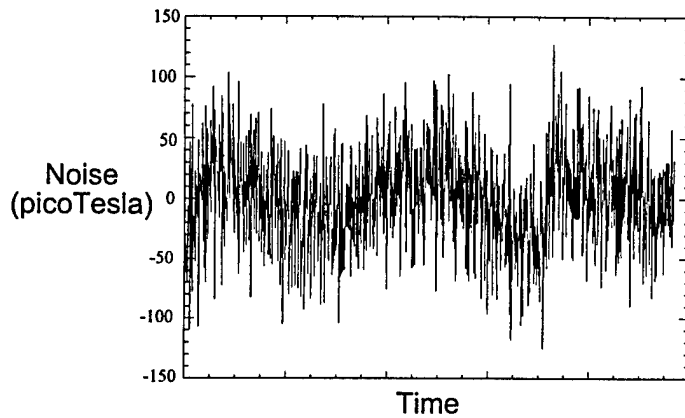


Figure 4.21 Experimental noise time series

As can be seen, the noise is approximately 100 pT peak-to-peak. A  $\chi^2$ -test confirmed that this noise distribution is normally distributed at a 5% significance level. With the inducing plate technique, use of the lock-in amplifier reduces this to about 5 pT peak-to-peak, a noise reduction factor of 20. Since we are also interested in taking measurements in an unshielded environment, noise distributions have been extracted from scan data taken using the same HTS-SQUID that was used in some of the experimental comparisons. Figure 4.22 shows noise time series for both the dc-measurement (upper) and the inducer measurement using the lock-in (lower). The dc-measurement data shows approximately 400 pT peak-to-peak noise while the lock-in measurement data shows about 2 pT, a noise reduction factor of 200! POD values determined using noise distributions similar to that shown in the lower part of Fig. 4.22 will represent present SQUID capability. Previous tests have shown that SQUID experimental noise can be assumed to be gaussian or “white” and therefore, the noise distribution used for dc-measurements was  $N(0, 58.48 \text{ pT})$  and for lock-in measurements was  $N(0, 0.475 \text{ pT})$ . These noise distributions were used in the following Monte Carlo simulation.

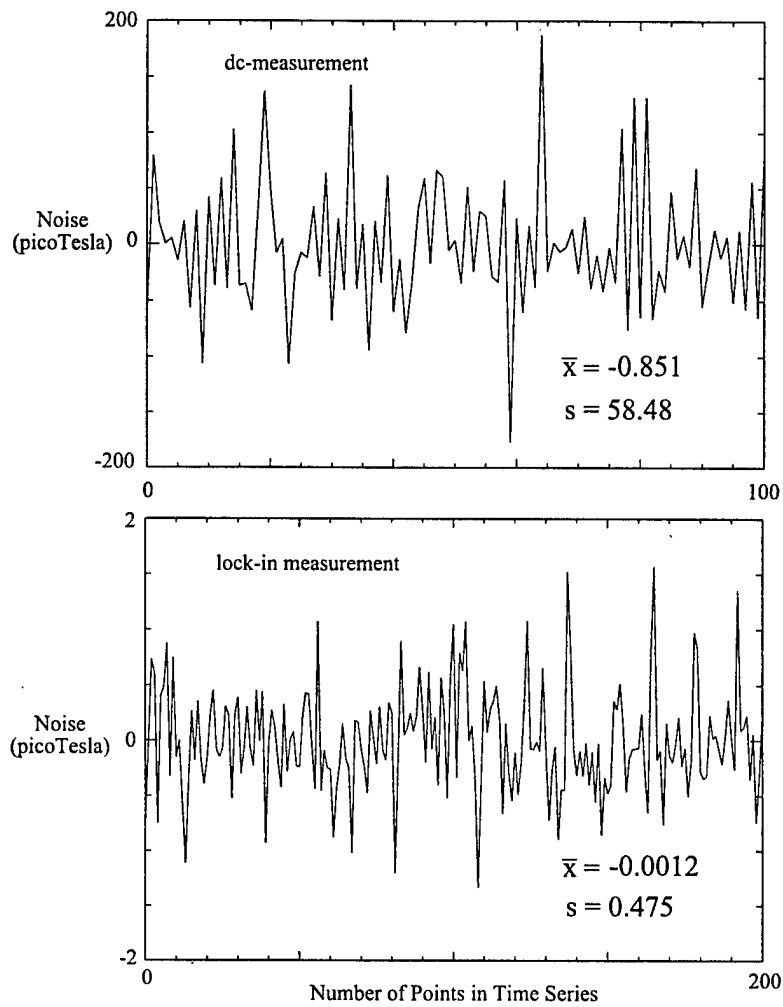


Figure 4.22 HTS-SQUID noise for dc (upper) and lock-in (lower) measurements

## Monte Carlo Simulation

### *A realistic test scenario*

Signal strength is dependent on the amount of dc-current injected into the sample. When using the standard dc-current injection technique, it is a common approach to increase the current until adequate SNR's are achieved, making POD primarily dependent

on how large a current source one might have. However, the dc approach is not practical and is not likely to be used in field applications. Instead of simulating dc-current injection directly, the BEM measurement model will be used to approximate the fields associated with the eddy-current inducing plate [29] mentioned earlier which produces “dc-like” currents within the sample. To do this, an estimate of the current density must be made from [30] to calculate magnetic fields of the correct magnitude. The inducing plate normally carries a current of approximately 0.04 mA/mm. This produces eddy currents on the order of  $0.01 \text{ mA/mm}^2$  in the top 1 mm of an aluminum plate. Unfortunately, for the thinner plates commonly found in aircraft fuselage lap joints, the eddy currents in the bottom of the plate (in the opposite direction) reduce the overall signal by about 40% for a 1 mm plate. This yields a final estimate of current density of  $0.006 \text{ mA/mm}^2$ . This is a representative value associated with state-of-the-art detection techniques used in SQUID NDE.

The test sample geometry used for these simulations was a  $1\text{-m}^2$ , 1-mm thick aluminum plate containing a 5-mm fastener hole with crack lengths ranging up to 4 mm. A uniform dc-current of  $0.006 \text{ mA/mm}^2$  was injected in a direction transverse to the crack for maximum signal. The modeled SQUID system utilized a 3-cm baseline axial gradiometer with 3-mm diameter pick-up and balance coils. The plate was scanned using  $1\text{-mm}^2$  x-y pixels at a pick-up coil to plate surface liftoff distance of 3 mm.

#### *Steps of Monte Carlo distribution sampling*

Monte Carlo simulation, utilizing the results from the BEM measurement model, was used to sample from the uncertainty distributions of scan resolution, plate thickness,



pick-up coil liftoff and pick-up coil tilt angle to generate an overall signal distribution.

The resulting signal distribution was then compared with the noise distributions associated with ac and dc measurements to determine POD. A 95% lower confidence bound was then generated by iterative generation of multiple signal distributions at each crack length. The Monte Carlo simulation steps are outlined here:

1. For each crack length, sample 1000 times from each of the four system parameter distributions to generate 1000 values of total error in  $B_{pp} \rightarrow (\Sigma \Delta B_{pp})$ . This, added to  $B_{pp}$ , constitutes the signal distribution to be compared to the noise distribution.

-Distributions used related to system parameter uncertainty

$\Delta B_{pp}$  (scan resolution):  $U(-0.016 B_{pp}, 0)$

$\Delta B_{pp}$  (plate thickness):  $N(0, 0.025 B_{pp})$

$\Delta B_{pp}$  (pick-up coil liftoff):  $N(0, 0.075 B_{pp})$

$\Delta B_{pp}$  (pick-up coil tilt angle): negative values from  $N(0, 0.0025 B_{pp})$ .

2. Within the same sampling loop as step 1, sample 1000 times from the noise distribution. In this way, each  $B_{pp}$  will have a corresponding noise value.

-Noise Distributions

dc:  $N(0, 58.48 \text{ pT})$

ac(lock-in):  $N(0, 0.475 \text{ pT})$

3. Compare each signal-noise pair (1000 pairs) to determine whether  $B_{pp} > (\text{noise} \times \text{SNR})$ . If yes, then increment “detected” counter. Otherwise, increment “missed” counter. A signal-to-noise ratio (SNR=2) was introduced at this point to represent a

detection criteria such that, when the signal-noise pair is compared, the signal value must be at least twice as large as the noise value to count as a “detection”. This is basically the “threshold” of the POD integration.

4. Then, for that particular crack length, the  $POD = (\# \text{ detected})/1000$ .
5. For determination of 95% lower confidence bound, run steps 1 through 4 100 times to generate a distribution of POD values. Sort the 100 values in ascending order (lowest POD to highest POD). The 95% lower confidence bound value is such that 95% of all POD values in this distribution are above this bound; this corresponds to the 5<sup>th</sup> POD value in the sorted sequence.
6. For each crack length, run steps 1 through 5. Forty crack length increments were used for these calculations. For the dc-noise calculation, this corresponded to a range of (0 - 4 mm). For the ac-noise calculation, the range was (0 - 0.05 mm).

Using the sampling numbers listed in steps 1 through 6 resulted in a total number of Monte Carlo simulations of  $(1000 / \text{parameter})(5 \text{ parameters})(100 \text{ POD loops})(40 \text{ crack length increments})(2 \text{ noise distributions}) = 40 \text{ million points}$ . This would not be easily accomplished experimentally; at one measurement per minute, it would take over 75 years!

#### *Monte Carlo generated POD curves*

Figure 4.23 shows the histogram representation of the signal and noise data generated (steps 1 and 2) for the 5-mm hole with a 1-mm crack in the dc-measurement case. The noise distribution was defined to be one-sided (a rectified normal distribution)

since the signal distribution has only positive values (peak-to-peak values are always positive). In this way, the noise distribution is represented in a peak-to-peak sense so that the distributions can be compared. In the noise histogram (lower), the signal histogram (upper) has been appropriately scaled and overlaid (dashed line) to show the region of overlap of the two distributions. It is this region which is of interest when determining POD.

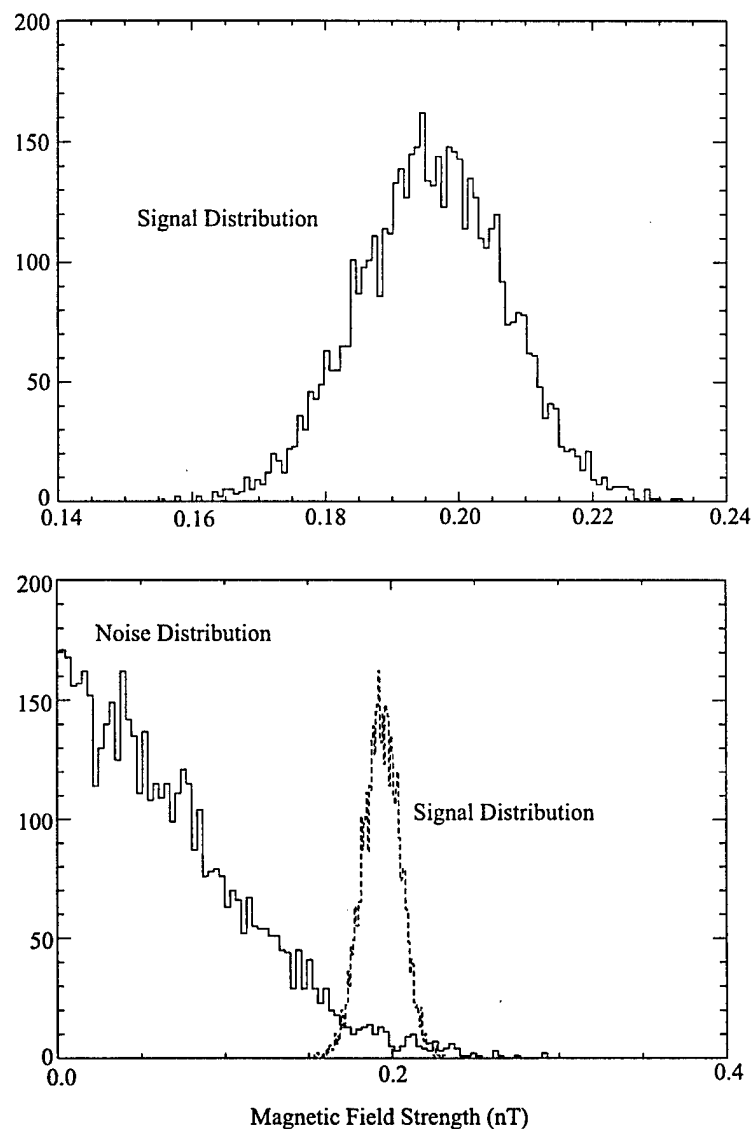


Figure 4.23 Monte Carlo generated signal and noise distributions for the dc case (1 mm crack)

Figure 4.24 is the dc-measurement POD curve resulting from generating similar distributions at each crack length. The abruptness of the POD curve near the origin is due to a combination of the relative sharpness of the signal distribution with respect to the noise distribution and the one-sidedness of the noise distribution. Also shown

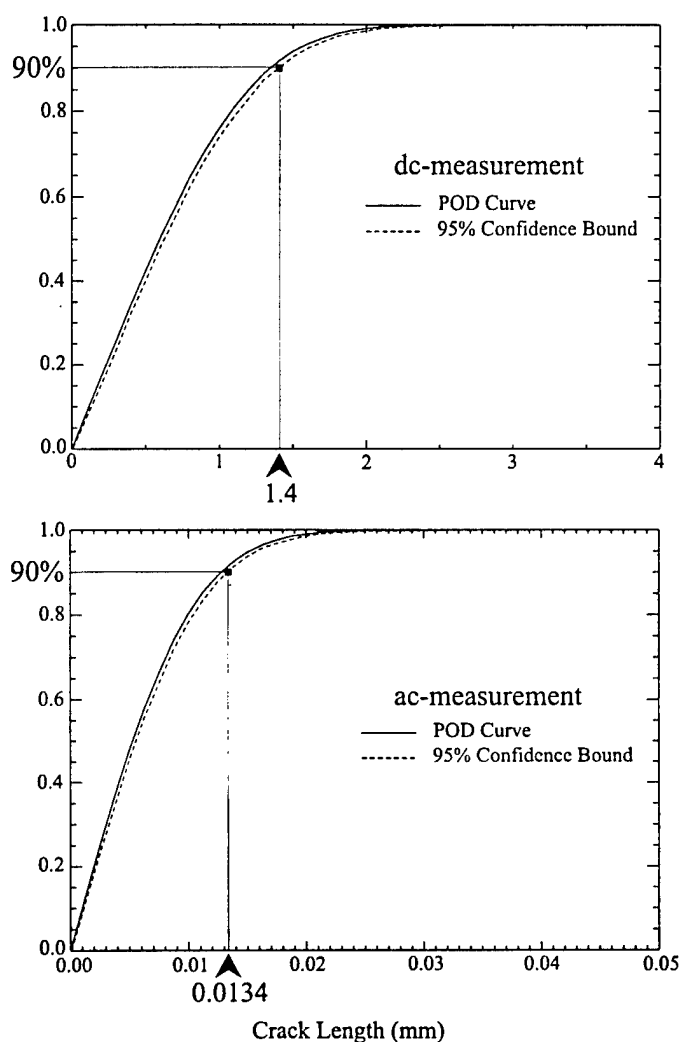


Figure 4.24 Ac/dc-measurement POD curves showing 90/95 crack lengths

in this figure is the 95% confidence bound that was determined from steps 5 and 6. This lower bound can also be calculated using a standard one-sided confidence limit formula [31]. For this case,

$$POD|_{95\%} = (\bar{x}_{POD} - 1.65 \frac{s_{POD}}{\sqrt{n = 100}}) \quad , \quad (4.22)$$

where  $\bar{x}_{POD}$  is the sample mean and  $s_{POD}$  is the sample standard deviation of the 100 Monte Carlo generated POD values. Lower confidence bounds using Eq. (4.22) were much narrower (lower confidence bound very close to POD curve) than those determined through direct sampling. It was decided to retain the Monte Carlo derived confidence bounds to be consistent with the approach and this would also give the “worst-case” lower confidence bound. However, Eq. (4.22) reveals how the confidence bound depends on the number of data points or, in the case of Monte Carlo, the number of simulations and therefore, will approach the POD curve itself for large numbers of simulations. The 95% lower confidence limit applies more to experimentally based POD curves that are usually generated from a relatively small number of data points. For simulated data, the lower confidence bound can be made to basically lie on the POD curve if enough runs are made and is not as useful as a concept as for the experimentally derived POD curve.

The minimum detectable crack lengths corresponding to 90% probability of detection at 95% confidence are 1.4 mm for the dc-measurement and 0.0134 mm for the ac-measurement. The very small minimum detectable crack length determined for the ac-measurement is due to the large noise reduction through use of the lock-in amplifier in this type of measurement.

## *POD and POFA*

In the Monte Carlo simulations, the signal distribution was compared directly with the noise distribution to determine POD. For direct sampling from distributions, the signal-to-noise ratio set the threshold ( $\hat{a}_{th}$  in standard calculations of POD (see Eq. (4.1)), which set the detection criteria. To examine the tradeoff between the probability of detection and the probability of false alarm when setting  $\hat{a}_{th}$ , the signal and noise distribution data generated by the Monte Carlo simulations can be presented in a different format. Refer back to Fig. 4.3 and Eqs. (4.1) and (4.8) regarding the description of POD and POFA. The SNR requirements determine where  $\hat{a}_{th}$  is to be placed, thus affecting POD (larger SNR requirements correspond to larger minimum detectable crack lengths).

Figure 4.25 displays the dc-measurement POFA and POD curves for three crack lengths, including the minimum detectable crack length, as a function of threshold. By setting a threshold, a value for POFA and POD for all crack lengths is determined. As can be seen, for a crack length of 0.5 mm, the 90% probability of detection point corresponds to a 28% POFA (*i.e.*, there is a 28% chance that noise will be mistaken for a signal). There is only a single POFA curve since probability of false alarm is determined from the noise distribution, which for these simulations is constant. Figure 4.26 shows the ac-measurement POFA and POD as a function of threshold for the previously determined minimum detectable crack length of 0.0134 mm. In both the dc and ac measurement cases, the POFA corresponding to the minimum detectable crack length is approximately zero. This is because the determination of these minimum values was a

result of a  $SNR=2$  requirement (equivalent to doubling the noise distribution in Figs. 4.25 and 4.26).

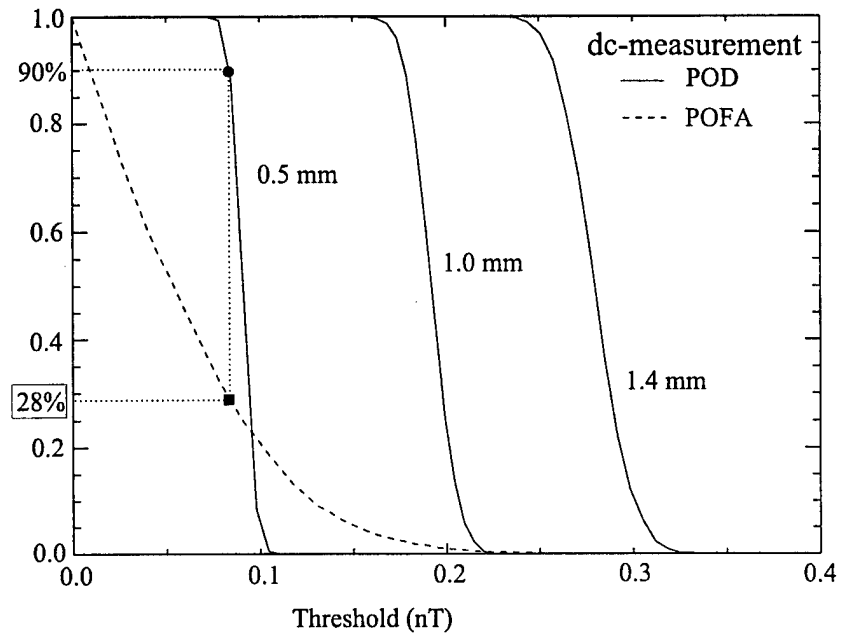


Figure 4.25 Dc-measurement POFA and POD as a function of threshold for three values of crack length

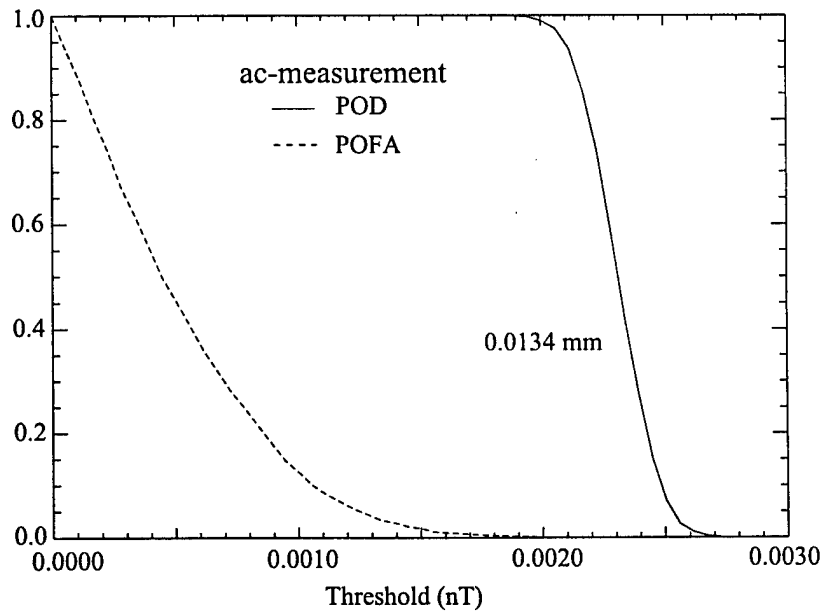


Figure 4.26 Ac-measurement POFA and POD as a function of threshold for the minimum detectable crack length

## CHAPTER V

### SUMMARY AND DISCUSSION

#### Summary

This research was directed towards the use of a Superconducting Quantum Interference Device (SQUID) magnetometer as a tool for nondestructive evaluation (NDE) to detect and characterize structural damage occurring in aging aircraft. The primary advantage of using SQUID's in NDE over other techniques is their ability to detect second layer damage commonly found in aircraft structures. A probability of detection (POD) analysis is being done to validate the capability of SQUIDs in this role. A POD analysis can be done using real experimental data or simulated experimental data generated from a measurement model. A goal in this research has been to develop the latter method, where simulation represents the experimental approach, is cheaper and faster, and identifies sources of unreliability in SQUID NDE.

The approach has been to develop a measurement model simulating the scanning of a SQUID over a dc-current injected sample containing a crack. The modeled crack and fastener hole simulates fatigue-cracking conditions found in aircraft fuselage lap joints. Boundary integral equations, using a special Green's function incorporating the crack, are used to solve the potential problem. This special formulation eliminates the need to model the crack as part of the boundary mesh. From the BIE potential solution, the magnetic field above the sample can be calculated through numerical integration of the Biot-Savart law. Special techniques, such as the use of quadratic interpolation



functions and a quarter-point formulation, were required to accommodate the singular behavior at the crack tip.

Thin copper plate samples containing a thin slot simulating a crack were used for experimental comparisons with the BEM measurement model. Several different SQUID systems, including a shielded axial-gradiometer SQUID (MicroSQUID), an unshielded axial-gradiometer SQUID (SBIR SQUID), and an unshielded planar-gradiometer SQUID (Mobile HTS SQUID), were used. Comparisons of scan centerline profiles from the experimental magnetic maps show good agreement (within a few percent in the region of the flaw) with the measurement model for all SQUID systems and test conditions used. Differences can be attributed to sample-related noise (*e.g.*, non-uniform current injection density).

Monte Carlo simulation utilizing the results of the BEM measurement model was used to generate POD curves. The uncertainty distributions resulting from a sensitivity analyses on several system parameters (scan resolution, plate thickness, pick-up coil liftoff, and pick-up coil tilt angle) were combined with experimental noise distributions to determine POD as a function of crack length. Threshold analysis resulted in comparative Probability of False Alarm (POFA) and POD curves. For dc-measurements, the minimum detectable crack length that could be found with 90% probability of detection with 95% confidence was 1.4 mm. The ac-measurements, which had much lower noise, had a corresponding value of 0.0134 mm. The POFA for these two cases was negligible due to the signal-to-noise ratio being set to two for the calculations. These small crack lengths suggest that additional experimental noise factors will have to be incorporated into the POD analysis before realistic SQUID NDE capability can be accurately quantified.

## Discussion

### Factors That May Decrease POD Capability

The relatively small values of minimum detectable crack length determined from this analysis prompts discussion on whether this reflects the true capability of SQUIDs in the detection of real cracks near fasteners in aircraft lap joints. Experimental measurements using SQUIDs on fatigue cracks in lap joints [36] have demonstrated the difficulty in finding cracks, adjacent to fasteners, on the order several millimeters in length. For the POD analysis done here, we have considered only four system parameters (scan resolution, plate thickness, pickup coil liftoff and tilt angle) and their associated uncertainties. Since it is these parameter uncertainties that determine the overall signal distribution, and therefore POD, it is apparent that significant parameters have been left out of this analysis. More than likely, these stem from sample-related noise associated with real measurements, which have not been represented in either the measurement model itself or through the parameter uncertainty distributions. Sample-related noise results from the geometry of the sample or, more specifically, how that geometry affects the current flow used to probe the sample. Figure 5.1 shows how some of these current paths can go under and/or through the crack and the fastener, further complicating the detection and characterization of the crack. Some of these issues are discussed in the following sections.

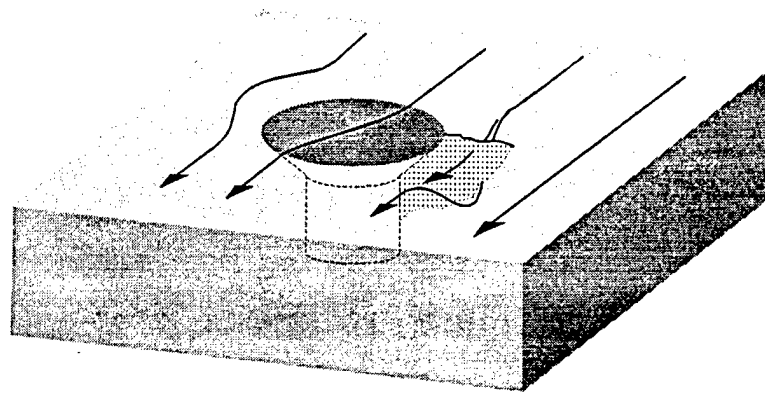


Figure 5.1 Additional current paths complicating crack detection

### *Crack shape*

Probability of detection is traditionally stated as a function of crack length to be consistent with damage tolerant requirements, which are stated in terms of crack length. However, crack shape is an important issue to discuss briefly since cracks of the same “length” but different shape could result in different signals. Currently, the BEM measurement model simulates a straight-through crack (the same length through the entire thickness of the plate) but it is possible to use the model to simulate “3-D” cracks to examine the effect of crack “shape” on magnetic field. By creating slices of varying shapes and depths (see Fig. 5.2), a pseudo-3D crack can be modeled. The total signal is then the superposition or sum of the signals calculated at each of these slices. However, as discussed in Chapter II, the model does not allow current flow perpendicular to the slices, only in the plane of each layer, and cannot model current going under cracks and fastener heads.

For this work, the “signal” used in the POD analysis has been defined as the

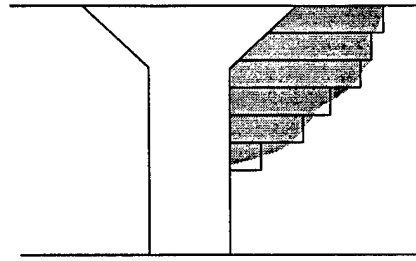


Figure 5.2 Pseudo 3-D modeling of a crack using slices

peak-to-peak value of the magnetic dipolar signal. The dipolar signal has characteristics that are related to physical characteristics of the crack. The amplitude of the dipole is proportional to crack size. More specifically, for dc-current injection, the signal is proportional to the cross sectional area of the crack. For the 2-D modeling used in the BEM measurement model, this is equivalently crack length. It is also known that the peak-to-peak separation is proportional to the liftoff and the spreading out of the dipole signal is related to the spatial distribution of the crack. Since crack shape affects both the amplitude and the shape of the magnetic field, then this pseudo 3-D approach would be a better approximation to a real crack that has shape that varies with depth.

#### *Ideal cracks versus real cracks and slots*

The BEM measurement model assumes an ideal, perfectly insulating, infinitely thin crack. This assumption will lead to differences between the model and measurements made on samples containing either wide cracks (slots) or real fatigue cracks. Most fabricated test samples used in our laboratory use slots, made by a saw or electrodischarge machining (EDM), to simulate cracks. A combination of a drilled hole with an EDM slot is an approximation to a crack emanating from an aircraft fastener

hole. This is useful in preliminary analyses, especially for development of NDE techniques. Fabrication of test samples made this way is simple and controllable, making it easy to build a test set representing the range of conditions that are of interest. But, measurements with NDE instruments [18, 19] have shown that the instrument response from a slot is not necessarily the same as that from a fatigue crack of the same size and geometry. Figure 5.3 schematically shows some of the possible variations, each possibly resulting in a different instrument response.

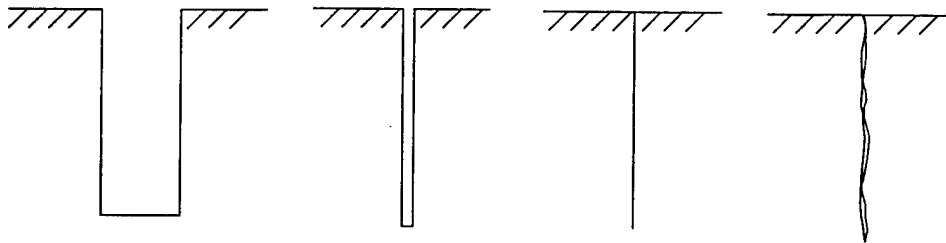


Figure 5.3 Slot profiles: (a) wide slot (b) narrow slot (c) ideal crack (d) real crack

More realistic crack specimen fabrication can be accomplished as described in [20]:

- a) Introduce a controlled starter notch (usually by EDM) into the specimen.
- b) Promote a fatigue crack from the notch by cyclically fatigue loading the specimen with axial and/or bending loads.
- c) Remove starter notch to retain only the sharp fatigue crack and to produce a desired specimen surface finish.

However, this is a time intensive process and it is difficult to control as to produce “standard” cracks of various lengths used in system characterization.

The BEM measurement model simulates a closed crack that is electrically insulated along the entire length. We have shown that it provides a reasonable approximation to a thin slot for liftoffs appropriate for SQUIDs commonly used in the laboratory ( $> 3$  mm). However, for real fatigue cracks, it is possible that crack closure may cause electrical conductivity across parts of the crack. Probability of detection will be strongly dependent on the effects of crack closure since, if current is flowing through the crack instead of around it, the signal (which is proportional to the perturbation of the current) will be greatly reduced. It is not yet understood how much crack closure effects current flow since it is likely that the oxide layers that form on the crack surfaces will act as an electrical insulator and so, only those contact points where the oxide layer is not present will provide conductive paths.

#### *Additional current paths*

The POD analysis has been based on simulated measurements of a crack emanating from a fastener *hole* and has completely ignored the effects of the fastener itself. This is most likely one of the larger sources of discrepancy present between the model and real measurement. Since most fatigue cracks start under the fastener head, early detection is difficult and usually the crack has to propagate beyond the fastener head before detection occurs. Another critical issue is that of contact between the fastener and the hole sides, which can create numerous current flow paths across and through the fastener. These currents may be too difficult to model directly and their associated uncertainty might have to be represented through a sample-related noise distribution. This will probably have to be determined experimentally by examining

samples with holes alone and with fasteners inserted to quantify the effect on the magnetic signal.

### *Geometry factors*

Current can also be greatly affected by the geometry of the surrounding structure, particularly edges such as lap joint seams. Figure 5.4 is a detail from Fig. 3.4 showing that edges can produce a large signal amplitude that can make flaw detection difficult, especially if the flaw is located near an edge.

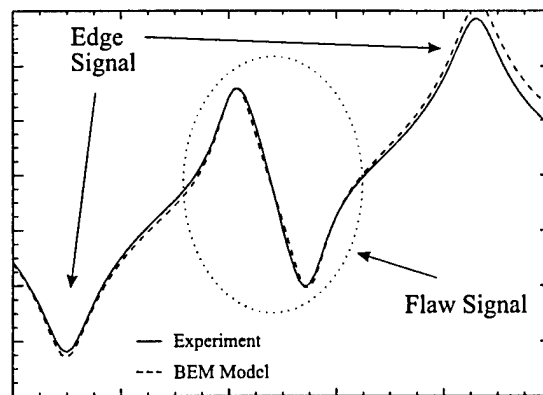


Figure 5.4 Detail from Fig. 3.4 pointing out edge and flaw signals

Other examples of edge signals can be seen in previously shown figures (Fig. 1.6 (b) and Fig. 3.2). Image processing techniques can partially remove the background slope due to these edges but it is still difficult to extract the signal from a flaw that is near an edge. Edges and other geometrical factors (*e.g.*, structural support members) affect the ability of the SQUID to detect a crack and these have not been taken into account in this POD analysis.

## Factors That May Increase POD Capability

The peak-to-peak value of the magnetic dipolar map is the present definition of “signal” used in these analyses. Peak-to-peak amplitude is a very limited use of the information available in the mapping since it reduces the entire 2-D image to a single value. It is the opinion of the author that image features (*e.g.*, shape and asymmetry) of the 2-D magnetic field map are just as important as the peak-to-peak signal amplitude in the detection and characterization of cracks, especially near fastener holes. For example, if we look at the magnetic map centerline profiles for various ideal geometries that have the same “cross sectional length” perpendicular to the current injection direction, we can see that using only peak-to-peak information for current perpendicular to the crack can lead to detection problems. The left-hand side of Fig. 5.5 shows the profiles for the current transverse to the crack at three different liftoffs for a 9 mm diameter hole, a 5 mm hole with a 4 mm crack, and a 9 mm crack. The signal values for each of the traces are plotted on the same scale and represent a SQUID system using 3 mm pickup/balance coils with a 3 cm baseline. From this information, all the profiles look the same in that they are dipolar with a mostly symmetrical shape. Based on peak-to-peak amplitude in a single direction, we can not distinguish between a crack alone, hole alone, or a hole-with-crack combination unless a baseline signal amplitude can be established as was done earlier in this POD analysis using the signal associated with a 5 mm hole alone. However, this approach would not work here since the 5 mm hole is not a constant feature in all three geometries.

The rotating current schemes of [30] take advantage of the differing two-dimensional structure of these three geometries. By rotating the current direction, the



signals associated with a crack will go through a maximum (when the current is perpendicular to the crack) and a minimum (when the current is parallel to the crack). A hole alone will not show this cyclic behavior (unless it is out-of-round). On the right-hand side of Fig. 5.5 are the corresponding profiles when the current is parallel to the crack showing the 9 mm crack having a flatline (zero signal) and the 5 mm hole with a 4 mm crack having a signal corresponding to a 5 mm hole alone and the 9 mm hole is unchanged. In this way, the three geometries could be distinguished by a measure of their peak-to-peak difference at the two current injection directions, with the crack alone being the largest, the hole-with-crack combination the next largest, and the hole alone having no difference. Real fatigue cracks will have some small signal for current injected parallel to the crack (versus zero signal for the ideal cracks of Fig. 5.5) but will still show the same maximum/minimum behavior as a function of current injection direction (the signal difference will just be smaller than the ideal crack case).

It may also be possible to distinguish between these three cases using a single current direction. By looking at the contour maps for the three cases, it can be seen that it may be possible to use dipole extrema eccentricity as an identification procedure. Figure 5.6 shows the contour maps for these cases with the bidirectional arrows in the upper figure representing the measures related to extrema eccentricity, defined here as

$$e = \frac{a_e}{b_e} . \quad (5.1)$$

The hole-with-crack contour plot has different eccentricities for the left and right extrema of the dipole. For the hole alone and the crack alone, there is left-right symmetry but the

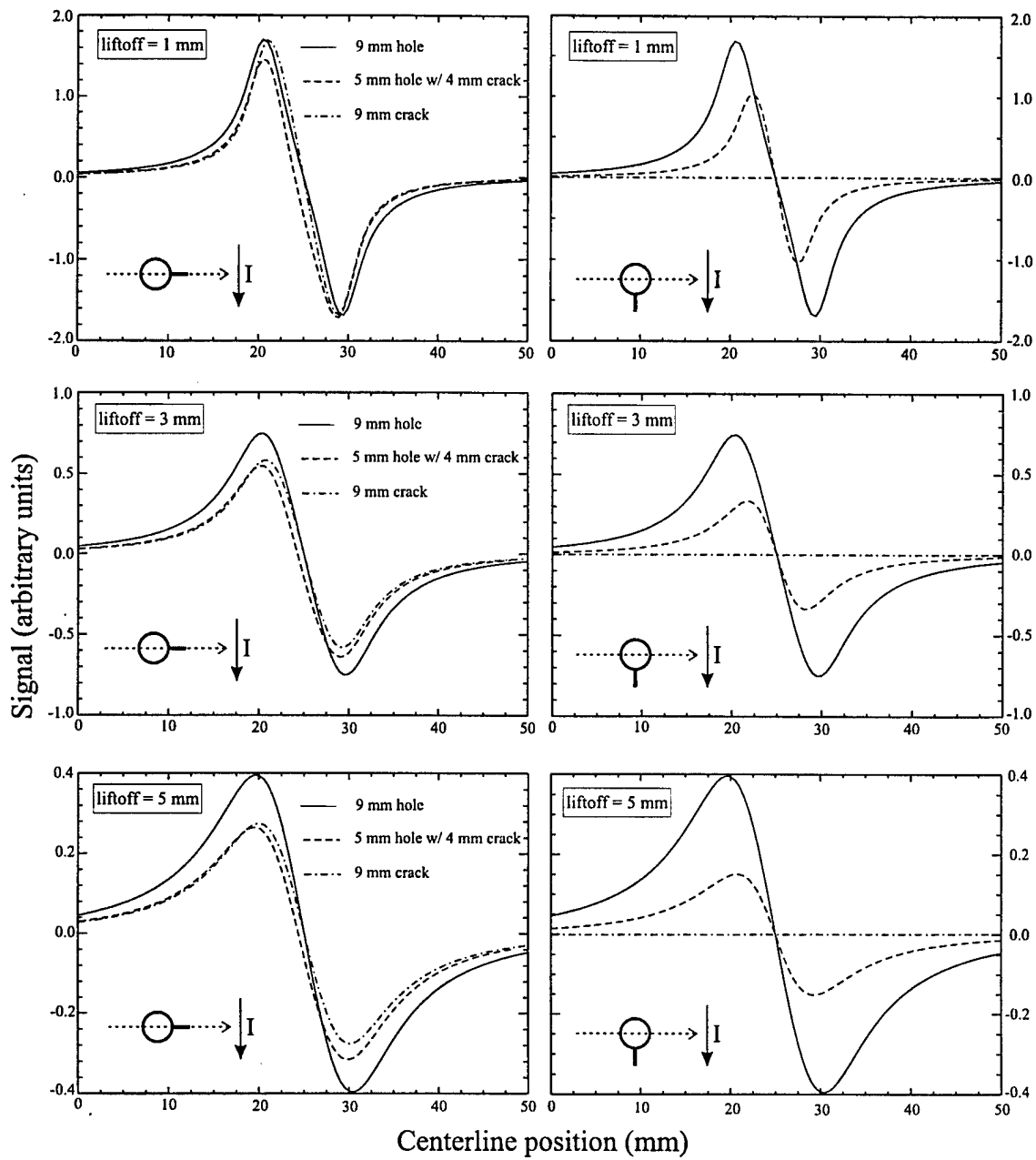


Figure 5.5 Profiles for three 9-mm "cross section" geometries at varying liftoffs  
(Note: all profile traces are on the same scale)

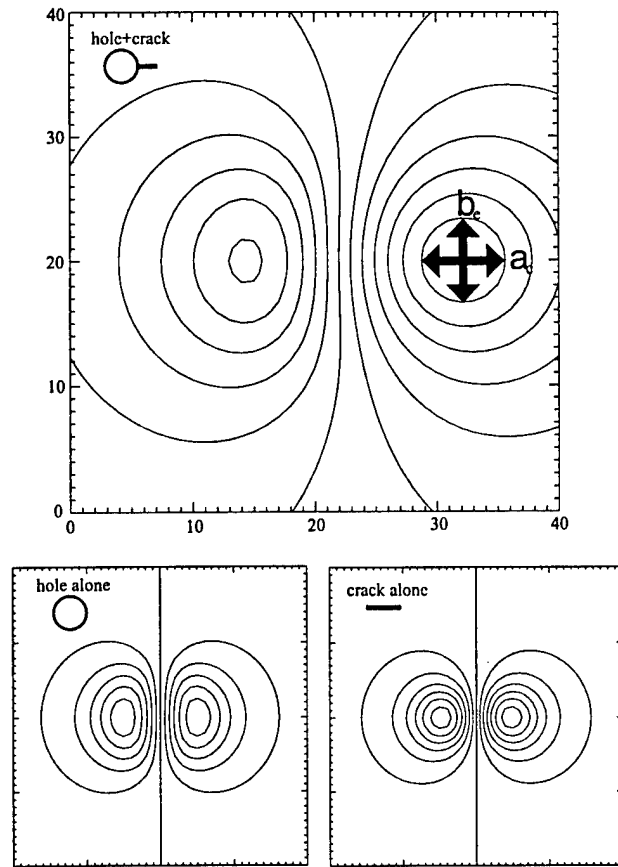


Figure 5.6 Contour plots showing extrema eccentricity

eccentricity is different between the two,  $e_{hole} < e_{crack}$ . This is due to the hole having more spatial (physical) extent than the crack in the  $b_e$  direction causing the signal to be more stretched out in comparison. Since this feature is strongly a function of liftoff, it is difficult to determine a quantitative measure without further analysis.

SQUID NDE systems will have to use asymmetry measures (which includes the rotating current direction technique) for crack detection, especially for cracks originating from fastener holes. If the asymmetry technique is used only to find the maximum and minimum of the signal, then POD may still be determined primarily from peak-to-peak amplitudes. However, if additional measures of asymmetry (*e.g.*, eccentricity or other

shape factors) are to be used, then POD analyses must incorporate these measures into the standard peak-to-peak analysis to reflect the true capability of the system. This is an important topic to be addressed for future development of SQUID POD methodologies.

#### Other Comments and Suggestions

The BEM measurement model has already been used in other experimental work involving validation [33, 34] and calibration techniques [35]. The model is just now beginning to be used for POD work, which was what it was originally designed for. The measurement model can provide a fast and accurate way to simulate scans over samples containing injected current, making it a very useful sensitivity analysis tool. However, if the model is to be used to calculate realistic probability of detection values for SQUID systems, more work has to be done to identify those sources of noise which are causing the large discrepancy between experimental measurements on real fatigue cracks and the detection capability determined by this analysis. Some of the possible sources of this noise have been discussed but no work has been done as of yet to quantify their effects.

Also, the effect of the crack tip, which was a significant model formulation issue, seems to be somewhat washed out at the liftoffs presently used ( $> 3$  mm). It may be that the usefulness of the BEM measurement model may not be fully realized until the liftoffs are reduced enough to see the large magnetic fields in proximity of the crack tip. At smaller liftoffs ( $< 1$  mm), using less accurate models (*e.g.*, superposition) will lead to very large errors. Significant improvements in reducing liftoff, requiring a very short distance between superconducting and room temperatures, are more likely to be achieved in high-

temperature SQUID systems. The measurement model and the POD approach are readily applicable to these types of systems as well.

Some additional items to consider for future development include:

- automate the entire process: currently, the determination of POD requires several individual computational steps and it should be possible to incorporate all of these into one overall program.
- refine the Monte Carlo simulation: optimize the process since, as more uncertainty factors are included in the sampling, computational time will increase tremendously. It may be possible to determine functional forms for the POD instead of using Monte Carlo methods but this will depend on the distributions associated with the added uncertainty factors. Also, we need to define how to compare POD curves generated from simulation to those generated from experimental measurements (*e.g.*, relevance of lower confidence bound).
- examine applicability to eddy-current inducer technique: since this is the proposed technique for NDE in the field, we need to determine how well the eddy currents produced by the inducer sheet can be modeled by the dc-current injection of this model.
- incorporate signal measures other than  $B_z$  peak-to-peak: most of the magnetic map information is not currently used (*e.g.*, dipole shape characteristics). Probability of detection may be enhanced by additional measures derived from this unused information. This also leads into the use of vector magnetometers to measure  $B_x$  and  $B_y$ , which has yet to be addressed in POD determination.

APPENDIX A:

GREEN'S FUNCTION FORMULATION  
OF LAPLACE'S EQUATION  
FOR ELECTROMAGNETIC  
CRACK DETECTION

# Green's Function Formulation of Laplace's Equation for Electromagnetic Crack Detection

T. A. Cruse, A. P. Ewing, and J. P. Wikswo<sup>1</sup>

## 1 Introduction

The following note summarizes the development of a special Green's function for crack problems in potential theory. The formulation is for a single, straight crack contained within or intersecting a regular boundary. The formulation of the special Green's function was first derived for the elastic fracture mechanics problem. The current formulation is a subset of the elasticity problem and is formulated as a Hilbert problem using complex variables. The formulation is validated using boundary element modeling of the Mode III, pure (antiplane) shear fracture mechanics problem.

The Green's function formulation is applied to modeling the magnetic field for the steady-state current flow through a two-dimensional plate with a plane crack. The BIE formulation is used to obtain the boundary integrals necessary to compute the normal component of the magnetic field for an arbitrary remote sensing location. The boundary integrals involve the tangential current flow on all boundaries including that for the crack. The explicit form for each of the two crack tip singularity terms is derived.

## 2 Singular Potential and Green's Second Identity

The field problem is that of Laplace's equation subject to mixed boundary conditions which may locally be Dirichlet or Neumann conditions. We will formulate a boundary integral equation (BIE) for this problem using a special fundamental solution that corresponds to a surface upon which the normal derivative of the solution is zero. All other surfaces will have user-specified values of the potential or its normal derivative.

The field equations are for the unknown potential  $\phi(p)$  where  $p(\mathbf{x})$  is the Cartesian field point. The BIE will be formulated from a Green's identity using the fundamental solution of Laplace's equation and is denoted  $\psi(p, q)$  where  $p, q$  are the field point and the singular point, respectively. When these points are taken to the boundary they will be denoted as upper-case points  $P, Q$ . Details supporting this note are given in [1].

The fundamental solution in two dimensions is given by real part of the complex logarithm function. Recall that a real part of a complex function is one-half of the function plus its complex conjugate. We can then write the logarithmic potential as the following real form.

$$\psi(p, q) = [\log(z - c) + \log(\bar{z} - \bar{c})]/2 = \mathcal{R} \log(z - c) \quad (1)$$

where  $c = x_p + iy_p$ ,  $z = x_q + iy_q$  and  $i = \sqrt{-1}$ . This fundamental solution satisfies the following singular, inhomogeneous form of Laplace's equation.

$$\nabla^2 \psi(p, q) = 2\pi \mathcal{D}(p, q) \quad (2)$$

In this equation,  $\mathcal{D}$  is the Dirac delta function, defined by the relations  $\int_R \mathcal{D}(p, q) dV(q) = 1(p)$  and  $\mathcal{D}(p, q) \equiv 0$  so long as  $p \neq q$ .

The integral equation formulation for potential theory derives from Green's second identity, written for the fundamental solution and the unknown potential function.

$$\int_R [\phi(q) \nabla^2 \psi(p, q) - \psi(p, q) \nabla^2 \phi(q)] dV(q) = \int_S \left( \phi(Q) \frac{\partial \psi(p, Q)}{\partial n(Q)} - \psi(p, Q) \frac{\partial \phi(Q)}{\partial n(Q)} \right) dS(Q) \quad (3)$$

<sup>1</sup>H. Fort Flowers Professor of Mechanical Engineering, Graduate Student, and A. B. Learned Professor of Physics, respectively

We now take  $\phi(q)$  to satisfy Laplace's equation  $\nabla^2 \phi = 0$  and replace the Laplacian of the fundamental solution by the Dirac function, as above. The result is an integral identity for the values of  $\phi(p)$  in terms of the totality of Dirichlet and Neumann data.

$$2\pi\phi(p) = \int_S \left( \phi(Q) \frac{\partial\psi(p, Q)}{\partial n(Q)} - \psi(p, Q) \frac{\partial\phi(Q)}{\partial n(Q)} \right) dS \quad (4)$$

### 3 Boundary Integral Equation (BIE)

The above identity cannot be used for a solution to the unknown potential without complete knowledge of the Dirichlet and Neumann boundary conditions. In general, one or the other of these two boundary conditions is specified on portions of the boundary. These mixed boundary conditions can be written as follows.

$$\phi(Q) = f(Q) \quad Q \in S_D \quad (5)$$

$$\left. \frac{\partial\phi}{\partial n} \right|_Q = g(Q) \quad Q \in S_N \quad (6)$$

The total boundary  $S$  is given by the union of the Dirichlet boundary  $S_D$  and the Neumann boundary  $S_N$ .

The Laplacian operator is elliptic. This property endows the potential  $\phi(p)$  with considerable smoothness. The boundary values of  $\phi(Q)$  will be taken to be continuous in what follows. While the derivatives of the potential are also continuous on the interior, the normal derivative can be discontinuous on the surface. That fact is not central, however, to the following developments.

Under these circumstances, the potential  $\phi(Q)$  and its normal derivatives are continuous at the boundary. We can now subtract the boundary value of the potential at an arbitrary boundary point  $P$  from the boundary integral, and add it back in as follows.

$$2\pi\phi(p) = \int_S [\phi(Q) - \phi(P)] \frac{\partial\psi(p, Q)}{\partial n(Q)} dS(Q) + \phi(P) \int_S \frac{\partial\psi(p, Q)}{\partial n(Q)} dS(Q) - \int_S \psi(p, Q) \frac{\partial\phi(Q)}{\partial n(Q)} dS(Q) \quad (7)$$

The free term multiplying the potential at  $P$  can be integrated in closed form for all interior points  $p$  and the result is independent of the actual surface shape, so long as the surface is closed.

$$\int_S \frac{\partial\psi(p, Q)}{\partial n(Q)} dS(Q) = 2\pi \quad (8)$$

We now obtain an equivalent Green's identity for which all integrals are continuous as  $p \rightarrow P$ .

$$2\pi[\phi(p) - \phi(P)] = \int_S [\phi(Q) - \phi(P)] \frac{\partial\psi(p, Q)}{\partial n(Q)} - \int_S \psi(p, Q) \frac{\partial\phi(Q)}{\partial n(Q)} dS(Q) \quad (9)$$

Green's identity can now be taken to the boundary, letting  $p \rightarrow P$ , in a smooth manner. The resulting boundary integral equation (BIE) for the potential theory formulation is given by the following relationship.

$$0 = \int_S [\phi(Q) - \phi(P)] \frac{\partial\psi(P, Q)}{\partial n(Q)} - \int_S \psi(P, Q) \frac{\partial\phi(Q)}{\partial n(Q)} dS(Q) \quad (10)$$

The BIE is a constraint equation that holds for all harmonic functions. The defined constraint is between the Dirichlet and Neumann boundary conditions for the problem. All well-posed problems can be reduced to a well-defined integral equation which can be solved for all unknown boundary conditions. Following the solution of the BIE, one can substitute the totality of the derived Dirichlet and Neumann boundary data into the Green's identity for the interior potential function. This constitutes the full solution of the boundary value potential theory problem.



## 4 Green's Function for Crack Problems

We now seek to derive the special fundamental solution for two dimensional crack problems. For the EM problems we will be using the potential function to represent the current potential for the steady-state problem. The derivative of the potential normal to the crack surface will be zero, for the assumption of a perfectly insulating crack surface. We seek a Green's function for the resulting Neumann potential problem of the insulating crack. That is, we seek a function whose derivative normal to the plane crack is zero at the crack surfaces. In the steady-state EM problem, the crack is taken to be an infinitely thin insulating surface. We define the surface to be  $\Gamma$ . Further, we will take  $\Gamma$  to be a single straight line parallel to the  $x$ -axis in the two dimensional problem. The source of the derivation we will use is [2], [3].

The new fundamental solution or Green's function is the combination of two functions. The first is the same logarithmic potential we started with; the second is a function which will cancel the values of the  $y$ -derivative of the logarithmic potential — at the crack surface. That is, the  $y$ -derivative of the sum of the two potentials is to be zero at the crack surface. We achieve this by finding the solution to the boundary value problem for the second potential problem that cancels the values of the  $y$ -derivative of the logarithmic potential, at the crack.

The problem whose solution we now seek is called a Hilbert problem [4, 5]. The formulation consists of finding the potential for an infinite region with a crack surface  $\Gamma$  on which we have specified boundary conditions. The boundary conditions for the Hilbert problem are to be the Neumann conditions involving the  $y$ -derivative of the log-potential at the crack. For superposition, the resulting derivative is the negative of the boundary values for the Hilbert problem and are taken to be  $\beta(t)$  for  $t \in \Gamma$ .

We now derive the complex potential  $h(z)$  whose boundary values on  $\Gamma$  are  $\beta(t)$ . The boundary values for our problem are taken to be the same on both the upper and lower side of the crack  $\Gamma$ .

$$\begin{aligned} h^+(t) &= \beta(t) \\ h^-(t) &= \beta(t) \end{aligned} \tag{11}$$

The following combinations of these boundary conditions hold for the Hilbert problem we have defined. The general solution allows the potential to be discontinuous at the surface  $\Gamma$ .

$$\begin{aligned} h^+(t) - h^-(t) &= 0 \\ h^+(t) + h^-(t) &= 2\beta(t) \end{aligned} \tag{12}$$

The solution for this Hilbert problem is given as follows [2].

$$h(z) = \frac{1}{\pi\sqrt{z^2 - a^2}} \int_{\Gamma} \frac{\beta(t)\sqrt{a^2 - t^2}dt}{t - z} + \frac{P(z)}{\sqrt{z^2 - a^2}} \tag{13}$$

In this equation, the integral is performed on the positive side of the crack, from the left hand end  $t = -a$  to the right hand end  $t = +a$ . The function of integration,  $P(z)$  is a positive power polynomial which can be determined by the behavior of  $h(z)$  at infinity. These conditions require that  $P(z) = 0$ . A discussion of the complex variable integration method for this integral is given in [5]. In what follows, we will compute only the real part of this integral.

We can now take the boundary values  $\beta(t)$  to be such that they cancel the boundary conditions of the  $y$ -derivatives of the logarithmic fundamental solution. This superposition of two functions gives us a new fundamental solution whose  $y$ -derivative is zero on the crack surfaces. Recalling the fundamental solution to be given by the following expression

$$\begin{aligned} \psi(z, c) &= \mathcal{R}[\log(z - c)] \\ &= \frac{1}{2} [\log(z - c) + \log(\bar{z} - \bar{c})] \end{aligned} \tag{14}$$

we can derive the  $y$ -derivative of the logarithmic potential at the crack, which is parallel to the  $x$ -axis. We will take the negative of the derivative as our boundary conditions for the Hilbert problem. The final solution we seek will have zero  $y$ -derivative at the crack by adding the Hilbert problem potential to the fundamental solution potential.

$$\left. \frac{\partial \psi(z, c)}{\partial y} \right|_{z=x} = \frac{1}{2} \left[ \frac{i}{x-c} - \frac{i}{x-\bar{c}} \right] = -\beta(x) \quad (15)$$

It is seen that the boundary condition is a real function on the crack surface  $\Gamma$ .

The Green's function is to be a real function with the boundary conditions satisfying the values  $\beta(x)$ ; we will take this real function to be given by  $G(p, q; a)$ . The Hilbert problem potential is then given by the following integral.

$$G(p, q; a) = -\frac{1}{2\pi} \mathcal{R} \left[ \frac{1}{\sqrt{z^2 - a^2}} \int_{\Gamma} \frac{\sqrt{a^2 - t^2}}{t - z} \left( \frac{i}{t - c} - \frac{i}{t - \bar{c}} \right) dt \right] \quad (16)$$

The above integrals for the Green's function terms exist in closed form, as can be seen in [5]. We need only the real part for each of the above terms, as in [3], given as follows

$$\begin{aligned} G(p, q; a) &= \mathcal{R}[h(z)] \\ &= -\frac{1}{2} \mathcal{R} \left[ \frac{i}{\sqrt{z^2 - a^2}} \left( \frac{I(z) - I(c)}{z - c} - \frac{I(z) - I(\bar{c})}{z - \bar{c}} \right) \right] \end{aligned} \quad (17)$$

where the integral  $I(z)$  is defined below

$$I(z) = \frac{1}{\pi} \int_{-a}^{+a} \frac{\sqrt{a^2 - t^2}}{t - z} dt = \left[ \sqrt{z^2 - a^2} - z \right] \quad (18)$$

for all  $z$  except along the crack where  $I(z)$  has the boundary values

$$\begin{aligned} I^+(t) &= \left[ i\sqrt{t^2 - a^2} - t \right] \\ I^-(t) &= \left[ -i\sqrt{t^2 - a^2} - t \right] \quad t \in \Gamma \end{aligned} \quad (19)$$

The complex potential  $h(z, c)$  has been used to find a Hilbert problem solution for the boundary data derived from the  $y$ -derivatives of the fundamental solution. These terms will be used for the evaluation of the BIE terms involving the  $y$ -derivative.

The BIE also requires that we have the fundamental solution potential, and not just its  $y$ -derivative. Therefore, we have to integrate the function  $h(z)$  with respect to  $z/i$  to have the function whose boundary conditions on the crack we have just used. The integration result is given as follows [6]

$$\mathcal{G}(p, q; a) = \mathcal{R} \left[ \frac{1}{i} \int h(z, c) dz \right] = -\frac{1}{2} \mathcal{R} [J(z, c; a) - J(z, \bar{c}; a)] \quad (20)$$

where  $J(z, c)$  is given by the following result

$$J(z, c; a) = \log \left[ 2 \frac{\sqrt{z^2 - a^2} \sqrt{c^2 - a^2} + cz - a^2}{(z + \sqrt{z^2 - a^2})(c + \sqrt{c^2 - a^2})} \right] \quad (21)$$

such that

$$\frac{\partial J}{\partial z} = \frac{I(z) - I(c)}{(z - c)\sqrt{z^2 - a^2}} \quad (22)$$

We now have the two Hilbert problem forms that are needed to modify the BIE for the crack problem. The new potential  $J(z, c; a)$  depends on both field points as well as the crack size. The crack for this formulation is limited to a straight crack along the real axis with its center at the origin. For computational purposes, we use a simple shift and rotation of the coordinate axes to put the crack at any user-defined location and orientation relative to the physical geometry.

## 5 BIE with the Special Green's Function

The final formulation for the crack problem is obtained by taking the sum of the original fundamental solution with the solution of the Hilbert problem. This modified fundamental solution which satisfies the insulated condition on the crack surface is denoted a Green's function for the crack. That is, the Green's function is an harmonic function containing the fundamental singularity property and it satisfies the boundary conditions on the crack. This fundamental solution is denoted by  $\Psi(p, q)$  and is given by the real part (denoted by the  $\mathcal{R}$  notation) of the two terms. The original fundamental solution term has been normalized by dividing it by  $2\pi$ .

$$\begin{aligned}\Psi(p, q; a) &= \frac{1}{2\pi} \left[ \mathcal{R} \log(z - c) - \frac{1}{2} \mathcal{R} \{J(z, c; a) - J(z, \bar{c}; a)\} \right] \\ &= \frac{1}{4\pi} \mathcal{R} [\log(z - c) + \log(\bar{z} - \bar{c}) - J(z, c; a) + J(z, \bar{c}; a)]\end{aligned}\quad (23)$$

The modified fundamental solution, or Green's function, for the crack is shown containing the crack length as a parameter. This is to reinforce that the presence of the crack is now embedded in the fundamental solution terms. The Green's function derivative in the normal direction at the surface point  $Q$  will also be needed for the BIE formulation. That result is now given.

$$\begin{aligned}\frac{\partial \Psi(p, Q; a)}{\partial n} &= \frac{1}{4\pi} \mathcal{R} \left[ \frac{n_x + in_y}{z - c} + \frac{n_x - in_y}{\bar{z} - \bar{c}} - \frac{(n_x + in_y)}{\sqrt{z^2 - a^2}} \left( \frac{I(z) - I(c)}{z - c} - \frac{I(z) - I(\bar{c})}{z - \bar{c}} \right) \right] \\ &= \frac{1}{2\pi} \mathcal{R} \left[ \frac{n_x + in_y}{z - c} \right] - \frac{1}{4\pi} \mathcal{R} \left[ \frac{(n_x + in_y)}{\sqrt{z^2 - a^2}} \left( \frac{I(z) - I(c)}{z - c} - \frac{I(z) - I(\bar{c})}{z - \bar{c}} \right) \right]\end{aligned}\quad (24)$$

The BIE identity can now be written on the total of the regular surface and the crack surface.

$$\begin{aligned}0 &= \int_S [\phi(Q) - \phi(P)] \frac{\partial \Psi(P, Q; a)}{\partial n(Q)} - \int_S \Psi(P, Q; a) \frac{\partial \phi(Q)}{\partial n(Q)} dS(Q) + \\ &\quad \int_\Gamma [\phi(Q) - \phi(P)] \frac{\partial \Psi(P, Q; a)}{\partial n(Q)} - \int_\Gamma \Psi(P, Q; a) \frac{\partial \phi(Q)}{\partial n(Q)} dS(Q)\end{aligned}\quad (25)$$

The effect of the special Green's function formulation is now seen. Both integrals on the crack surface  $\Gamma$  are zero. The first is zero due to the Green's function having zero normal derivative on the crack, and the second due to the insulating boundary conditions for the unknown potential function.

Thus, we take as the final BIE for the insulated crack potential theory problem to be the following equation.

$$0 = \int_S [\phi(Q) - \phi(P)] \frac{\partial \Psi(P, Q; a)}{\partial n(Q)} - \int_S \Psi(P, Q; a) \frac{\partial \phi(Q)}{\partial n(Q)} dS(Q)\quad (26)$$

The BIE models the crack through the Green's function, and not through the boundary of the crack. The form that has been derived places the crack at the origin and oriented along the  $x$ -axis. However, the existing computer program allows the user to specify the global location of the crack and its orientation. The crack can be contained within the region or can intersect one or more physical surfaces. Again, the BIE code has been written to accept these cases.

Thus, the BIE for the insulated crack problem contains only the uncracked surface in the BIE. Application of the special Green's function to the elasticity problem has demonstrated the very high accuracy of this formulation for crack problems, as in [6]. Further, applications of the special Green's function formulation have demonstrated a high degree of accuracy for cracks at holes and other stress concentrating geometries [7].

## 6 Interior Derivatives of the Potential

The interior potential for the Green's function formulation is given by the identity

$$\phi(p) = \int_S \phi(Q) \frac{\partial \Psi(p, Q; a)}{\partial n(Q)} - \int_S \Psi(p, Q; a) \frac{\partial \phi}{\partial n} \Big|_Q dS(Q) \quad (27)$$

The derivatives in the  $x$ -direction and the  $y$ -direction of the interior potential are needed for the full electromagnetic field formulation.

$$\frac{\partial \phi(p)}{\partial(x_c, y_c)} = \int_S \phi(Q) \frac{\partial^2 \Psi(p, Q; a)}{\partial n(Q) \partial(x_c, y_c)} - \int_S \frac{\partial \Psi(p, Q; a)}{\partial(x_c, y_c)} \frac{\partial \phi}{\partial n} \Big|_Q dS(Q) \quad (28)$$

The derivative at the point  $c$  of the kernels given in Eq. 23 and Eq. 24 are required in order to compute the gradient of the interior potential. These kernel derivatives are given as follows.

$$\begin{aligned} \frac{\partial \Psi(p, Q; a)}{\partial(x_c, y_c)} &= -\frac{1}{2\pi} \mathcal{R} \left[ \frac{(1, i)}{z - c} \right] \\ &\quad - \frac{1}{4\pi} \mathcal{R} \left[ \frac{(1, i)}{\sqrt{c^2 - a^2}} \left( \frac{I(z) - I(c)}{z - c} \right) - \frac{(1, -i)}{\sqrt{\bar{c}^2 - a^2}} \left( \frac{I(z) - I(\bar{c})}{z - \bar{c}} \right) \right] \end{aligned} \quad (29)$$

The identity

$$\frac{\partial J}{\partial c} = \frac{I(c) - I(z)}{(c - z)\sqrt{c^2 - a^2}} = \frac{I(z) - I(c)}{(z - c)\sqrt{c^2 - a^2}} \quad (30)$$

has been applied using the symmetry of  $J(z, c; a)$  with respect to  $z, c$ .

The derivative at  $c$  of the normal derivative kernel function in Eq. 24 is given in the following set of terms.

$$\begin{aligned} \frac{\partial^2 \Psi(p, Q; a)}{\partial n \partial(x_c, y_c)} &= +\frac{1}{2\pi} \mathcal{R} \left[ \frac{(n_x + in_y)(1, i)}{(z - c)^2} \right] \\ &\quad - \frac{1}{4\pi} \mathcal{R} \left[ \frac{(n_x + in_y)(1, i)}{\sqrt{z^2 - a^2}} \left( \frac{\partial}{\partial c} \frac{I(z) - I(c)}{z - c} \right) \right] \\ &\quad + \frac{1}{4\pi} \mathcal{R} \left[ \frac{(n_x + in_y)(1, -i)}{\sqrt{z^2 - a^2}} \left( \frac{\partial}{\partial \bar{c}} \frac{I(z) - I(\bar{c})}{z - \bar{c}} \right) \right] \end{aligned} \quad (31)$$

The remaining derivatives with respect to  $z$  above are given in the following result.

$$\frac{\partial}{\partial c} \frac{I(z) - I(c)}{z - c} = \frac{I(c)}{(z - c)\sqrt{c^2 - a^2}} + \frac{I(z)}{(z - c)^2} \quad (32)$$

## 7 Crack Tip Field Intensity Factor

One of the key parameters in crack problems is the so-called crack tip intensity factor ( $\text{CIF} = K$ ) derived from the derivatives of the potential at each crack tip. The CIF is given by the following limit

$$K_{(x,y)} = \lim_{c \rightarrow \pm a} \sqrt{2\pi(c \mp a)} \frac{\partial \phi(z, c; a)}{\partial(x, y)} \quad (33)$$

for  $z \neq c$ . The intensity factor can be derived for any direction of approach to either of the crack tips. For convenience, we will take the point  $c = \pm(a + r)$  where the real variable  $r$  is the distance from the crack tips and is taken to be along the  $x$ -axis. Thus,  $\bar{c} = c$  for the limiting processes. The CIF is then given by the following integral identity from Eq. 4.

$$K_{(x,y)}|_{\pm a} = \lim_{r \rightarrow 0} \sqrt{2\pi r} \frac{\partial \phi(p)}{\partial(x, y)} = \lim_{r \rightarrow 0} \sqrt{2\pi r} \int_S \left( \phi(Q) \frac{\partial^2 \Psi(p, Q)}{\partial(x, y) \partial n(Q)} - \frac{\partial \Psi(p, Q)}{\partial(x, y)} \frac{\partial \phi(Q)}{\partial n(Q)} \right) dS \quad (34)$$

Carrying out the limits on the two kernel functions, one finds that the derivative  $\partial\phi/\partial x$  is zero ahead of the crack. That is, the gradient of the flux parallel to the crack is zero for potential theory. The singular term is contained solely in  $\partial\phi/\partial y$ , the gradient transverse to the crack, ahead of the crack. One can also find from a study of the kernels that the gradients for points on the crack surfaces are swapped and the sign changed. Thus, for the top crack surface  $\partial\phi/\partial x$  is singular with the CIF equal to minus that of the approach ahead of the crack, output in the code as  $K$ . The derivative  $\partial\phi/\partial y$  is, by the Green's function, zero along the crack surfaces.

The two kernels that are needed in order to compute  $K$  for the limit using points ahead of the crack are given as follows, using the right hand crack tip  $c = +a$ . The code allows the negative crack tip computation as well.

$$\lim_{r \rightarrow 0} \sqrt{2\pi r} \frac{\partial^2 \Psi(p, Q)}{\partial y \partial n(Q)} = \sqrt{\frac{a}{4\pi}} \mathcal{R} \left[ \frac{i(n_x + in_y)}{(z - a)\sqrt{z^2 - a^2}} \right] \quad (35)$$

$$\lim_{r \rightarrow 0} \sqrt{2\pi r} \frac{\partial \Psi(p, Q)}{\partial y} = -\frac{1}{\sqrt{4\pi a}} \mathcal{R} \left[ \frac{i[I(z) - I(a)]}{z - a} \right] \quad (36)$$

## 8 Boundary Element Algorithm

### 8.1 Quadratic Straight Line Segments

The boundary element method (BEM) replaces the actual boundary with an approximate boundary discretized as a finite set of simple elements. The current algorithm uses straight line segments in order that we can implement analytical integrations of the kernels in Eq. 23 and Eq. 24. The boundary functions are then represented by quadratic interpolations over each boundary segment. Continuity of the potential is enforced, but not continuity of the flux, between the boundary elements. The analytical integrations of the two kernels times quadratic polynomial interpolations of the boundary data are computed on an element-by-element basis.

The quadratic boundary data model replaces each of the boundary functions with the following general form of interpolative.

$$F(z) = A_0 + A_1 z + A_2 z^2 \quad (37)$$

The current BEM algorithm is based on boundary elements defined by end nodes and mid-length nodes for each boundary element,  $\Delta S_i = \Delta z/B$ . The general form in Eq. 37 can be replaced by a form specifically tailored to the element-by-element integration for the BEM algorithm. We define the endpoint nodal values of each interpolative by  $F_1$ ,  $F_2$  and the midside nodal value by  $F_3$ . The general quadratic interpolative is then given by

$$\begin{aligned} F(z) = & \frac{F_1 - F_2}{\Delta z} z_Q - \frac{F_1 - F_2}{\Delta z} z + 2 \frac{F_1 + F_2}{(\Delta z)^2} z_Q^2 - \\ & - 4 \frac{F_1 + F_2}{(\Delta z)^2} z_Q z + 2 \frac{F_1 + F_2}{(\Delta z)^2} z^2 + F_3 \left[ 1 - 4 \frac{z_Q^2}{(\Delta z)^2} + 8 \frac{z_Q z}{(\Delta z)^2} - 4 \frac{z^2}{(\Delta z)^2} \right] \end{aligned} \quad (38)$$

The midside node for each segment is denoted as  $z_Q$ .

### 8.2 Integration of the Boundary Terms

The integrals for each boundary element, with the complex variables used herein, are converted to complex integrals with respect to  $dz = BdS$  where  $B = in_x - n_y$ . It can be noted that  $A = n_x + in_y = -iB$  in Eq. 24. The boundary integrals are given symbolically in the following forms.

$$I(c) = \int_S F(z) \left( \Psi(z, c, a), \frac{d\Psi}{dn} \right) \frac{dz}{B} \quad (39)$$

Substitution of the quadratic interpolative from Eq. 38 into the above integral results in the following forms of boundary element terms for the end-point nodes ( $N = 1, 2$ ) and the midside node ( $N = 3$ ).

$$\begin{aligned} I(c) &= \Delta I_0 - (-1)^N (\Delta I_1 - \Delta I_2) - \Delta I_3 + \Delta I_4 \text{ for } N \neq 3 \\ &= \Delta I_5 + \Delta I_6 + \Delta I_7 \text{ for } N = 3 \end{aligned} \quad (40)$$

The terms  $I_0$  and  $I_1$  result from integration of the kernel functions times the constant interpolation terms in Eq. 38. The terms  $I_2$  and  $I_3$  are for the linear terms in the interpolation, and the term  $I_4$  is for the quadratic interpolation of the kernels. The terms  $I_1$  and  $I_2$  change sign for the two end nodes in Eq. 38. In the case of the integrals relative to the midside node, the term  $I_5$  is for the constant term in the interpolative, the term  $I_6$  is for the linear term, and  $I_7$  is for the quadratic term.

The kernel functions for the integrations are repeated in a convenient form below.

$$\begin{aligned} \Psi(p, q; a) &= \frac{1}{4\pi} \mathcal{R} [2 \log(z - c) - J(z, c; a) + J(z, \bar{c}; a)] \\ \frac{\partial \Psi(p, q; a)}{\partial n} &= \frac{1}{4\pi} \mathcal{R} \left[ 2 \frac{n_x + in_y}{z - c} - (n_x + in_y) \frac{\partial J(z, c)}{\partial z} + (n_x + in_y) \frac{\partial J(z, \bar{c})}{\partial z} \right] \end{aligned} \quad (41)$$

Substituting the identity  $dz = BdS$  in the above equation, and integrating over the segment  $\Delta S_i$ , we have the following integrals to evaluate. Since we are using straight line segments in the BEM algorithm, the term  $B$  is a constant over each segment.

$$\begin{aligned} \int_{\Delta S_i} (1, z, z^2) \Psi(p, q; a) (p, q; a) dS &= \frac{1}{4\pi B} \int_{\Delta z} (1, z, z^2) [2 \log(z - c) - J(z, c; a) + J(z, \bar{c}; a)] dz \\ \int_{\Delta S_i} (1, z, z^2) \frac{\partial \Psi(p, q; a)}{\partial n} dS &= \frac{1}{4\pi} \int_{\Delta z} (-i)(1, z, z^2) \left[ \frac{2}{z - c} - \frac{\partial J(z, c)}{\partial z} + \frac{\partial J(z, \bar{c})}{\partial z} \right] dz \end{aligned} \quad (42)$$

The final results are obtained by taking only the real part of the above integrals.

We will first consider the integrals of the potentials of the uncracked body. The integrated kernel functions are labeled  $\Delta U_0$ ,  $\Delta T_0$ ,  $\Delta U_1$ , etc., referring to the constant, linear, and quadratic interpolatives. The following summarizes those integration results.

$$\begin{aligned} 2\pi \Delta U_0 &= \frac{1}{B} [z(\log z - 1)]_1^2 \\ 2\pi \Delta T_0 &= -i \log z \Big|_1^2 \\ 2\pi \Delta U_1 &= \frac{1}{2B} \left[ z^2 \left( \log z - \frac{1}{2} \right) \right]_1^2 \\ 2\pi \Delta T_1 &= -i(z_2 - z_1) \\ 2\pi \Delta U_2 &= \frac{1}{3B} \left[ z^3 \log z - \frac{z^3}{3} \right]_1^2 \\ 2\pi \Delta T_2 &= -i \frac{z^2}{2} \Big|_1^2 \end{aligned} \quad (43)$$

The following terms are the integrals of the special Green's function terms. The integrations will be given in terms of the source point  $c$  as the conjugate results are obtained by simple substitution of  $\bar{c}$  for  $c$ .

$$\begin{aligned} 4\pi B \Delta U_0 &= -[(z - c)J(z, c; a) - z + \sqrt{z^2 - a^2} + I(c) \log(z + \sqrt{z^2 - a^2})]_1^2 + [\dots(z, \bar{c})] \\ 4\pi \Delta T_0 &= i[J(z, c; a) - J(z, \bar{c}; a)] \end{aligned}$$

$$\begin{aligned}
4\pi B \Delta U_1 &= - \left[ \frac{(z-c)^2}{2} J(z, c; a) + cU_0 - \frac{c}{2}(-z + \sqrt{z^2 - a^2} + I(c) \log(z + \sqrt{z^2 - a^2})) - \right. \\
&\quad \left. - \frac{1}{4}z^2 + \frac{1}{2}\sqrt{c^2 - a^2}z^2 - a^2 - \frac{1}{2}c\sqrt{z^2 - a^2} + \frac{z}{4}\sqrt{z^2 - a^2} + \right. \\
&\quad \left. + \frac{a^2}{4} \log(z + \sqrt{z^2 - a^2}) - \frac{c^2}{4} \right]_1^2 + [\dots(z, \bar{c})] \\
4\pi \Delta T_1 &= i[cJ(z, c; a) + z - \sqrt{z^2 - a^2} - I(c) \log(z + \sqrt{z^2 - a^2})]_1^2 - i[\dots(z, \bar{c})] \\
4\pi B \Delta U_2 &= - \left[ \frac{z^3}{3} J(z, c) \right]_1^2 + \int_1^2 \frac{z^3}{3} \left( \frac{I(z) - I(c)}{\sqrt{z^2 - a^2}(z - c)} \right) + [\dots(z, \bar{c})] \\
4\pi \Delta T_2 &= i[z^2 J(z, c; a)]_1^2 - 2\Delta U_1(z, c) - i[z^2 J(z, \bar{c}; a)]_1^2 - 2\Delta U_1(z, \bar{c}) \quad (44)
\end{aligned}$$

Again, we recall that the BEM equations are obtained by taking only the real part of the above integration results. A linear system of equations is generated by the BEM algorithm. The system of equations is automatically swapped during assembly such that the unknown boundary conditions appear in a single vector. The system of equations is square so long as there is only one unknown flux value at each boundary node.

### 8.3 Integration of the Interior Gradient Terms

The previous integrations are used to compute the boundary integrals for the BIE as well as for the evaluation of the interior potential function. Now we consider the evaluation of the derivatives of the interior potential function. We will take the gradient of the potential at an arbitrary interior point. The integrations of the kernels in Eq. 29 and 31 will again be broken up into the terms for the uncracked potential and the terms for the special Green's function. The integration results for the interpolated boundary functions times the kernels will again be denoted by  $U_0, T_0, U_1$ , etc.

The uncracked potential function integrals are given as follows.

$$\Delta U_{(0,1,2)} = \int_{\Delta S_i} (1, z, z) \frac{\partial \Psi(p, Q; a)}{\partial (x_c, y_c)} \frac{dz}{B} \quad (45)$$

$$\begin{aligned}
2\pi U_0 &= -\frac{(1, i)}{B} \log |z|_1^2 \\
2\pi U_1 &= -\frac{(1, i)}{B} z|_1^2 \\
2\pi U_2 &= -\frac{(1, i)}{2B} z^2|_1^2 \quad (46)
\end{aligned}$$

The above three results use the fact that the uncracked potential can be integrated from each source point as  $c = 0$  without loss of generality.

$$\begin{aligned}
2\pi T_0 &= \frac{i(1, i)}{z} \Big|_1^2 \\
2\pi T_1 &= -i(1, i) \log |z|_1^2 \\
2\pi T_2 &= -i(1, i) z|_1^2 \quad (47)
\end{aligned}$$

The following results are the integrals of the special Green's function terms, using the same notation as above for the terms in  $c$ ; the conjugate functions which must be combined with the terms below are of the same form with  $\bar{c}$  substituted for  $c$ . The coefficient  $(1, i)$  is also conjugated

to  $(1, -i)$ .

$$\begin{aligned}
4\pi BU_0 &= -(1, i) \left[ (z - c) \frac{\partial J(z, c)}{\partial c} - J(z, c) + \frac{\partial I(c)}{\partial c} \log(z + \sqrt{z^2 - a^2}) \right] \Big|_1^2 + \\
&\quad + (1, -i) [\dots (z, \bar{c})] \\
4\pi BU_1 &= -(1, i) \left[ \frac{1}{2} (z - c)^2 \frac{\partial J(z, c)}{\partial c} - z + \sqrt{z^2 - a^2} + I(c) \log(z + \sqrt{z^2 - a^2}) \right. \\
&\quad \left. - cJ(z, c) + c(z - c) \frac{\partial J(z, c)}{\partial c} - \frac{1}{2} \left[ -z + \sqrt{z^2 - a^2} + I(c) \log(z + \sqrt{z^2 - a^2}) \right] \right. \\
&\quad \left. - \frac{c}{2} \frac{\partial I(c)}{\partial c} \log(z + \sqrt{z^2 - a^2}) + \frac{1}{2} \frac{c}{\sqrt{c^2 - a^2}} \sqrt{z^2 - a^2} - \frac{1}{2} \sqrt{z^2 - a^2} \right] \Big|_1^2 + (1, -i) [\dots (z, \bar{c})] \\
4\pi BU_2 &= \dots
\end{aligned} \tag{48}$$

where

$$\mathcal{I}_1 = [(z - c)J(z, c) - z + \sqrt{z^2 - a^2} + I(c) \log(z + \sqrt{z^2 - a^2})] \tag{49}$$

$$\begin{aligned}
4\pi T_0 &= -i(1, i) \frac{\partial J(z, c)}{\partial c} \Big|_1^2 = \\
&= \frac{-i(1, i)}{\sqrt{c^2 - a^2} \sqrt{z^2 - a^2} + cz - a^2} \left( \frac{c\sqrt{z^2 - a^2}}{\sqrt{c^2 - a^2}} + z \right) \Big|_1^2 + i(1, -i) [\dots (z, \bar{c})] \\
4\pi T_1 &= -i(1, i) \left[ J(z, c) + c \frac{\partial J(z, c)}{\partial c} - \frac{\partial I(c)}{\partial c} \log(z + \sqrt{z^2 - a^2}) \right] \Big|_1^2 + i(1, -i) [\dots (z, \bar{c})] \\
4\pi T_2 &= \dots
\end{aligned} \tag{50}$$

#### 8.4 Test Problem for Antiplane Shear Loaded Crack

The test problem is the antiplane shear fracture mechanics problem. The antiplane shear problem is governed by Laplace's equation  $\nabla^2 w(x, y)$  for the equilibrium equation in terms of the displacement function  $w(x, y)$ . The two shear stresses (denoted by  $\tau_{xz}$  and  $\tau_{yz}$  where  $z$  is normal to the plane) correspond to the gradients of the potential in the  $x, y$  directions. Thus, the formulated Green's function corresponds to the exact solution for a large plate containing a central crack remotely loaded by the applied shear traction  $\partial\phi/\partial n$ . Equilibrium of the boundary tractions is given by the side-condition

$$\oint_S \frac{\partial w(x, y)}{\partial n} dS \equiv 0 \tag{51}$$

which must be satisfied for the solution to the BIE to exist.

The test problem is a square plate containing a central crack of length  $2a$ . The shear modulus  $\mu$  is taken to be unity. The selected BEM model for this problem is given in Figure 1. The mesh consists of twenty-four boundary elements, as shown. The crack is taken to have an angle  $\beta$  relative to the global  $x$ -axis. The test problem is loaded by shear values of +5 units on the top surface, -5 units on the bottom surface, and zero on the side surfaces.

The validation solutions will be the shear stress intensity factor, referred to as the Mode III stress intensity factor in fracture analysis. The intensity factor for the infinite plate loaded by a constant  $\tau_{yz} = \tau_0$  at infinity is given by the following result [9].

$$K_{III} = \tau_0 \sqrt{\pi a} \tag{52}$$

In the case of the angled crack the solution is found in [10] to be given as follows.

$$K_{III} = \tau_0 \cos \beta \sqrt{\pi a} \tag{53}$$



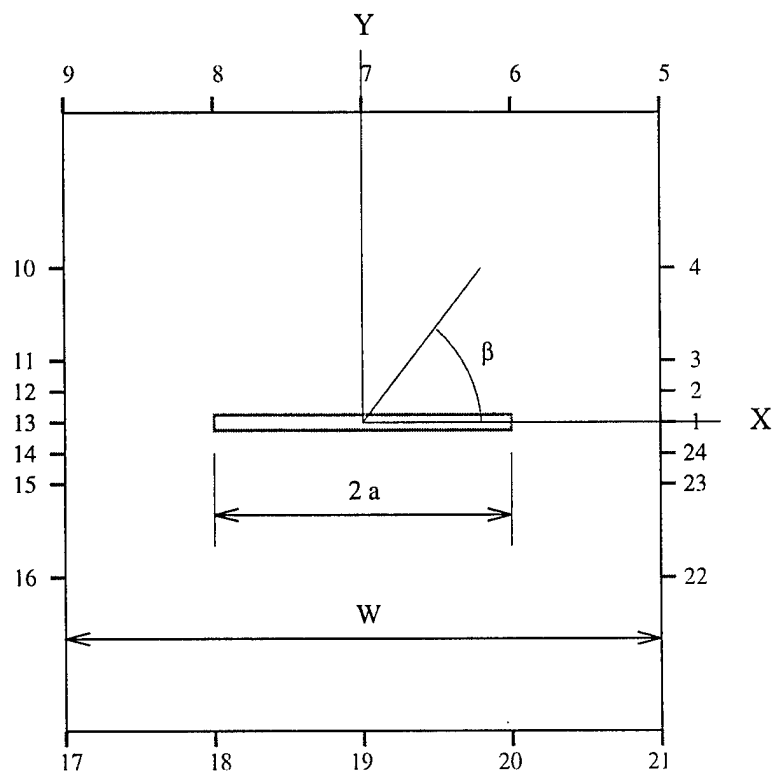


Figure 1: BEM Mesh for Antiplane Shear Validation Problem

The exact displacement field solution for points on the crack surfaces (corresponding to the values of the potential in the field) is given in [9] as

$$\frac{w(x \in \Gamma, 0)}{a} = \frac{\tau_0}{\mu} \sqrt{1 - \left(\frac{x}{a}\right)^2} \quad (54)$$

The singular stress terms near the crack tip are given as follows

$$\begin{aligned} \tau_{xz} &= -\frac{K_{III}}{\sqrt{2\pi r}} \sin \frac{\theta}{2} \\ \tau_{yz} &= +\frac{K_{III}}{\sqrt{2\pi r}} \cos \frac{\theta}{2} \end{aligned} \quad (55)$$

The BEM validation solutions are for a normalized total plate width of  $W/2a = 100$ . The solution for the stress intensity factor is judged to be equivalent to that of the infinite crack. The BEM code reproduces the exact solution for the stress intensity factor, the gradient along the crack, and the displacement of the crack. The accuracy relative to the above analytical solutions for the infinite body is 0.004%, and can be further decreased by increasing  $W/2a$ . The BEM code is therefore taken to be validated.

## 9 Application to the Electromagnetic Problem

The target problem is the prediction of the gradient of the three dimensional magnetic field created by steady current flow through a two dimensional plate containing one or two cracks coming from a hole. The electrical field problem in two dimensions is solved using the Green's function formulation of the previous sections. We then apply three dimensional potential theory to get the induced magnetic field normal to the plate. All three dimensional aspects of the current flow problem in the finite thickness plate are ignored and the two dimensional current flow is integrated over the finite thickness of the plate to get the three dimensional magnetic vector at a specified field location. The normal component of the magnetic field is detected at that location using a fine-scale magnetometer type of device.

The following few equations summarize the application of the special Green's function to the problem of the electromagnetic (EM) field problem of steady current flow through a body with a crack. The surfaces will be assumed to be perfectly insulating except for the surfaces of current injection and removal. The conservation of charge is a side condition for this Neumann problem. The following derivations are based on the equations and definitions in [8].

The vector electrical field for the steady-electrical conduction problem  $\vec{E}(q)$  is taken to be the negative gradient of a harmonic function.

$$\vec{E}(q) = -\vec{\nabla}V(q) \quad (56)$$

The current vector  $\vec{J}(q)$  is scaled from the electrical field by the conductivity  $\sigma$  which is taken to be a constant for the body.

$$\vec{J}(q) = \sigma \vec{E}(q) \quad (57)$$

The steady current flow problem means that the electrostatic potential  $V(q)$  is harmonic,  $\nabla^2 V = 0$ .

The boundary conditions for the conductor are given in terms of the current flow density across the boundary defined by its outward normal  $\hat{n}$  unit vector.

$$\vec{J}(Q) \cdot \hat{n}(Q) = -\sigma \frac{\partial V}{\partial n} = \sigma g(Q) \quad (58)$$

For insulated portions of the boundary,  $g(Q) = 0$ . Thus, we have a Neumann problem to solve with the BIE, for the potential  $V$ . The BIE for this problem is given below.

$$\int_S [V(Q) - V(P)] \frac{\partial \Psi(P, Q; a)}{\partial n(Q)} dS(Q) = \int_S \Psi(P, Q; a) g(Q) dS(Q) \quad (59)$$

The physical interpretation of the requirement for the solvability of this Fredholm equation of the First Kind is that the total current flow is conserved. When we account for the fact that parts of the regular boundary are also insulated, we get the final form of the EM-BIE for our application.

$$\int_S [V(Q) - V(P)] \frac{\partial \Psi(P, Q; a)}{\partial n(Q)} dS(Q) = \int_{S_N} \Psi(P, Q; a) g(Q) dS(Q) \quad (60)$$

The solution of the EM-BIE is by the use of boundary element modeling of the surface and the imposition of boundary data interpolatives for each boundary element. The EM-BIE code is based on the algorithm in [6] except that we now use quadratic variations for all boundary data, straight-line boundary elements, and exact integration of the boundary element terms.

The vector magnetic field  $\vec{B}$  at an arbitrary point in space but caused by the steady current is derived according to the law of Biot-Savart [8]. We will take the three dimensional field point for the determination of the magnetic field as the point  $c(x)$ . The magnetic field is given as the curl of the current field divided by the distance between the coil point and the integration point. The result, written for the *three dimensional problem*, is given as follows.

$$\vec{B}(c) = \frac{\mu_0}{4\pi} \int_R \vec{\nabla}_c \times \left( \frac{\vec{J}(q)}{r(c, q)} \right) dV(q) \quad (61)$$

where  $\mu_0$  is the free space permeability constant. Note that the gradient is taken at the free-space point  $c$  and not the integration point  $q$ . The gradient could be taken outside of the integral and lead to a different potential formulation for the non-steady state solution. We will leave the gradient inside the integration for our developments.

The result can also be written in terms of the electrical current potential  $V(q)$ , which substitution is valid for the steady-state electromagnetic formulation, as given in Eq. 56.

$$\vec{B}(c) = -\frac{\mu_0 \sigma}{4\pi} \int_R \vec{\nabla}_c \times \left( \frac{\vec{\nabla}_q V(q)}{r(c, q)} \right) dV(q) \quad (62)$$

At this time we can expand the gradient operator as follows

$$\vec{\nabla}_c \times \left( \frac{\vec{\nabla}_q V(q)}{r(c, q)} \right) = -\vec{\nabla}_q \times \left( \frac{\vec{\nabla}_q V(q)}{r(c, q)} \right) + \frac{\vec{\nabla}_q \times \vec{\nabla}_q V(q)}{r(c, q)} \quad (63)$$

However, the last term above is zero due to taking the curl of a gradient of a scalar field. We can then write the following form in terms of the derivatives at  $q$ .

$$\vec{\nabla}_c \times \left( \frac{\vec{\nabla}_q V(q)}{r(c, q)} \right) = -\vec{\nabla}_q \times \left( \frac{\vec{\nabla}_q V(q)}{r(c, q)} \right) \quad (64)$$

The derivatives are now all at the point  $q$  and we can drop the notation of the derivative point. We now use Stokes' theorem to convert the volume integral into the equivalent surface integral, as follows. The form of Stoke's theorem for the current application is now given,

$$\int_V \vec{\nabla} \times \vec{F} dV = \oint \hat{n} \times \vec{F} dS \quad (65)$$

where  $\hat{n}$  is the surface normal. The model problem is a plate with contours defined in the  $x$ - $y$  plane and two parallel surfaces in the  $z$ -direction. Thus, if we take the  $z$ -component of the left-hand side of Eq. 65, the resulting surface integrals are on the two-dimensional contours for the plate being analyzed. It is this component of the gravity field that we wish to model. The second identity converts the cross-product term to the following dot-product term.

$$\begin{aligned}\hat{e}_3 \cdot (\hat{n} \times \vec{F}) &= (\hat{e}_3 \times \hat{n}) \cdot \vec{F} \\ &= \hat{t} \cdot \vec{F}\end{aligned}\quad (66)$$

and thus

$$\int_V \hat{e}_3 \cdot (\vec{\nabla} \times \vec{F}) dV = \oint \hat{t} \cdot \vec{F} dS \quad (67)$$

Substituting the results from Eq. 62 and 63 into Eq. 67, we obtain the necessary boundary integrals for the  $B_3$  component of the magnetic field in terms of the current flow along the boundaries of the two-dimensional plate.

$$B_3(c) = B_z(c) = \frac{\mu_0 \sigma}{4\pi} \int_{S+\Gamma} \frac{\vec{\nabla} V(Q) \cdot \hat{t}}{r(c, Q)} dS(Q) \quad (68)$$

The modeling approach that is to be used for the EM-applications is to be quasi-three dimensional. We take the current to be defined for two dimensional slices parallel to the surface of the plate. Each slice has a two dimensional surface and crack geometry, although the crack geometry can be changed for each layer to simulate a three dimensional crack. The quasi-three dimensional approach neglects flow components in the direction normal to the surface of the plate. This approximation may be valid if changes in the geometry in the direction normal to the plane of the plate are small.

The tangent vector in the above magnetic field problem is now unique and is the vector tangent to the two dimensional surface which has been employed in the EM-BIE formulation. The tangential derivatives of the potential  $V$  at the boundary can therefore be determined from the EM-BIE solution, including points on the crack tip. Analytical derivation of the special Green's function to get the tangential derivatives is used to compute the singular current flow at the crack tip. However, the above form is still in three dimensional form and its integration will be discussed in the next section.

$$\vec{\nabla}_p V(p) \cdot \vec{t} = -\frac{1}{2\pi} \int_S [V(Q) - V(P)] \frac{\partial^2 \Psi(p, Q; a)}{\partial n \partial t} dS(Q) + \frac{1}{2\pi} \int_S \frac{\partial V(Q)}{\partial n} \frac{\partial \Psi(p, Q; a)}{\partial t} dS(Q) \quad (69)$$

The magnetic field at  $c(\mathbf{x})$  is derived from a volume potential converted to the surface tangential current flow problem. If the current flow was truly two dimensional, the two dimensional result for the magnetic field would convert the above equation to the  $\log(z - c)$  form used for the fundamental solution. Clearly, the quasi-three dimensional approach contains the most critical three dimensional elements of the magnetic field problem and can probably serve well in the current application, in spite of the current flow approximations used.

## 9.1 The Biot-Savart Integral

The Biot-Savart law [11] is used to calculate the  $z$ -component of the magnetic field from the tangential derivative of the scalar potential,  $V$ . The integral from Eq. 68 is written again in the local coordinate system of the measurement device, as follows

$$B_z(x) = -\frac{\mu_0 \sigma h}{4\pi} \int_{S+\Gamma} \frac{\vec{\nabla} V(Q) \cdot \hat{t}}{r(c, Q)} dS(Q) \quad (70)$$

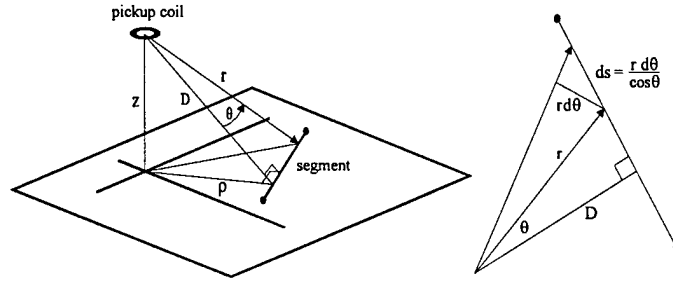


Figure 2: Integration geometry between pickup coil and boundary segment

where  $h$  is the thickness of the plate. The BEM algorithm calculates  $dV/dt$  as a piecewise linear result since we are taking  $V(Q)$  to be represented as piecewise quadratic. Letting  $V_t = \vec{\nabla} V \cdot \hat{t}$  be the tangential component of the gradient of the scalar potential, we have for the line segment along the arc length  $s$ , where the surface is taken to have unit thickness ( $dS = 1 \cdot ds$ ).

$$V_t(Q) = b_1 + b_2 s \quad (71)$$

This integration is done for all boundary elements except for the crack surface  $\Gamma$ . Substituting this  $V_t$  into the integral for  $B_z(c)$  gives the contribution to the magnetic field at point  $c$  due to all boundaries except for the crack surface,  $\Gamma$ .

$$B_z(c)|_S = -\frac{\mu_0 \sigma h}{4\pi} \int_S \frac{b_1 + b_2 s}{r(c, Q)} ds(Q) \quad (72)$$

To carry out the integration, the geometrical relations for  $r$  and  $s$  must be determined.

From Figure 2 we can see that

$$\begin{aligned} r &= \frac{D}{\cos \theta} \\ D &= \sqrt{z^2 + \rho^2} \\ ds &= \frac{r d\theta}{\cos \theta} = \frac{D d\theta}{\cos^2 \theta} \\ s &= D \tan \theta \Big|_{\theta_1}^{\theta_2} = D(\tan \theta - \tan \theta_1) \end{aligned} \quad (73)$$

Therefore, for the boundaries other than the crack, the integral is now

$$\begin{aligned} B_z(c)|_S &= -\frac{\mu_0 \sigma h}{4\pi} \int_S \frac{b_1 + b_2 D(\tan \theta - \tan \theta_1)}{D/\cos \theta} \frac{D d\theta}{\cos^2 \theta} \\ &= -\frac{\mu_0 \sigma h}{4\pi} \left[ B_1 \int_S \frac{d\theta}{\cos \theta} + b_2 D \int_S \frac{\sin \theta}{\cos^2 \theta} \right] \\ &= -\frac{\mu_0 \sigma h}{4\pi} \left[ B_1 \ln \left[ \tan \left( \frac{\pi}{4} + \frac{\theta}{2} \right) \right] + \frac{b_2 D}{\cos \theta} \right]_S \end{aligned} \quad (74)$$

where  $B_1 = b_1 - b_2 D \tan \theta_1$ .

Since the surface  $S$  is divided into  $n$  segments, the summation of this equation – evaluated over each segment for which  $V_t$  is defined by a single linear equation (each defined by a different  $b_1$  and

$b_2$ ) – will determine  $B_z$  at the pickup coil.

$$B_z(c) = \sum_n -\frac{\mu_0 \sigma h}{4\pi} \left[ B_1 \ln \left[ \tan \left( \frac{\pi}{4} + \frac{\theta}{2} \right) \right] + \frac{b_2 D}{\cos \theta} \right]_{\theta_1}^{\theta_2} \quad (75)$$

The angles  $\theta_1$  and  $\theta_2$  correspond to the angles between the perpendicular  $D$  and each endpoint of the segment as the summation moves in a positive sense around the boundary (material on left).

For points on the crack surface, the singular behavior of  $V_t$  at the crack tip requires special consideration. The complete analytic representation of  $V_t$  for crack problems is given by [12]

$$V_t = \frac{f_1(x)}{\sqrt{x^2 - a^2}} + f_2(x) \quad (76)$$

where  $f_1(x)$  and  $f_2(x)$  are analytic functions of the real position  $x$  on the crack and  $a$  is the crack half-length.

The first term in Eq. 76 contains the discontinuity at the crack tip while the second term is needed to match far field (away from the crack) boundary conditions. On the crack surface, Eq. 76 can be rewritten as

$$\begin{aligned} V_t|_{\Gamma} &= \frac{if_1(x)}{\sqrt{a-x}\sqrt{a+x}} + f_2(x) \\ &= \frac{1}{\sqrt{R}} \frac{if_1(x)}{\sqrt{a+x}} + f_2(x) \\ &= \frac{1}{\sqrt{R}} iF_1(x) + f_2(x) \end{aligned} \quad (77)$$

where  $R$  is the distance measured from the crack tip at  $x = a$ . For the region near the positive crack tip, the behavior of  $V_t$  is known to follow

$$V_t = \frac{K^+}{\sqrt{2\pi R}} \sin \frac{\beta}{2} \quad (78)$$

where  $K^+$  is the potential intensity factor (PIF) of the crack on the positive x-axis side. Note that at  $R = 0$  (crack tip),  $V_t = \infty$ .

If there were a crack on the opposite side (negative x-direction) of the rivet, then there would be a corresponding  $V_t$  term proportional to  $K^-$ . The sin function multiplier reflects a geometrical dependence of  $V_t$  on  $\beta$ , the angle measured from the crack tip axis to the evaluation point (see Figure 1). For points on the upper surface of the crack,  $\beta = \pi$  and the multiplier is a (+1). For points on the lower surface of the crack,  $\beta = -\pi$  and the multiplier is a (-1). Therefore, combining Eq. 77 and Eq. 78, the value (real part only) of the term multiplying the singular term,  $F_1(x)$ , can be expressed in terms of the PIF

$$F_1(a) = \pm \frac{K^+}{\sqrt{2\pi}} - f_2(a) \quad (79)$$

Due to the singular behavior of  $V_t$  at the crack tip, numerical integration will be necessary to evaluate the magnetic field contribution of the crack. Values of  $V_t$  will be evaluated for the upper and lower crack surfaces using the BIE program and then the magnetic field will be calculated through a numerical integration of the previously stated Biot-Savart relation (Eq. 70).

## 9.2 Numerical integration of the Biot-Savart integral

Numerical integration over the crack is accomplished using discretization of the crack boundary into elements. By utilizing a coordinate transformation,  $V_t$  can be expressed in terms of nodal values

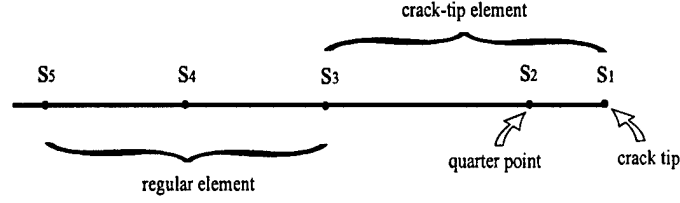


Figure 3: Crack divided into regular and quarter point (crack-tip) elements

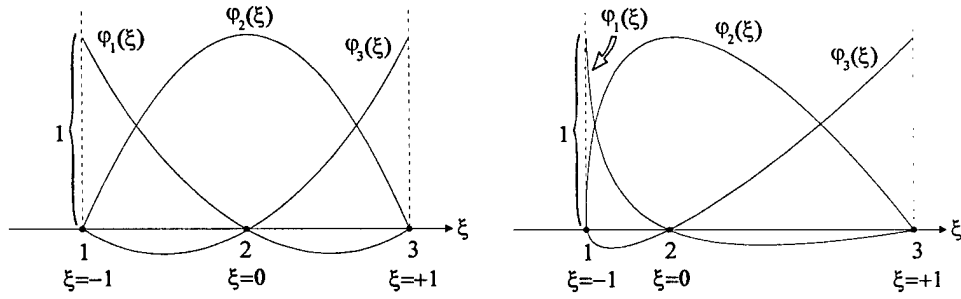


Figure 4: Quadratic interpolation functions for mapping the regular and crack tip elements into the intrinsic  $\xi$ -space

and interpolation functions (or shape functions) [13] of an intrinsic coordinate  $\xi$ . Once mapped into  $\xi$ -space, Gaussian quadrature numerical integration can be used to evaluate the integral. The present formulation will use quadratic interpolation functions  $N_m(\xi)$  which requires three nodes per boundary element.

The crack will be modeled using one crack-tip element containing the crack-tip node and one regular element, each element being defined by three nodes (see Figure 3). The regular element is a straight-forward use of the interpolation functions but the crack-tip element will require some modification to accommodate the singularity at the crack tip. The crack-tip element contains the crack tip node as its first node and the mapping uses the quarter-point formulation [13] to account for the inverse square-root singular behavior at the crack tip. The other regular element will use the general form of the shape functions to map them to  $\xi$ -space.

The general form of the quadratic interpolation functions used to map the function to be integrated into the  $\xi$ -space are as follows;

$$\begin{aligned} N_1(\xi) &= \frac{1}{2}\xi(\xi - 1) \\ N_2(\xi) &= 1 - \xi^2 \\ N_3(\xi) &= \frac{1}{2}\xi(\xi + 1) \end{aligned} \quad (80)$$

The parent element along the  $\xi$ -axis with uniformly spaced nodes at  $\xi = -1, 0, +1$  and the parent shape functions are shown in Figure 4.

The spatial coordinate transformation,  $s = s(\xi)$  maps the parent element ranging from  $\xi = -1$

to  $\xi = +1$  onto each of the crack boundary elements. A set of three parent shape functions are created for each element. It is desirable that this mapping be one-to-one so that each point in the parent element maps onto one point in the real element. In particular, the boundary nodes of the parent element,  $\xi = 1$ , must map onto the boundary nodes of the real element to ensure continuity at the interelement boundaries. For the quadratic element, the mapping takes the form:

$$\begin{aligned} s &= \sum_{k=1}^3 s_k N_k(\xi) \\ &= -\frac{1}{2}\xi(1-\xi)s_1 + (1-\xi^2)s_2 + \frac{1}{2}\xi(1+\xi)s_3 \end{aligned} \quad (81)$$

where  $s_1, s_2$ , and  $s_3$  are the corresponding real-space nodal values of the variable being mapped from the real element to the parent element. It can be seen that this equation maps the parent nodes onto the real nodes:

$$\begin{aligned} \xi &= -1 \rightarrow s = s_1 \\ \xi &= 0 \rightarrow s = s_2 \\ \xi &= +1 \rightarrow s = s_3 \end{aligned} \quad (82)$$

Only the values of  $s_1, s_2$ , and  $s_3$  for each element need to be changed for each mapping. The coordinate transformation into  $\xi$ -space of the integral results in the following sum

$$\int_{\Gamma} F(s) ds \rightarrow \sum_{k=1}^3 \int_{-1}^{+1} N_k(\xi) F_k J(s, \xi) d\xi \quad (83)$$

where  $F_k$  is the value of the function at the  $k^{th}$  node and  $J(s, \xi)$  is the Jacobian of the mapping of the real surface onto the reference surface.

$$J(s, \xi) = \frac{ds}{d\xi} = \sum_{k=1}^3 \frac{dN_k}{d\xi} s_k \quad (84)$$

The Jacobian can be written out explicitly for use with quadratic shape function as follows.

$$J(s, \xi) = \left( \xi - \frac{1}{2} \right) s_1 - 2\xi s_2 + \left( \xi + \frac{1}{2} s_3 \right) \quad (85)$$

For the regular element, the location of the second node is midway between the endpoint nodes of the element,  $s_2 = (s_1 + s_3)/2$ , so the resulting mapping is

$$\begin{aligned} s &= -\frac{1}{2}\xi(1-\xi)s_1 + (1-\xi^2)s_2 + \frac{1}{2}\xi(1+\xi)s_3 \\ &= \frac{(1-\xi)s_1 + (1+\xi)s_3}{2} \end{aligned} \quad (86)$$

with the corresponding Jacobian

$$J = \frac{ds}{d\xi} = \frac{s_3 - s_1}{2} \quad (87)$$

For  $s_1 = 0$  and  $s_3 = L$ , the contribution to  $B_z$  of the regular element on the upper crack surface becomes

$$B_z|_{\Gamma} = -\frac{\mu_0 \sigma h}{4\pi} \int_0^L \left( \frac{V_t(s)}{r(s)} \right) ds \quad (88)$$



$$\begin{aligned}
&= -\frac{\mu_0 \sigma h}{4\pi} \int_{-1}^{+1} \left[ N_1(\xi) \left( \frac{V_t(s)}{r(s)} \right)_{s_1} + N_2(\xi) \left( \frac{V_t(s)}{r(s)} \right)_{s_2} + N_3(\xi) \left( \frac{V_t(s)}{r(s)} \right)_{s_3} \right] J(s, \xi) d\xi \\
&= -\frac{\mu_0 \sigma h}{4\pi} \frac{L}{2} \int_{-1}^{+1} \left[ N_1(\xi) \left( \frac{V_t(0)}{r(0)} \right) + N_2(\xi) \left( \frac{V_t(\frac{L}{2})}{r(\frac{L}{2})} \right) + N_3(\xi) \left( \frac{V_t(L)}{r(L)} \right) \right] d\xi
\end{aligned}$$

This result can now be numerically integrated using regular Gaussian quadrature techniques [13].

For the crack-tip element on the upper crack surface, the standard mapping to  $\xi$ -space needs to be modified to accommodate the  $1/\sqrt{s}$  behavior of  $V_t(s)$  at the crack tip. In what follows, the crack tip point will be mapped at  $s = 0$ . The general approach will be to split the  $V_t(s)$  term into a singular term multiplied times a non-singular coefficient. The form of  $V_t(s)$  follows from Eq. 77.

$$\begin{aligned}
V_t(s)|_{\Gamma} &= \frac{if(s)}{\sqrt{s}\sqrt{2L-s}} \\
&= \frac{1}{\sqrt{s}} F_1(s)
\end{aligned} \tag{89}$$

To map  $V_t(s)$  into  $\xi$ -space, the singular term will use an inverse mapping relation and the non-singular term will use the quadratic shape functions. To determine the inverse mapping relation, we start with the  $1/\sqrt{s}$  behavior which can be represented by placing the midnode of the quadratic element at the quarter point location

$$s_2 = \frac{1}{4}(s_3 - s_1) \tag{90}$$

Therefore, choosing  $s_1 = 0$ ,  $s_2 = \frac{1}{4}L$ ,  $s_3 = L$  in Eq. 86, the quarter point mapping is given by the following result

$$s = (1 - \xi^2) \frac{L}{4} + \frac{1}{2} \xi(1 + \xi)L \tag{91}$$

which has a corresponding inverse mapping given as follows.

$$\xi = -1 + 2\sqrt{\frac{s}{L}} \tag{92}$$

The Jacobian  $J$  is given by

$$\begin{aligned}
J = \frac{ds}{d\xi} &= -2\xi \frac{L}{4} + \frac{1}{2}(1 + 2\xi)L \\
&= \frac{L}{2}(1 + \xi)
\end{aligned} \tag{93}$$

Note that at the  $s = 0$  ( $\xi = -1$ ) point the Jacobian also equals zero. This characteristic is important when evaluating the integral of the mapped function. The  $1/\sqrt{s}$  term is represented in  $\xi$ -space by solving for  $1/\sqrt{s}$  in terms of  $\xi$  in Eq. 92

$$\frac{1}{\sqrt{s}} = \frac{2}{\sqrt{L}(\xi + 1)} \tag{94}$$

Therefore, the  $B_z$  contribution due to the crack-tip element on the upper crack surface is as follows

$$\begin{aligned}
B_z|_{\Gamma} &= -\frac{\mu_0 \sigma h}{4\pi} \int \frac{V_t(s)}{r(s)} ds \\
&= -\frac{\mu_0 \sigma h}{4\pi} \int_0^L \frac{1}{\sqrt{s}} \left( \frac{F(s)}{r(s)} \right) ds
\end{aligned} \tag{95}$$

$$\begin{aligned}
&= -\frac{\mu_0 \sigma h}{4\pi} \int_{-1}^{+1} \frac{2}{\sqrt{L}(\xi + 1)} \left[ N_1(\xi) \left( \frac{F(s)}{r(s)} \right)_{s_1} + N_2(\xi) \left( \frac{f(s)}{r(s)} \right)_{s_2} + \right. \\
&\quad \left. N_3(\xi) \left( \frac{F(s)}{r(s)} \right)_{s_3} \right] \frac{L}{2} (\xi + 1) d\xi \\
&= -\frac{\mu_0 \sigma h}{4\pi} \sqrt{L} \int_{-1}^{+1} \left[ N_1(\xi) \left( \frac{F(s_1)}{r(s_1)} \right) + N_2(\xi) \left( \frac{F(s_2)}{r(s_2)} \right) + N_3(\xi) \left( \frac{F(s_3)}{r(s_3)} \right) \right] d\xi
\end{aligned}$$

Note that as  $\xi \rightarrow -1$  the singular term ( $\xi + 1$  in denominator) goes to infinity but is canceled by the Jacobian term ( $\xi + 1$  in numerator) going to zero, thereby making the overall function well behaved in the mapped space. All values of  $F, r$ , and  $s$  are known except for  $F$  at the crack tip node which has the singularity. But at the crack tip, the value of the function is the PIF( $K^+$ )

$$F(s_1) = \frac{K^+}{\sqrt{2\pi}} \quad (96)$$

All boundaries are now taken care of and the following section summarizes the experimental validation of the measurement model based on this development.

### 9.3 Experimental Validation

A measurement model has been developed using this BIE/EM formulation. The program simulates the scanning of a Superconducting Quantum Interference Device (SQUID) magnetometer [14] over a sample containing a crack. The SQUID magnetometer uses small pickup coils to sense magnetic field above the sample. Injecting a uniform DC-current in the sample causes the current to be parallel to the sample's surface under the pickup coil. The associated magnetic field is mostly tangential to the plate surface for scans located centrally and with small lift-off distances. A flaw in the specimen will perturb the current distribution and produce a vertical magnetic field component that can then be detected by the SQUID. When the SQUID is scanned two-dimensionally over the sample, a magnetic field map is produced, revealing a flaw signature that commonly has a dipolar shape (maximum and minimum peaks).

As a measurement reference, electrodischarge machined (EDM) slots and saw cuts are used in calibrating NDE systems for detection of cracks. A combination of a drilled hole with an EDM slot is an approximation to a crack emanating from an aircraft fastener hole. Fabrication of test samples made this way is simple and controllable making it easy to build a test set representing the range of conditions that are of interest. But measurements with NDE instruments [15] have shown that the instrument response is not necessarily the same as that from a fatigue crack of the same size and geometry. It is possible that crack closure may cause electrical conductivity across parts of the fatigue crack thus causing a reduced signal response over an electrically insulated slot. The BIE formulation used in the SQUID measurement model is for a closed crack (no width) but electrically insulated along the entire length. These issues must be taken into consideration when validating the model against experimental measurements on open cracks (i.e., slots) and actual fatigue cracks which may have closure. For this work, magnetic field map shape comparisons are the basis for validation and provides most of the information, except amplitude, needed to accomplish this.

Following are descriptions of two experimental measurements on fabricated samples representative of those commonly used in SQUID NDE.

**Case I:** The first validation experiment used a 5 mA DC-current injected into a 75 mm  $\times$  150 mm  $\times$  0.03 mm copper clad circuit board containing a 15 mm  $\times$  0.03 mm slot cut with a scalpel (see Figure 5). Although this setup does not provide completely uniform current injection across the sample (transverse to the slot) due to the point source electrodes, the region around the centrally located slot should be relatively uniform.

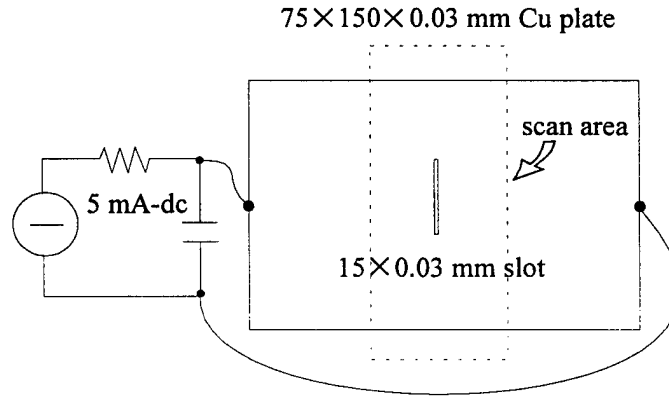


Figure 5: Case I: Experimental setup for DC-current injection in copper plate with slot

Figure 6 shows the contour map resulting from a 2-D scan over the sample with the lines AA', BB', and CC'. Profiles along these lines on this map are compared to those calculated by the measurement model. The scaling factor between the measured signal response (a voltage) and the calculated magnetic flux was determined using these profiles. Magnetic field shape characteristics (matching of peaks and valleys) will reflect the accuracy of the measurement model since a difference between the model and experiment would show up as a mismatch of the profiles at either the edge or the crack locations.

The measurement model is in very good agreement with experiment for all profiles. A slight mismatch at the right side of AA' can be seen and is most likely due to a small variation in liftoff during a scan (i.e. sample not level).

**Case II:** The second validation measurement was similar to the first with a 5 mA DC-current injected into a 100 mm  $\times$  150 mm  $\times$  0.03 mm copper clad circuit board containing a 9 mm diameter hole with a 9 mm  $\times$  0.03 mm slot on one side of the hole (see Figure 7). However, the SQUID used for this measurement was a high-T<sub>c</sub> system [16] which used a planar gradiometer (pickup and balance coils in same plane) instead of axially along  $z$ . The scans were taken in an unshielded environment.

Figure 8 shows the contour map resulting from a 2-D scan over the sample. The quadrupolar shape results from the planar gradiometer acting as a spatial differentiator and, by taking the derivative of the dipole-shaped magnetic signal, results in a quadrupolar shape. Since the planar gradiometer was oriented parallel to the plate edges, the edge signal is approximately zero and therefore, only that part of the scan above the hole/slot was used in these comparisons. Profiles along lines on this map are compared to those calculated by the measurement model.

Figure 8 shows the profile comparisons, after scaling, corresponding to the lines AA', BB', and CC' on the contour map. The measurement model is in very good agreement with experiment for all profiles. Again, a difference between the model and experiment would show up as a mismatch of the profiles at the location of the hole/crack.

## 10 Summary and Conclusions

The problem formulation begins with a boundary-integral representation for Laplace's equation in the plane. The presence of a single, straight crack in the plane is represented by a special Green's

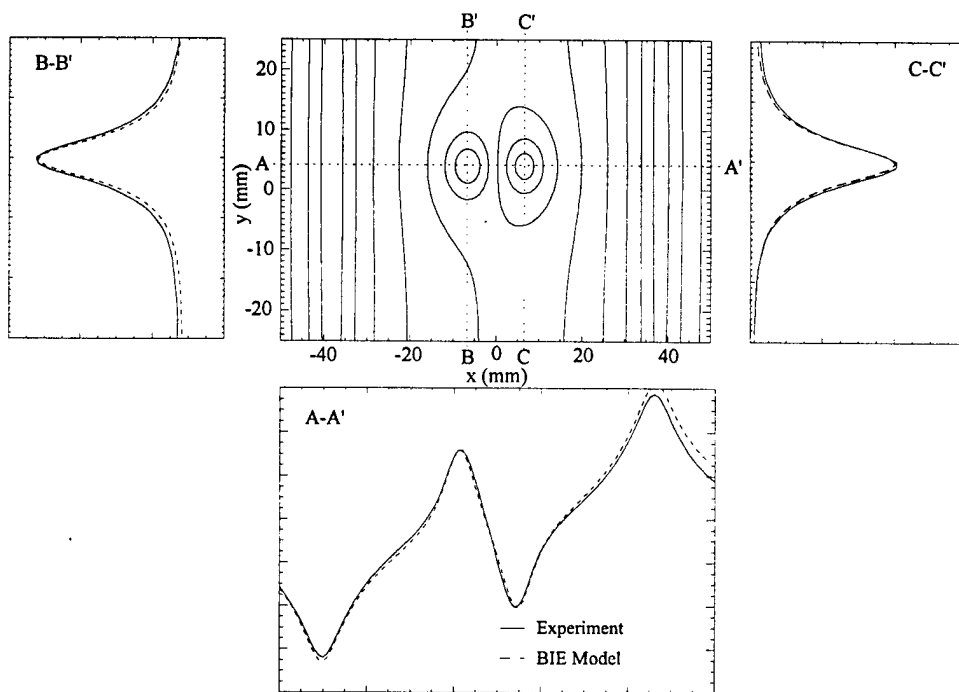


Figure 6: Case I: Magnetic field contour map and profiles comparing experiment with the BEM model

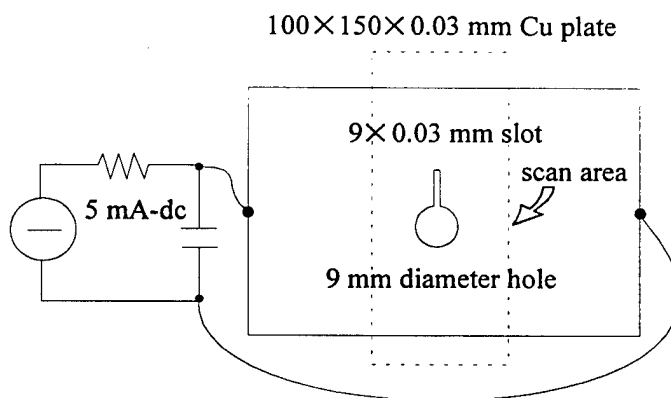


Figure 7: Case II: Experimental setup for DC-current injection in copper plate with hole/slot

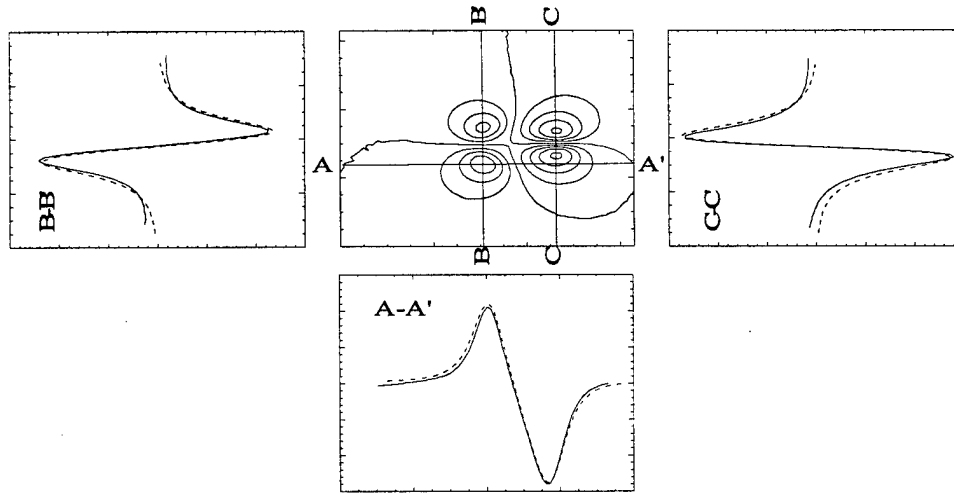


Figure 8: Case II: Magnetic field contour map and profiles comparing experiment with the BEM model

function corresponding to zero flux across the crack. The Green's function used provides a very effective BIE model for the zero-flux boundary condition as the crack then is a part of the integral equation kernels and is not a part of the modeled boundary. A boundary element implementation for the harmonic BIE uses quadratic data variation on piecewise linear boundary elements. The BEM model with the Green's function is validated for the antiplane shear crack problem for which exact solutions exist.

The steady-state electromagnetic problem suitable for calculating the magnetic field for a cracked plate with current injection has been formulated in terms of the derived BIE. The gradient of the potential yields the electrical field vector. The electromagnetic field equations yield the magnetic field at arbitrary three-dimensional space points, using the law of Biot-Savart. The law of Biot-Savart result is given in terms of two boundary integrals of current flow tangent to the boundaries which must be evaluated for all boundary points, including the crack. The cracked plate is represented as a finite thickness plate with a two-dimensional field so that the BEM results can be used in the three-dimensional magnetic field computation.

The magnetic field integrals on the boundary points are formulated as Gaussian quadratures for the quadratic BEM data. The crack surface requires a special integration algorithm due to the singular conditions at each crack tip. Isoparametric boundary element algorithms are used for the magnetic field boundary integrals. The crack tip element uses the quarter-point mapping developed for BEM traction models of fracture problems which contain the leading term in the singular behavior. The mapping is shown to contain the leading term exactly.

The application problem is the magnetic field for the steady-state current flow through two-dimensional plate with a crack. The magnetic field is the normal component of the field, which is the component detected by an experimental SQUID magnetometer. Experimental data was obtained for two cracked plates. The first is a copper plate with an EDM slot representing a crack. The second is a copper plate with a circular hole and a single edge crack normal to the hole surface.

The new BEM results for the magnetic field are used to simulate a SQUID scan over the plate, along three scan lines parallel and normal to the current flow field. The agreement between the BEM results and the experimental data is excellent.

**Acknowledgment** The authors gratefully acknowledge the support of the Air Force Office of Scientific Research, University Research Initiative, AFOSR Grant F49620-93-0268, under the direction of Dr. A. Weinstock. One of us, A. P. Ewing, gratefully acknowledges financial support of the Air Force AASSERT grant F49620-94-1-0369.

## References

- [1] T. A. Cruse, *Boundary Element Analysis in Computational Fracture Mechanics*, Kluwer Academic Publishers, Dordrecht, The Netherlands, 1988.
- [2] M. D. Snyder and T. A. Cruse, Crack tip stress intensity factors in finite anisotropic plates, AFML-TR-73-209, August 1973.
- [3] M. D. Snyder and T. A. Cruse, Boundary-integral equation analysis of cracked anisotropic plates, *International Journal of Fracture*, 11, 2, 315—328 (1975).
- [4] N. I. Muskhelishvili, *Singular Integral Equations*, P. Noordhoff, Holland (1953).
- [5] A. H. England, *Complex Variable Methods in Elasticity*, Wiley—Interscience, London (1971).
- [6] T. A. Cruse, Two-dimensional BIE fracture mechanics analysis, *Applied Mathematical Modeling*, 2, 287—293 (1978).
- [7] T. A. Cruse, Fracture Mechanics, Chapter 7 in *Boundary Element Methods in Mechanics*, ed. D. E. Beskos, North-Holland, Amsterdam, 333—365 (1987).
- [8] P. Lorrain, D. P. Corson, and F. Lorrain, *Electromagnetic Fields and Waves*, W. H. Freeman and Company, New York (1988).
- [9] I. N. Sneddon and M. Lowengrub, *Crack Problems in the Classical Theory of Elasticity*, pp. 37 — 39, John Wiley & Sons, Inc., New York 1969.
- [10] H. Tada, P. Paris, and G. Irwin, *The Stress Analysis of Cracks Handbook*, Section 5.2, Paris Productions Inc., St. Louis, 1985.
- [11] D. J. Griffiths, *Introduction to Electrodynamics*, Prentice-Hall, Inc., New York, p. 185, 1985.
- [12] H. M. Westergaard, "Bearing pressures and cracks," *Journal of Applied Mechanics*, 61, pp. A49-A53, 1939.
- [13] D. S. Burnett, *Finite Element Analysis - From Concepts to Applications*, Addison-Wesley Publishing Co., New York, pp. 305-327, 1987.
- [14] W. G. Jenks, S. S. H. Sadeghi, and J. P. Wikswo, Jr., "SQUIDS for Nondestructive Evaluation," *Journal of Physics D: Applied Physics*, 30, pp. 293-323, 1997.
- [15] W. D. Rummel, J. C. Moulder, and N. Nakagawa, "The Comparative Responses of Cracks and Slots in Eddy Current Measurements," in *Review of Progress in Quantitative NDE*, 10, D. O. Thompson and D. E. Chimenti, Eds., Plenum, New York, pp. 277-283, 1991.
- [16] I. M. Thomas and J. P. Wikswo, Jr., "On the Calibration of the Flux-Voltage Characteristic of SQUID Magnetometers," Department of Physics and Astronomy, Vanderbilt University, Nashville, TN. Manuscript in preparation.
- [17] H.-J. Krause, Y. Zhang, R. Hohmann, M. Grünekee, M. I. Faley, D. Lomparski, M. Maus, H. Bousack, and A. I. Braginski, "Eddy current aircraft testing with mobile HATS-SQUID gradiometer system," presented at EUCAS '97, 1997.

APPENDIX B:  
C-PROGRAM

```

/* PROGRAM: biescan.c */
/* Tony Ewing, Nov 96 */

/* Program to solve the magnetic forward problem using BIE, */
/* generating the simulated magnetic field data due to circular rivet
hole */
/* with crack which would be detected by a single-coil magnetometer. */

#include <stdlib.h>
#include <stdio.h>
#include <math.h>

#define pi 3.141592653589793
#define Nh 200
#define Nc 200

main()

{

/* scan */
char scan_in[20],hole_in[20],crack_in[20];

int i,j,k,l,widsteps,lngsteps,njmp,cnum;

double scnwid,trcewid,scnlng,scninc,xstart,ystart,offset,xinc,theta;
double coilrad,coilrd2,area,loff,product,baseline,base;
double lnginc,widinc,X,Y,Z,calarea,Rcen;
double mu,cnst,rtd,Bmax,Bmin,Bpp;

double intflx[200][200];

/* hole */
int nc,nr,sn,eseg,hseg;

double dm1,dm4,kay,kayprm,dell,del2,snphil,csphil,phil,b1,b1p,b2;
double dm21,dm22,sy,sx,snphi2,csphi2,phi2,s,scal,dm31,dm32,Bh,totflxh1;
double Bhtot,shatny,shatny,rho1,rho1x,rho1y,rldtsnx,rldtsny,D1,rldtsn;
double rho2,rho2x,rho2y,r2dtsnx,r2dtsny,philp,phi2p,beta1,beta2;
double
shattx,shatty,rldtstx,rldtsty,rldtst,r2dtstx,r2dtsty,r2dtst,sign1,sign2
;
double a,b,c,d,e,f1,targ1,targ2,xprint,yprint,xbegin,ybegin,phi,snphi;
double r1,r2,Dlprm,h,sig,calib,totflxh2;

double seg[Nh+1][3];
double Vth[Nh+1][3];
double flxh[200][200];
double flxt[200][200];

/* crack */
int gs,snj,sgint,cseg,cnod;

double n1,n2,n3,rxil,rxil2,rxil3,Vtxi,j1,j2,j3,rhon1,rhon2,rhon3,jxi,AC;
double snd1,snd2,snd3,rhon1x,rhon1y,rhon2x,rhon2y,rhon3x,rhon3y;

double Vtxi1,Vtxi2,Vtxi3,jxi1,jxi2,jxi3,Lx,Ly,L,VtR1,VtR2,VtR3;

```



```

double Bc,Bctot,totflxc1,totflxc2,holrad,biesign;

double node[Nc+1][3];
double Vtc[Nc+1];
double flxc[200][200];
double I5[6],xi5[6],w5[6];

/* print */
int ip,jp,print;

/* math functions */
double cos(double),sin(double),acos(double),tan(double);
double fabs(double),pow(double,double),sqrt(double);
double log(double);

FILE *fpin;
FILE *fpin1;
FILE *fpin2;
FILE *fpout;
FILE *fpout1;
FILE *fpout2;

/* open scanning input file */

printf("Input scan input file name: ");
scanf("%s",scan_in);

if((fpin=fopen(scan_in,"r"))==NULL)
{
    printf("cannot open file\n");
    exit(1);
}

/* open BIE segments input file for hole */

fscanf(fpin,"%s",hole_in);

if((fpin1=fopen(hole_in,"r"))==NULL)
{
    printf("cannot open file\n");
    exit(1);
}

/* open BIE segments input file for crack */

fscanf(fpin,"%s",crack_in);

if((fpin2=fopen(crack_in,"r"))==NULL)
{
    printf("cannot open file\n");
    exit(1);
}

/* open output file */

if((fpout=fopen("scan.out","a"))==NULL)
{

```

```

    printf("\nCannot open file\n\n");
    exit(1);
}

if((fpout1=fopen("scan1.out","w"))==NULL)
{
    printf("\nCannot open file\n\n");
    exit(1);
}

if((fpout2=fopen("scan2.out","w"))==NULL)
{
    printf("\nCannot open file\n\n");
    exit(1);
}

/* read in boundary info, SQUID parameters and x-y scan geometry */

fscanf(fpin,"%lf",&holrad);
fscanf(fpin,"%lf",&AC);
fscanf(fpin,"%lf",&sig);
fscanf(fpin,"%lf",&h);
fscanf(fpin,"%lf",&calib);
fscanf(fpin,"%d",&eseg);
fscanf(fpin,"%d",&hseg);
fscanf(fpin,"%d",&njmp);
fscanf(fpin,"%d",&cnod);
fscanf(fpin,"%d",&cseg);
fscanf(fpin,"%d",&sgint);
fscanf(fpin,"%lf",&coilrad);
fscanf(fpin,"%lf",&loff);
fscanf(fpin,"%lf",&baseline);
fscanf(fpin,"%lf",&scnwid);
fscanf(fpin,"%lf",&scnlng);
fscanf(fpin,"%lf",&lnginc);
fscanf(fpin,"%lf",&widinc);
fscanf(fpin,"%lf",&offset);

/* read in x,y-coordinates of boundary segment endpoints for hole */
/* njmp is the number of boundary jumps - e.g. 2 closed boundaries is
*/
/* njmp=1 */
for(nr=1;nr<=(eseg+hseg+njmp+1);nr++)
{
    for(nc=1;nc<=2;nc++)
    {
        fscanf(fpin1,"%lf",&seg[nr][nc]);
        /* seg[nr][nc]=(seg[nr][nc])/100.;*/
    }
    for(nc=1;nc<=2;nc++)
    {
        fscanf(fpin1,"%lf",&Vth[nr][nc]);
        printf("Vth[%d][%d]= %f\n",nr,nc,Vth[nr][nc]);
    }
}

/* read in x,y-coordinates of nodes for crack (3 per crack element) */
/* nseg is the total number of segments (2 nodes per segment) */

```

```

/* sgint is the number of segments per element - eg 3 nodes/2
segments/ */
/* 1 element. */
printf("cnod= %d\n",cnod);
for(nr=1;nr<=cnod;nr++)
{
    for(nc=1;nc<=2;nc++)
    {
        fscanf(fpin2,"%lf",&node[nr][nc]);
    }
    fscanf(fpin2,"%lf",&Vtc[nr]);
    printf("Vtc[%d]= %f\n",nr,Vtc[nr]);
}

/* Define constants */

mu=pi*4.0e-07;
rtd=180./pi;
cnst=mu/(4.0*pi);
coilrd2=coilrad*coilrad;
calarea=pi*coilrd2;
widsteps=scnwid/widinc; /* number of scan traces - y direction */
lngsteps=scnlng/lnginc; /* number of steps along x-scan */

/* write statements for ASCII output */
/*fprintf(fpout, "%i\n",lngsteps);
fprintf(fpout, "%i\n",widsteps);*/
fprintf(fpout1, "%i\n",lngsteps);
fprintf(fpout1, "%i\n",widsteps);
fprintf(fpout2, "%i\n",lngsteps);
fprintf(fpout2, "%i\n",widsteps);

/***** START SCAN *****/

for(i=0;i<=widsteps;i++) /* loop to step along y */
{
    printf("loop %d of %d\n",i,widsteps);
    xstart=-scnlng/2.;
    ystart=-offset-(scnwid/2.)+i*(widinc);
    for(j=0;j<=lngsteps;j++) /* loop to step along x */
    {
        xinc=xstart+j*lnginc;
        totflxh1=0.0;
        totflxc1=0.0;
        totflxh2=0.0;
        totflxc2=0.0;
        base=baseline;
        for(cnum=1;cnum<=2;cnum++) /* loop for gradiometer */
        {
            if(cnum==2) base=0.0;
            for(k=0;k<=6;k++) /* loop for coil integration - Roth */
            {
                theta=(pi/3.)*k;
                if(k==0)
                {
                    Rcen=0.0;
                    area=0.25*calarea;

```

```

    }
else
{
    Rcen=0.81650*coilrad;
    area=0.125*calarea;
}
X=Rcen*cos(theta)+xinc;
Y=Rcen*sin(theta)+ystart;

/***** HOLE BEGIN *****/
/* Calculate vectors between source and field points */
Bhtot=0.0;
for(sn=1;sn<(eseg+hseg+njmp+1);sn++)
{
    if(sn==eseg+1) sn++;
    sy=seg[sn+1][2]-seg[sn][2];
    sx=seg[sn+1][1]-seg[sn][1];
    s=sqrt(pow(sx,2)+pow(sy,2));
    shatnx=sy/s;
    shatny=-sx/s;
    shattx=sx/s;
    shatty=sy/s;

/* If modeling rivot hole with crack, since node position from BIE is
in */
/* crack coordinates, need to shift back to global coordinates by */
/* AC (crack length) - only on X now - subtract holrad from rho1x and
rho2x*/

    if(cnod==0) rho1x=X-seg[sn][1];
    else rho1x=X-seg[sn][1]-holrad; /*1st error: subtract hole
radius */
    rholy=Y-seg[sn][2];
    rho1=sqrt(pow(rho1x,2)+pow(rholy,2));
    r1=sqrt(pow(rho1,2)+pow((loff+base),2));
    rldtsnx=rho1x*shatnx;
    rldtsny=rholy*shatny;
    rldtstx=rho1x*shattx;
    rldtsty=rholy*shatty;
    rldtst=rldtstx+rldtsty;
    rldtsn=rldtsnx+rldtsny;

/* Determine sign on angle using dot product with s-tangent */
    if(rldtst==0.0) sign1=-1.0;
    else sign1=-(rldtst/fabs(rldtst));

    D1=fabs(rldtsn);
    D1prm=sqrt(pow(D1,2)+pow((loff+base),2));
    if(cnod==0) rho2x=X-seg[sn+1][1];
    else rho2x=X-seg[sn+1][1]-holrad; /* part 2 of 1st error */
    rho2y=Y-seg[sn+1][2];
    rho2=sqrt(pow(rho2x,2)+pow(rho2y,2));
    r2=sqrt(pow(rho2,2)+pow((loff+base),2));
    r2dtsnx=rho2x*shatnx;
    r2dtsny=rho2y*shatny;
    r2dtstx=rho2x*shattx;
    r2dtsty=rho2y*shatty;

```

```

r2dtst=r2dtstx+r2dtsty;

if(r2dtst==0.0) sign2=-1.0;
else sign2=-(r2dtst/fabs(r2dtst));

phil=sign1*acos(Dlprm/r1);
phi2=sign2*acos(Dlprm/r2);

/* Determine linear constants from tangential derivatives */

b2=((Vth[sn][2])-(Vth[sn][1]))/s;
b1=(Vth[sn][1])-b2*Dlprm*tan(phil);
targ1=tan((pi/4.)+(phil/2.));
targ2=tan((pi/4.)+(phi2/2.));
Bh=(b1*log(targ2/targ1))+(b2*(r2-r1));

Bhtot=Bh+Bhtot;

} /* end loop for hole bie segments */

if(cnum==1)
{
totflxh1=Bhtot*area+totflxh1;
}
else
{
totflxh2=Bhtot*area+totflxh2;
}

/***** HOLE END -CRACK BEGIN *****/

/* Set up Gauss points and corresponding weights arrays for
integration */
xi5[0]=-sqrt((35.+2.*sqrt(70.))/63.);
xi5[1]=-sqrt((35.-2.*sqrt(70.))/63.);
xi5[2]=0.0;
xi5[3]=-xi5[1];
xi5[4]=-xi5[0];
w5[0]=5103./(50.*(322.+13.*sqrt(70.)));
w5[1]=5103./(50.*(322.-13.*sqrt(70.)));
w5[2]=128./225.;
w5[3]=w5[1];
w5[4]=w5[0];

/* Calculate vectors between source and field points */
Bctot=0.0;
snj=0;
for(sn=0;sn<(cseg/2);sn++) /* 2nd error: divide by 2 */
{
if(sn%sgint==0) snj=snj+1;
if(sn==0) snj=0;

/* 5-pt gaussian quadrature integration loop */
for(gs=0;gs<=4;gs++)

```

```

    {
        n1=.5*xi5[gs]*(xi5[gs]-1.);
        n2=(1.-xi5[gs])*(1.+xi5[gs]);
        n3=.5*xi5[gs]*(xi5[gs]+1.);

/* Evaluate terms in integral */

        rhon1x=X-(holrad+node[2*sn+1+snj][1]);
        rhon2x=X-(holrad+node[2*sn+2+snj][1]);
        rhon3x=X-(holrad+node[2*sn+3+snj][1]);
        rhon1y=Y-node[2*sn+1+snj][2];
        rhon2y=Y-node[2*sn+2+snj][2];
        rhon3y=Y-node[2*sn+3+snj][2];
        rhon1=sqrt(pow(rhon1x,2.)+pow(rhon1y,2.));
        rhon2=sqrt(pow(rhon2x,2.)+pow(rhon2y,2.));
        rhon3=sqrt(pow(rhon3x,2.)+pow(rhon3y,2.));

        rxil=(1./(sqrt(pow((loff+base),2.)+pow(rhon1,2.))));
        rxi2=(1./(sqrt(pow((loff+base),2.)+pow(rhon2,2.))));
        rxi3=(1./(sqrt(pow((loff+base),2.)+pow(rhon3,2.))));

        Vtxi1=n1*Vtc[2*sn+1+snj];
        Vtxi2=n2*Vtc[2*sn+2+snj];
        Vtxi3=n3*Vtc[2*sn+3+snj];

/* Determine sign change due to numerical integration direction */
/* starting at crack tip nodes rather than bie integration being */
/* positive direction with material always on left */
        Lx=node[2*sn+3+snj][1]-node[2*sn+1+snj][1];
        Ly=node[2*sn+3+snj][2]-node[2*sn+1+snj][2];
        L=sqrt(pow(Lx,2)+pow(Ly,2));

        if(node[2*sn+1+snj][2]>0.0) biesign=1.0;
        else biesign=-1.0;

/* Check to see if on a crack-tip element or regular element */
        if(sn%sgint==0)
        {
            VtR2=sqrt(AC-fabs(node[2*sn+2+snj][1]));
            VtR3=sqrt(AC-fabs(node[2*sn+3+snj][1]));
            jxi=biesign*sqrt(L);
            I5[gs]=(Vtxi1*rxil+Vtxi2*rxi2+Vtxi3*rxi3)*jxi;
        }
        else
        {
            I5[gs]=(Vtxi1*rxil+Vtxi2*rxi2+Vtxi3*rxi3)*biesign*(L/2.);
        }

    } /* end gaussian quadrature loop */

    Bc=w5[0]*I5[0]+w5[1]*I5[1]+w5[2]*I5[2]+w5[3]*I5[3]+w5[4]*I5[4];
/*
    if(ystart==0) printf("Crack loop [%d], Bc= %e\n",sn,Bc);*/
    Bctot=Bc+Bctot;

} /* end loop for crack bie segments */

```

```

        if(cnum==1)
        {
            totflxc1=Bctot*area+totflxc1;
        }
        else
        {
            totflxc2=Bctot*area+totflxc2;
        }

    } /* end loop for coil integration */
} /* end loop for gradiometer */

flxh[i][j]=cnst*h*sig*calib*(totflxh2-totflxh1);
flxc[i][j]=cnst*h*sig*calib*(totflxc2-totflxc1);
flxt[i][j]=flxh[i][j]+flxc[i][j];

} /* end loop for scan along x */

} /* end loop for increment along y */

/***** END SCAN *****/
/* Set initial values within output range */
Bmax=flxt[1][1];
Bmin=flxt[1][1];

/* Loop to print output file */
for(ip=0;ip<=(widsteps);ip++)
{
    xbegin=-scnlng/2.;
    yprint=-offset-(scnwid/2.)+ip*(widinc);
    for(jp=0;jp<=lngsteps;jp++)
    {
        /* Find max/min of scan */
        if(flxt[ip][jp]>Bmax) Bmax=flxt[ip][jp];
        if(flxt[ip][jp]<Bmin) Bmin=flxt[ip][jp];

        xprint=xbegin+jp*lnginc;
        /*      fprintf(fpout, "%f %f %e\n", xprint,yprint,flxh[ip][jp]);*/
        /*      fprintf(fpout1, "%f %f %e\n",
xprint,yprint,intflx[ip][jp]);*/
        fprintf(fpout2, "%f %f %e\n", xprint,yprint,flxt[ip][jp]);
        /*      fprintf(fpout2, "%e\n",flxt[ip][jp]);*/
    }
}
Bpp=Bmax-Bmin;
fprintf(fpout, "%e\n", Bpp);

fclose(fpin);
fclose(fpin1);
fclose(fpin2);
fclose(fpout);
fclose(fpout1);
fclose(fpout2);

```

```
} /* end of main() */
```



APPENDIX C:  
FLUX/VOLTAGE CALIBRATION OF SQUID MAGNETOMETERS

## Flux/Voltage Calibration of SQUID Magnetometers

The SQUID magnetometer outputs a voltage,  $V$ , proportional to the magnetic flux,  $\Phi$ , through the pickup coil. Many SQUID systems use gradiometers consisting of a pickup coil connected serially to a counter-wound balance coil (Figure C.1). This is done to reject noise from distant field sources (uniform) since the flux through each coil would be approximately the same resulting in zero net flux. For closer sources, such as scanning a sample, the flux is stronger in the pickup coil than in the compensation coil resulting in a net flux and hence, an output voltage.

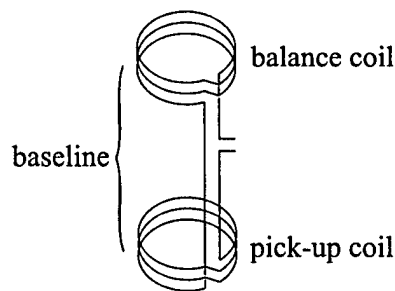


Figure C.1 Gradiometer with pick-up coil and counter-wound balance coil

To use SQUIDs as accurate quantitative measuring tools, correct instrument calibration is necessary to determine the absolute magnetic field being measured. One approach is to scan the SQUID over a standard source for which the magnetic field spatial distribution can be determined analytically so that comparisons can be made. A commonly used source is a current carrying wire (see Figure C.2). From Ampere's Law, it can be determined that the vertical component of magnetic field,  $B_z$ , in the x-direction a distance  $z$  above a current ( $I$ ) carrying wire is given by

$$B_z(x) = \frac{\mu_0 I}{2\pi} \left( \frac{x}{x^2 + z^2} \right). \quad (\text{C.1})$$

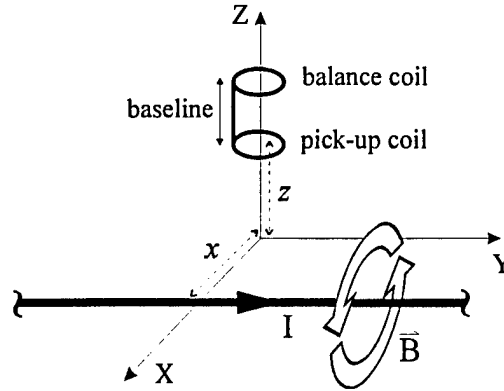


Figure C.2 Calibration using a current carrying wire

Differentiating this relation gives the location of the maximum and minimum peaks of  $B_z$  resulting in relationship for the peak-to-peak separation (see Figure C.3)

$$\frac{dB_z}{dx} = \frac{z^2 - x^2}{(x^2 + z^2)^2} = 0 \Rightarrow x = \pm z$$

$$\therefore \Delta x = 2z.$$
(\text{C.2})

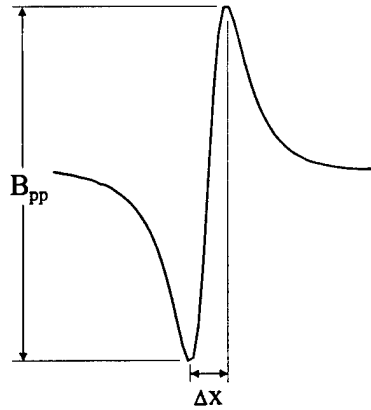


Figure C.3 Dipolar signal showing peak-to-peak separation and amplitude

So, the peak-to-peak field value,  $B_{pp}$ , is determined by the difference of  $B_z$  at  $x = \pm z$

$$\begin{aligned}
B_z(x=z) &= \frac{\mu_0 I}{2\pi} \left( \frac{1}{2z} \right) \\
B_z(x=-z) &= \frac{\mu_0 I}{2\pi} \left( \frac{-1}{2z} \right) \\
\therefore B_{pp} &= [B_z(x=z)] - [B_z(x=-z)] = \frac{\mu_0 I}{2\pi z}.
\end{aligned} \tag{C.3}$$

This can be used to estimate the vertical location ( $z$ ) of the pickup coil above the wire through a measurement of  $B_{pp}$ . This is only an approximation since it assumes a single point detector above an infinite wire. To model the output from a gradiometer above a finite wire, the magnetic field must be integrated over the areas of the pickup and balance coils.

Integration schemes can be found in [21] and used to integrate the magnetic field from a finite length wire, length  $2l$  carrying current  $I$

$$B_z(x, y, z) = \frac{\mu_0 I x}{4\pi(x^2 + z^2)} \left[ \frac{y-l}{\sqrt{(y-l)^2 + (x^2 + z^2)}} + \frac{y+l}{\sqrt{(y+l)^2 + (x^2 + z^2)}} \right]. \tag{C.4}$$

It is usually difficult to know  $z$  accurately since the pickup coils are located inside the dewar. To address the uncertainties in the system variables, a procedure, Calibration Requiring Approximate Parameters [22], has been developed to determine the factor scaling the output voltage to magnetic flux. The procedure uses optimization [23] over liftoff, coil tilt, gradiometer baseline, coil radius, and the calibration factor to “match” the experimentally measured voltage map to the magnetic flux map calculated using Eq. (C.4). The resulting voltage-to-flux calibration factor is independent of magnetic field source and liftoff distance and therefore, can be used for all measurements using that system.

So far in this discussion, the calibration factor has scaled voltage to net magnetic flux ( $\Phi$  – units of weber). It is common practice to state this calibration factor as a voltage to magnetic field ( $B$  – units of tesla) number. This is done by converting the net flux back to an approximate magnetic field value by dividing by the area of the pickup coil. This however introduces error into the resulting value since this conversion must assume a uniform magnetic field across the coil area and ignores the balance coil contribution. This is useful for those interested in approximate magnetic field values that are not dependent on the system's coil geometry, as flux is.

single coil - uniform  $\vec{B}$

$$\Phi = \int_{\text{coil}} \vec{B} \cdot d\vec{A}$$

$$\Rightarrow B = \frac{\Phi}{A}$$

gradiometer - nonuniform  $\vec{B}$

$$\Delta\Phi = \int_{\text{pickup coil}} \vec{B}_1 \cdot d\vec{A}_1 - \int_{\text{balance coil}} \vec{B}_2 \cdot d\vec{A}_2$$

$$\Rightarrow B = ?$$

These issues affect only quantitative amplitude values since the result is an optimized calibration factor used to scale the theoretical result to the experimental measurement. The shape of the magnetic maps is unchanged by this process and does not affect qualitative analysis of the images.

APPENDIX D:  
LIST OF PUBLICATIONS/PRESENTATIONS

"Special Green's Function Formulation of Laplace's Equation for EM Application", T.A. Cruse, **A.P. Ewing**, manuscript in preparation.

"An Optimization-based Procedure for Flux/Voltage Calibration of Axial SQUID Gradiometers", **A.P. Ewing**, C.Hall Barbosa, A.C. Bruno, J.P. Wikswo, Jr., manuscript in preparation.

"Boundary Integral Equation Measurement Model for the ECI Method of NDE", C.Hall Barbosa, **A.P. Ewing**, T.A. Cruse, A.C. Bruno, J.P. Wikswo, Jr., Compumag '97, Nov. 2-6, 1997.

"A SQUID NDE Measurement Model using BEM", **A.P. Ewing**, T.A. Cruse, J.P. Wikswo, Jr., 24<sup>th</sup> Annual Review of Progress in QNDE, 1997 (in print).

"Probability of Detection (POD) in SQUID NDE", **A.P. Ewing**, T.A. Cruse, J.P. Wikswo, Jr., The First Joint DoD/FAA/NASA Conference on Aging Aircraft, July 8-10, 1997.

"Boundary Integral Equations for Modeling Arbitrary Flaw Geometries in ECI NDE", **A.P. Ewing**, C.Hall Barbosa, T.A. Cruse, A.C. Bruno, J.P. Wikswo, Jr. 24<sup>th</sup> Annual Review of Progress in QNDE, 1997 (in print).

"Measurements of Surface-Breaking Flaws in Steel Pipes Using a SQUID Susceptometer in an Unshielded Environment", C.Hall Barbosa, A.C. Bruno, G.S. Kuhner, J.P. Wikswo, Jr., Y.P. Ma, **A.P. Ewing**, 24<sup>th</sup> Annual Review of Progress in QNDE, 1997 (in print).

"Measurements of Surface-Breaking Flaws in Ferromagnetic Plates by Means of an Imaging SQUID Susceptometer", A.C. Bruno, **A.P. Ewing**, J.P. Wikswo, Jr., 1994 Applied Superconductivity Conference.

## REFERENCES

- [1] A. Hoggard, "Fuselage Longitudinal Splice Design.", Structural Integrity of Aging Airplanes, S.N. Atluri, S.G.Sampath, P. Tong (Eds.), Springer-Verlag Press, 1991.
- [2] MIL STD-1530. Design Requirements for Aircraft.
- [3] MIL A-83444, Damage Tolerance Requirements.
- [4] NASA, MSFC STD-1249, NDE Guidelines and Requirements.
- [5] NASA, MSFC HDBK-1453, Fracture Control Requirements.
- [6] D. Broek, "The Civil Damage Tolerance Requirements in Theory and Practice." Structural Integrity of Aging Airplanes, S.N. Atluri, S.G.Sampath, P. Tong (Eds.), Springer-Verlag Press, 1991.
- [7] R.T. Anderson, T.J. Delacy, and R.C. Stewart, "Detection of Fatigue Cracks by Nondestructive Testing Methods", NASA CR-128946, March, 1973.
- [8] W.D. Rummel, P.H. Todd, S.A. Frecska, and R.A. Rathke, "The Detection of Fatigue Cracks by Nondestructive Testing Methods", NASA CR-2369, February, 1974.
- [9] D.S. Buchanan, D.B. Crum, D. Cox, and J.P. Wikswo, Jr., Advances in Biomagnetism, S.J. Williamson, M. Hoke, G. Stroink, and M. Kotani, Eds., (Plenum, New York), pp. 677-679 (1990).
- [10] Y.P. Ma and J.P. Wikswo, Jr., "SQUID Eddy Current Techniques for Detection of Second Layer Flaws", Review of Progress in QNDE, 13, pp. 303-309 (1994).
- [11] Ma, Y.P., and Wikswo, J.P. "Magnetic Field of a Subsurface Spherical Flaw Inside a Current-Carrying Plate", Manuscript in preparation.
- [12] Ma, Y.P., and Wikswo, J.P. "A Solution for the Magnetic Field Produced by a Plate with an Elliptic Inclusion Carrying a DC-Current - Application for Flaw Detection", Manuscript in preparation.
- [13] J.R. Reitz, F.J. Milford, R.W. Christy, Foundations of Electromagnetic Theory, 3<sup>rd</sup> edition, Addison-Wesley Publishing Co. (1979) p. 20.



- [14] Griffiths, D.J., Introduction to Electrodynamics Prentice-Hall, Inc. 1981 pp. 185,48.
- [15] T.A. Cruse and A.P. Ewing, "Special Green's Function Formulation of Laplace's Equation for Electromagnetic Application", manuscript in preparation.
- [16] Westergaard, H.M., "Bearing Pressures and Cracks", *Journal of Applied Mechanics*, Vol. 61, pp. A49-A53. 1939.
- [17] Burnett, D.S., Finite Element Analysis – From Concepts to Applications Addison-Wesley Publishing Company, 1987 pp. 305-327.
- [18] N. Nakagawa, V.G. Kogan, G. Bozzolo, "Effect of Crack Closure on Eddy Current Signals", *Review of Progress in Quantitative NDE*, Vol. 7, D.O. Thompson and D.E. Chimenti, Eds., (Plenum, New York, 1987) pp. 173-179.
- [19] W.D. Rummel, J.C. Moulder, N. Nakagawa, "The Comparative Responses of Cracks and Slots in Eddy Current Measurements", *Review of Progress in Quantitative NDE*, Vol. 10, D.O. Thompson and D.E. Chimenti, Eds., (Plenum, New York, 1991) pp. 277-283.
- [20] W.D. Rummel, "Recommended Practice for a Demonstration of Nondestructive Evaluation (NDE) Reliability on Aircraft Production Parts", *Materials Evaluation*, 40, (August 1982) pp. 922-932.
- [21] B.J. Roth, S. Sato, "Accurate and efficient formulas for averaging the magnetic field over a circular coil", *Biomagnetism: Clinical Aspects*. M.Hoke et al. Editors, Elsevier Publishers B.V., 1992 pp. 797-800.
- [22] A. Ewing, C. Hall, "Calibration of Voltage/Flux Characteristics of SQUID Systems Using Gradiometers", manuscript in preparation.
- [23] MATLAB – Optimization Toolbox, Version 5.0.1.421 1997.
- [24] H-J. Krause, Y. Zhang, R. Hohmann, M. Grünekle, M.I. Faley, D.Lomparski, M. Maus, H. Bousack, and A.I Braginski, "Eddy Current Aircraft Testing with Mobile HTS-SQUID Gradiometer System", presented at EUCAS '97, 1997.
- [25] A.P. Berens and P.W. Hovey, "The Analysis of NDE Reliability Data", Metals Handbook: Nondestructive Evaluation and Quality Control, Vol. 17, 9th ed. 1989.
- [26] J-N. Yang, W.J. Trapp, "Reliability Analysis of Aircraft Structures Under Random Loading and Periodic Inspection", *AIAA Journal*, AIAA, Vol. 12, No. 12, (1974) pp 1623-1630.

- [27] "Relation of Inspection Findings to Fatigue Reliability", Ship Structure Committee, Washington, D.C. U.S. Department of Commerce – National Technical Information Service, (1990).
- [28] R.C.H. Cheng, T.C. Iles, "Confidence Bands for Cumulative Distribution Functions of Continuous Random Variables", Technometrics, Vol. 25, No. 1, (1983), pp. 77-86.
- [29] Y.P. Ma, J.P. Wikswo, Jr., "SQUID Magnetometers for Phase-Sensitive, Depth Selective, Oriented Eddy Current Imaging", 24<sup>th</sup> Annual Review of Progress in Quantitative Nondestructive Evaluation, 1997 (in print).
- [30] Y.P. Ma, J.P. Wikswo, Jr., "Techniques for Depth-Selective, Low-Frequency Eddy Current Analysis for SQUID-Based Nondestructive Testing", J. of Nondestructive Evaluation, Plenum Publishing Corporation, Vol. 14, No. 3, 1995 pp. 149-167.
- [31] A.H-S Ang and W.H. Tang, Probability Concepts in Engineering Planning and Design, Vol. I, John Wiley & Sons, Inc. 1975.
- [32] A.P. Ewing, C.Hall Barbosa, T.A. Cruse, A.C. Bruno, J.P. Wikswo, Jr., "Boundary Integral Equations for Modeling Arbitrary Flaw Geometries in ECI NDE", Jr. 24<sup>th</sup> Annual Review of Progress in Quantitative Nondestructive Evaluation, 1997 (in print).
- [33] C.Hall Barbosa, A.P. Ewing, T.A. Cruse, A.C. Bruno, J.P. Wikswo, Jr., "Boundary Integral Equation Measurement Model for the ECI Method of NDE", Compumag '97, Nov. 2-6, 1997.
- [34] A.P. Ewing, C.Hall Barbosa, T.A. Cruse, A.C. Bruno, J.P. Wikswo, Jr., "Boundary Integral Equations for Modeling Arbitrary Flaw Geometries in ECI NDE", 24<sup>th</sup> Annual Review of Progress in QNDE, 1997 (in print).
- [35] A.P. Ewing, C.Hall Barbosa, A.C. Bruno, J.P. Wikswo, Jr., "An Optimization-based Procedure for Flux/Voltage Calibration of Axial SQUID Gradiometers", manuscript in preparation.
- [36] J.P. Wikswo, Jr., J.D. Achenbach, "Advanced Instrumentation and Measurements for Early Nondestructive Evaluation of Damage and Defects in Aerostructures and Aging Aircraft", Third Annual Report, Air Force University Research Initiative in Materials Degradation and Fatigue in Aerospace Structures, October 4, 1996.

SCIENTIFIC RESEARCH (AFSC)

RESEARCH (AFSC)

RESEARCH (AFSC)

RESEARCH (AFSC)

RESEARCH (AFSC)

RESEARCH (AFSC)

RESEARCH (AFSC)